Two-Dimensional Crystallization of Helical Aromatic Hydrocarbons on Metal Surfaces

---

Dissertation

zur Erlangung der naturwissenschaftlichen Doktorwürde
(Dr. sc. nat.)

vorgelegt der
Mathematisch-naturwissenschaftlichen Fakultät
der
Universität Zürich
von

Johannes Sebastian Seibel

aus Deutschland

Promotionskomitee

Prof. Dr. Karl-Heinz Ernst (Vorsitz)
Prof. Dr. Jay S. Siegel
Prof. Dr. Kim K. Baldridge

Zürich, 2014

Content

Acronyms

[5]H	Pentahelicene
[7]H	Heptahelicene
2D	two-dimensional
AFM	Atomic Force Microscopy
bis[7]H	[9,9']-Bisheptahelicene
BuLi	Butyllithium
db[5]H	[5,6,9,10]-Dibenzopentahelicene
DMF	Dimethylformamide
hv	Visible Light
IET	Inelastic Electron Tunneling
PPh_3	Triphenylphosphine
rac	Racemic
RT	Room Temperature
STM	Scanning Tunneling Microscopy
ToF-SIMS	Time-of-Flight Secondary Ion Mass Spectrometry
UHV	Ultra High Vacuum
XPD	X-ray Photoelectron Diffraction

Summary

Chirality is ubiquitous in nature and all major building blocks of life, for example amino acids, saccharides and nucleotides, are chiral and in general exist only in one enantiomeric form. Thus, intermolecular chiral recognition processes among these biomolecules are of paramount importance to life. Likewise, these recognition processes are responsible for the spontaneous resolution of enantiomers in crystallization of a racemate, so-called conglomerate formation, or diastereomeric salt crystallization, i. e. the enantioselective salt formation of one enantiomer from a racemate with another enantiopure compound. Enantiomer separation via diastereomeric salt crystallization is also an important technique in industry today. However, it is not possible to predict the outcome of crystallization solely based on molecular structure, because it is governed by very small structural influences that are amplified by many cooperating units. This complexity calls for studying appropriate model systems, for example two-dimensional molecular crystals on metal substrates, where submolecular resolution can be achieved by scanning tunneling microscopy. The high-resolution imaging and relatively simple spatial alignment of molecules in 2D compared to 3D allows the investigation of specific molecular interactions. Thereby, helical aromatic hydrocarbons, so-called helicenes, as chiral molecules without a tetragonal carbon atom or functional groups, respectively, allow in particular the investigation of interactions based purely on van-der-Waals forces. Furthermore, the nature of the surface influences heterogeneous nucleation and crystal growth and the surface structure plays an important role in the outcome of crystallization. This thesis reports the two-dimensional crystallization of non-functionalized helicenes on different single crystal metal substrates.

We demonstrate that the substrate metal and in particular its symmetry has a significant influence on conglomerate or racemate formation of racemic heptahelicene (*rac*-[7]H). On Cu(111), Ag(111) and Au(111) racemic zigzag rows are formed in the monolayer, exhibiting enantiomorphism only on the Cu(111) surface. In contrast thereto, a conglomerate forms on Cu(100), showing that the substrate symmetry has a significant influence on racemate or conglomerate formation and can be more important than the substrate metal. However, a different behavior is observed on Ag(100), where homochiral quadruplets are formed at very low coverage and heterochiral zigzag rows start to form at higher coverage. With increasing coverage the number of zigzag rows compared to quadruplets increases, until in the saturated monolayer only ordered zigzag rows are left. These rows run along the high symmetry surface direction and show no enantiomorphism.

The adsorption of a [5,6,9,10]-dibenzopentahelicene (db[5]H) racemate on Au(111) leads to 2D conglomerate formation, i. e. mirror domains containing only one enantiomer are observed, which is in contrast to previous results obtained for [7]H on Cu(111) and here observed for [7]H on Ag(111)

and Au(111). In order to study diastereomeric recognition processes based purely on van-der-Waals interactions, *M*-[7]H is mixed into the *rac*-db[5]H monolayer. This leads to a gradual shift in the balance between the mirror domains, until only the *P*-db[5]H enantiomorph is left in a monolayer containing 26% *M*-[7]H. This is explained by a preferred diastereomeric interaction between different helicene species of opposite handedness, suppressing the formation of the pure *P*-db[5]H enantiomorph by capturing *P*-db[5]H in non-ordered areas. A similar effect has only been observed for polar tartaric acid on Cu(110), where hydrogen bonds were identified as driving force for the domain suppression. These results show that dispersive forces can act in a manner comparable to polar forces in chiral discrimination at surfaces.

As soon as the coverage is increased above the saturated monolayer coverage, all structures of *rac*-[7]H and *rac*-db[7]H change significantly. In contrast to the racemic zigzag rows formed by *rac*-[7]H in the monolayer, the second layer is homochiral and it grows on a bottom layer of opposite handedness. Furthermore, the second layers on Au(111) and Ag(111) exhibit enantiomorphism. In the case of *rac*-db[5]H the bottom layer could be imaged at second layer boundaries, showing a different structure than the monolayer. Furthermore, the second layer of *rac*-db[5]H exhibits polymorphism and in addition to the homochiral domains, a racemic second layer structure is observed. These structural changes are the result of additional interlayer molecule-molecule interactions during crystal growth and a higher crystallization temperature of the double layer.

Single Bisheptahelicene (bis[7]H) molecules and small clusters are studied at low temperatures on Cu(111) in order to support the structure determination of previous studies on bis[7]H monolayers. Thereby, molecular dimers are a motif present at low coverage as well as a building block in a monolayer structure. The relative alignment of the molecules in a dimer is determined by picking apart single dimers with the STM tip.

In first measurements of single pentahelicene ([5]H) molecules on Cu(111), a preferred direction of rotational motion depending on the helicity is found, induced by inelastic electron tunneling. Additionally, homochiral dimer formation is observed.

Zusammenfassung

Chiralität ist allgegenwärtig in der Natur. Die wichtigsten Bausteine des Lebens, zum Beispiel Aminosäuren, Saccharide und Nukleotide, sind chiral und jeweils nur ein Enantiomer kommt in der Regel in der Natur vor. Chirale Erkennungsprozesse zwischen diesen Biomolekülen spielen daher eine bedeutende Rolle für das Leben. Des Weiteren sind sie verantwortlich für die spontane Enantiomerentrennung während der Kristallisation eines Racemates oder die diastereomere Salzkristallisation. Dabei fällt nur ein Enantiomer eines Racemates bei der Kristallisation mit einer enantiomerenreinen Verbindung aus. Die Enantiomerentrennung durch diesen Effekt ist eine wichtige Methode in der Industrie. Es ist jedoch nicht möglich, das Ergebnis einer Kristallisation allein anhand der Molekülstruktur vorherzusagen, da sehr kleine Struktureinflüsse durch die grosse Anzahl an Molekülen verstärkt werden und so das Ergebnis bestimmen. Diese Komplexität erfordert das Studieren geeigneter Modellsysteme, zum Beispiel zweidimensionale Molekülkristalle auf Metalloberflächen. Dabei können mit Hilfe der Rastertunnelmikroskopie Molekülstrukturen aufgelöst und abgebildet werden. Zusammen mit der im Vergleich zu dreidimensionalen Kristallen einfachen räumlichen Anordnung in zwei Dimensionen ist die Untersuchung von spezifischen molekularen Wechselwirkungen möglich. An helikalen aromatischen Kohlenwasserstoffen, sogenannten Helicenen, als chirale Moleküle ohne funktionale Gruppen bzw. tetragonales Kohlenstoffatom, können gezielt Wechselwirkungen studiert werden, die rein auf van-der-Waals Kräften basieren. Neben den Wechselwirkungen zwischen den Molekülen spielt die Oberfläche bei heterogenem Kristallwachstum und der Nukleation eine entscheidende Rolle, wodurch die Oberflächenstruktur das Kristallisationsergebnis entscheidend beeinflussen kann. In dieser Arbeit wird die zweidimensionale Kristallisation von nicht-funktionalisierten Helicenen auf verschiedenen einkristallinen Metalloberflächen beschrieben.

Wir zeigen, dass die Wahl der Metalloberfläche und insbesondere dessen Symmetrie einen bedeutenden Einfluss auf die Bildung eines Racemates oder Konglomerates razemischer Heptahelicene (*rac*-[7]H) hat. Auf Cu(111), Ag(111) und Au(111) werden racemische zickzack Reihen gebildet, welche nur auf Cu(111) enantiomorph sind. Im Gegensatz dazu bildet sich ein Konglomerat auf Cu(100), wodurch ein bedeutender Einfluss der Oberflächensymmetrie auf Racemat- oder Konglomeratbildung deutlich wird. Ein anderes Verhalten zeigt sich auf Ag(100). Bei einer geringen Bedeckung bilden sich homochirale *quadruplet* Motive und bei zunehmender Bedeckung bilden sich racemische zickzack Reihen. Die relative Anzahl der zickzack Reihen im Vergleich zu den quadruplet Motiven nimmt mit steigender Bedeckung zu, bis in der gesättigten Monolage ausschliesslich geordnete zickzack Reihen verbleiben. Diese laufen entlang der hochsymmetrischen Oberflächenrichtung und weisen keinen Enatiomorphismus auf.

Im Gegensatz zu der Racematbildung von [7]H auf Cu(111), Ag(111) und Au(111) entsteht bei der Adsorption eines [5,6,9,10]-dibenzopentahelicen (db[5]H) Racemates auf Au(111) ein Konglomerat mit Spiegeldomänen, die jeweils aus nur einem Enantiomer bestehen. Durch das Hinzufügen von *M*-[7]H in die Monolage verschiebt sich das Verhältnis der beiden Spiegeldomänen graduell, bis in einer Monolage mit 26% *M*-[7]H ausschliesslich der *P*-db[5]H Enantiomorph verbleibt. Dieser Effekt wird durch bevorzugte diastereomerische Wechselwirkungen zwischen den beiden Helicenarten mit gegenteiliger Händigkeit hervorgerufen. Dadurch wird *P*-db[5]H in ungeordneten Bereichen gebunden und die Bildung des *P*-db[5]H Enantiomorphs verhindert. Ein ähnlicher Effekt wurde bislang nur bei der Adsorption von polarer Weinsäure auf Cu(110) beobachtet, wo Wasserstoffbrückenbindungen als Ursache ausgemacht wurden. Somit zeigen unsere Ergebnisse, dass dispersive Wechselwirkungen eine ähnliche Rolle wie polare Wechselwirkungen in der chiralen Erkennung auf Oberflächen einnehmen können.

Sobald die Bedeckung über die gesättigte Monolage hinaus erhöht wird, tritt eine drastische Veränderung in den Strukturen von *rac*-[7]H und *rac*-db[7]H auf. Im Gegensatz zu den racemischen zickzack Reihen in der Monolage besteht die zweite Lage aus Molekülen gleicher Chiralität. Ebenso die darunter liegende erste Lage, jedoch aus Molekülen der entgegengesetzten Händigkeit. Ein weiterer Unterschied zur Monolage ist der auftretende Enantiomorphismus in der zweiten Lage auf Au(111) und Ag(111). Im Fall von *rac*-db[5]H kann die erste Lage an den Übergängen zur zweiten Lage abgebildet werden. Dabei zeigt sich eine andere Struktur als in der Monolage. Desweiteren zeigt die zweite Lage Polymorphismus und neben der homochiralen bildet sich u. a. eine razemische Struktur. Die Unterschiede zwischen den Strukturen der Mono- und Doppellage können auf zusätzliche Wechselwirkungen zwischen Molekülen in beiden Lagen während des Kristallwachstum und eine höhere Kristallisationstemperatur für die Doppellage zurück geführt werden.

Zur Unterstützung einer Strukturbestimmung von früheren Messungen einer Monolage Bisheptahelicene (bis[7]H) auf Cu(111) sind einzelne Moleküle und kleinere Cluster bei tiefen Temperaturen untersucht worden. Dimere bestehend aus zwei Molekülen treten sowohl bei geringer Bedeckung als auch in der gesättigten Monolage auf. Mit Hilfe von Manipulationsexperimenten ist die Lage der Moleküle in einem Dimer und somit der Monolage bestimmt worden.

Erste Experimente mit einzelnen Pentahelicenen ([5]H) auf Cu(111) zeigen nach der Anregung durch inelastische Tunnelelektronen eine bevorzugte Rotationsrichtung. Die Richtung hängt dabei von der Helizität ab. Neben den einzelnen Molekülen wird die Bildung von homochiralen Dimeren beobachtet.

1 Aim of this Thesis

Although the self-assembly and 2D crystallization of racemic and enantiopure [7]H has been extensively studied, there have been no studies focusing on the influence of the substrate metal and symmetry on 2D crystallization so far. Moreover, conglomerate formation has only been observed in the self-assembly of helicenes with polar groups and racemate formation for non-functionalized helicenes. This leads to the following open questions:

- What influence has the substrate metal and its symmetry on the self-assembly of [7]H?
- Are polar groups necessary for conglomerate formation of helicenes?

Adsorbing an enantiomeric excess of [7]H on Cu(111) resulted in amplification of chirality, which was possible because of the racemic composition of the enantiomorphous domains. Chiral bias in a conglomerate led to the suppression of one enantiomorph in the case of tartaric and malic acid on Cu(110). Thereby, hydrogen bonds were identified as driving force for the diastereomeric recognition process, giving rise to the following question:

- Are polar forces required for this kind of diastereomeric recognition?

In general, the studies involving helical molecules on surfaces focused on the self-assembly and formations of ordered molecular structures on the surface, but no manipulation experiments were performed or chirality switching has been tried in order answer the following question:

- Is it possible to switch the chirality of single helicene molecules via inelastic electron tunneling (IET)?

These questions are of keen interest nowadays, not only for the surface science community, and are treated in this thesis.

2 Introduction

For a better understanding of this work, the concept of chirality and its implications will be shortly described. It starts with a discovery made by Pasteur in 1848, when he manually separated left-handed from right-handed sodium ammonium tartrate crystals due to their different shapes, which are mirror images of each other (Fig. 2.1c). Aqueous solutions of the separated crystals showed opposite optical activity[1]. The term "chiral" comes from the Greek word for hand, Χειρ, and was later coined by Kelvin in 1904 and more precisely specified by Prelog as "an object is chiral, if it cannot be brought into congruence with its mirror image by translation and rotation. Such objects are devoid of symmetry elements which include reflection: mirror planes, inversion centres and improper rotational axes."[2] Two mirror images that are non-superimposable are also called enantiomorphous. The hand as an example for a macroscopic chiral object is illustrated in Fig. 2.1a. Compared to the chair as example for an achiral object, a hand is not superimposable with its mirror image. This concept also applies to molecules, e. g. a tetragonal carbon atom with four different substituents can be arranged in two ways that are mirror images of each other. These mirror images are then called enantiomers and a mixture containing both in an equal ratio is called a racemate. Upon crystallization, molecular symmetry can be transferred into a macroscopic crystal, as it is the case for sodium ammonium tartrate crystals as illustrated in Fig. 2.1c. Thereby, the enantiomers separate into two enantiomorphous crystals that are mirror images of each other.

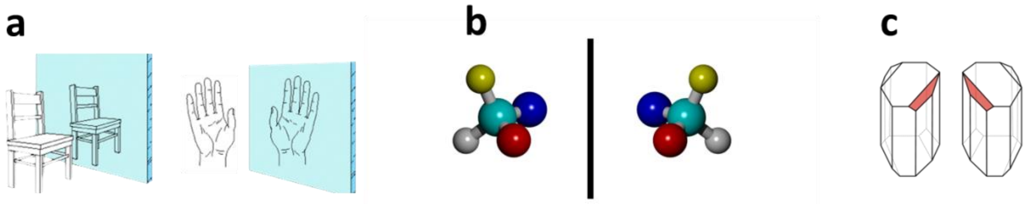

Fig. 2.1: a) Examples for an achiral (chair) and chiral (hand) object. Achiral objects and their mirror images are identical and can be superpositioned with each other, which is not possible for chiral objects. **b**) Two enantiomers of a tetragonal carbon with four different substituents. **c**) Enantiomorphous sodium ammonium tartrate crystals.

As in 3D crystals, upon adsorption on a surface, chiral molecules may crystallize as a racemate, conglomerate or a solid solution as illustrated in Fig. 2.2. In a racemic crystal, both enantiomers are incorporated at equal ratio, whereas they are laterally separated in a conglomerate, i. e. two enantiopure domains are formed that are mirror images of each other. In a solid solution both enantiomers are distributed randomly in the crystal.

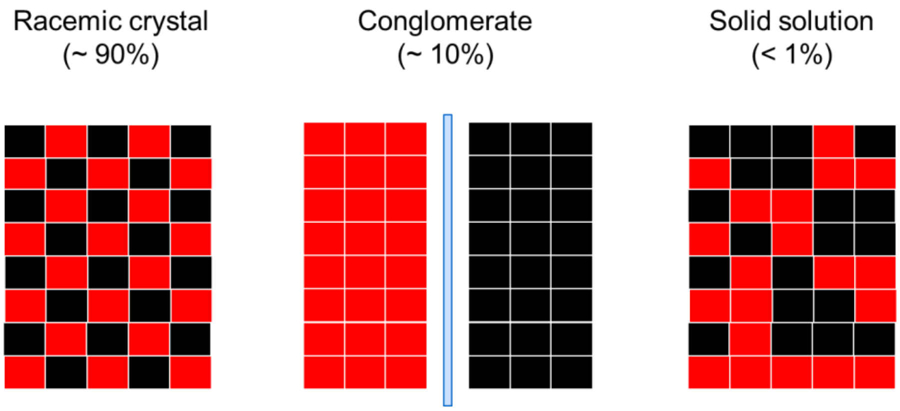

Fig. 2.2: Possibilities for the crystallization of chiral and prochiral molecules at surfaces. In 3D crystals about 90% of the known chiral molecules crystallize as a racemate, 10% separate into a conglomerate and less than 1% form a solid solution.

If only one enantiomer is adsorbed on the surface, the formed homochiral structure is the mirror image of the structure formed upon adsorbing the opposite enantiomer, similar to the conglomerate shown in Fig. 2.2. Furthermore, if a racemic mixture forms a conglomerate, the structure formed by one enantiomer is in general identical to the enantiomorph in the conglomerate of the corresponding enantiomer. In contrast thereto, if chiral molecules form a racemic structure upon adsorption, adsorbing only one enantiomer of the molecule may lead to a different crystal structure.

Enantiomers have identical physical and chemical properties, if they are in an achiral environment. As soon as the environment is chiral, the chirality starts to play an important role and both enantiomers can show significantly different behavior. Most of the important biomolecules, e. g. amino acids, saccharides, nucleotides and vitamins, are chiral and exist in nature only in one enantiomeric form. Helicity as a form of chirality appears, for example, in the DNA and α-helix structure in proteins. Thus, the question of racemate or conglomerate formation and the underlying molecular recognition processes among chiral biomolecules play a key role in the homochiral imperative of molecular evolution[3] and are of fundamental importance to life. Furthermore, they play a key role in the performance of liquid crystals[4] and in phenomena like spontaneous resolution of enantiomers in the crystallization of a racemate or their separation via diastereomeric salt crystallization. Established in 1893 by Pope and Kipping[5], it is the most important technique to separate enantiomers in industry even today[6]. Therefore, a racemate of the compound that shall be separated is mixed with another enantiopure compound. The enantiomers can then be separated, if only one enantiomer crystallizes with the enantiopure compound.

The crystallization outcome of given molecules is still difficult to predict, and due to their complexity the responsible molecular recognition processes are poorly understood[7]. That is, extremely small structural influences become amplified by many cooperating units and govern the macroscopic result of the crystallization. This complexity calls for an appropriate model system to understand the nature and consequences of intermolecular interactions. A promising approach is the investigation of two-dimensional (2D) crystals of organic molecules on single-crystal substrates, where scanning tunneling microscopy (STM) provides submolecular resolution. This resolution and the relatively simple spatial molecular ordering compared to 3D crystals[8] enables the detailed study of specific interactions of single chiral molecules in mono- and multilayers[9,10].

For the discussion of ordered molecular layers on crystalline surfaces, it is useful to describe the alignment of the molecules relative to the substrate lattice. There are two ways describing this relation. One is the Wood notation[11], which is useful to describe simple patterns. More precise is the transformation matrix, which links the substrate lattice vectors (a_s and b_s) to the adsorbate lattice (a and b), as introduced by Park and Madden[12]. Such a transformation matrix is given by

$$\begin{pmatrix} a \\ b \end{pmatrix} = \begin{pmatrix} m_{11} & m_{12} \\ m_{21} & m_{22} \end{pmatrix} \begin{pmatrix} a_s \\ b_s \end{pmatrix}.$$

However, the lack of unambiguous specification for unit cell selection leads to different possible matrices for equivalent patterns. Therefore, the proper choice of unit cells requires strict rules for an unambiguous and consistent denotation of matrices. Consequently, a protocol for “master matrix” selection was developed by Merz and Ernst[13], which is applied here for all adlattices.
For further reading and examples on molecular chirality at surfaces see the review articles [9,10,14-16] and for a short review on the effects of a chiral bias on solid surfaces see reference [17].

Upon adsorption on a crystalline surface of a given molecule, there is often an energetically favored adsorption site. As shown later, heptahelicene adsorbs with three benzene rings parallel to the surface on Cu(111). Therefore, phenantrene is chosen as example molecule in Fig. 2.3 to illustrate the adsorption site concept used to discuss the results. With preferred adsites, a crystalline surface can be described as adsorption grid for molecules that allows only certain intermolecular distances. As illustrated in Fig. 2.3, certain positions on this grid may be preferred (b). One step closer may result in a too strong overlap (a) and one step further away in no or very small attractive interactions (c). Interestingly, the lattice constant of Cu(111) fits the size of benzene rings in planar aromatic hydrocarbons, which allows for the three rings of phenantrene to be located on identical adsorption sites only for certain orientations (Fig. 2.3d). This is not the case on the Au(111) or Ag(111) surface due to their larger lattice constants. Hence, the benzene rings are not able to sit on identical adsorption sites, which may lead to lower adsorption energies.

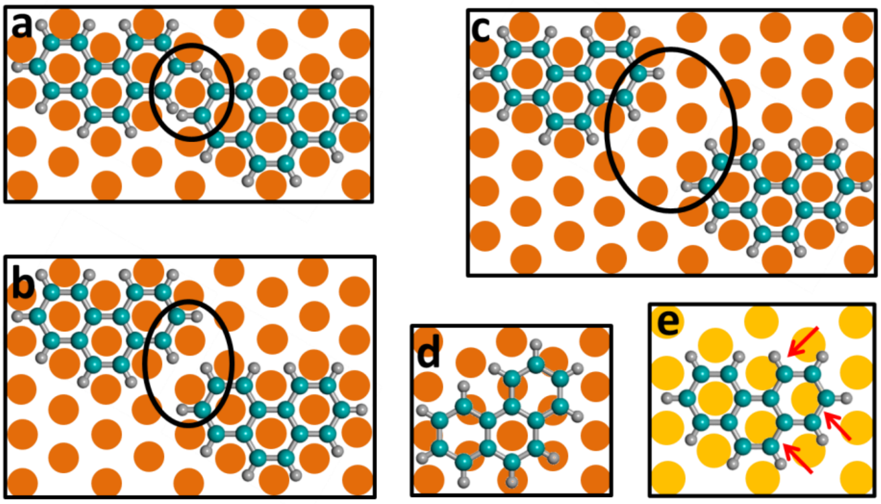

Fig. 2.3: Schematic illustration of the adsorption grid concept with phenantrene as example molecule. If only certain adsorption sites are allowed the grid provided by a Cu(111) surface then allows only certain possibilities with all three rings on identical sites. For example, the specific adsites can be thought of as the Cu atoms being underneath the center of the benzene rings. Only the positions of the molecules shown in **b** would allow attractive interactions. In the position shown in **a** the overlap of the molecules is too strong and in **c** the molecules are too far apart. **d**) Only certain orientations are possible under the premise of identical adsites. **e**) Due to the larger lattice constant on Au(111), the three benzene rings cannot sit on identical adsites as on Cu(111).

2.1 Helicenes

2.1.1 General Properties

Helicenes consist of ortho-fused benzene or other aromatic rings that form a non-planar screw shaped molecular backbone. Steric overcrowding of the terminal rings leads to the helical shape and, if both ends are identical, C_2 symmetry. Thus, helicenes are chiral without having tetragonal asymmetric carbon atoms (Fig. 2.4).

The denotation hexahelicene for phenantro[3,4-*c*]phenantrene was first introduced in 1956 by Newman and Lednicer[18] for simplifying the rather complex IUPAC nomenclature. A number *n* in brackets [*n*] before the name accounts for the number of aromatic rings in the molecular backbone. Helicenes that are built up exclusively by benzene rings are called carbohelicenes, whereas heterohelicenes contain at least one heteroatom in the molecular backbone[19]. All molecules studied in this work belong to the class of carbohelicenes and thus, for the sake of simplicity, the term "helicenes" will in general refer to carbohelicenes, here.

According to the helicity rule by Cahn, Ingold and Prelog[2], a left-handed helix is referred to as "minus" and indicated by *M*, whereas a right handed one is referred to as "plus" and indicated by *P*, as shown in Fig. 2.4 with heptahelicene as an example.

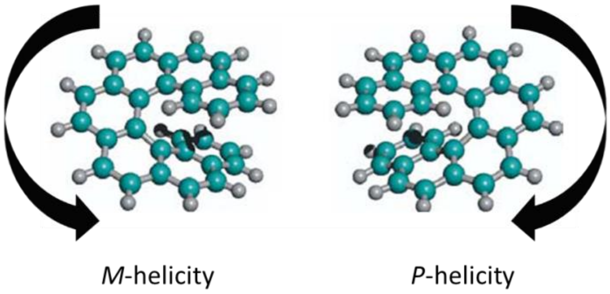

Fig. 2.4: Ball-and-stick molecular models of *M*- and *P*-heptahelicene.

With increasing number of fused aromatic rings in a molecule, they spiral further in the direction of the helical axis, whereby a full 360° rotation is completed after six rings in the case of *ortho* fused benzene rings[20]. The amount of the helix overlap has obviously a high influence on the racemization barriers of helicenes, i. e. the thermal conversion between both enantiomers. The kinetic data for the thermal racemization of [5]-[21], [6]-, [7]-, [8]- and [9]helicene[22] has been determined previously. While the Gibbs free energy increases from [5]H ($24.1\frac{kcal}{mol}$) over [6]H ($36.2\frac{kcal}{mol}$) to [7]H ($41.7\frac{kcal}{mol}$), it does not increase significantly for the higher helicenes [8]H ($42.4\frac{kcal}{mol}$) and [9]H ($43.5\frac{kcal}{mol}$). For the racemization mechanism a transition state with C_s symmetry was calculated for [6]H and [7]H, while a planar C_{2v} symmetry was found for [5]H[23].

One peculiar property of helicenes is their polarizability, making them good π-donors that can form charge-transfer complexes with many π-acceptors[24,25]. Additionally, they have interesting chiroptical properties, like high optical rotation and pronounced circular dichroism[26-29], but a fluorescence with moderate quantum yields.[30].

For more detailed reviews on the general properties and some resulting applications, e. g. in liquid crystals, nonlinear optic materials or polymers of helicenes see references [31] and [32].

2.1.2 Synthesis

The first synthesized carbohelicene was [4]helicene by Weitzenböck and Lieb in 1913[33], followed by the synthesis of [5]helicene by Weitzenböck and Klingler in 1918[34,35]. After this early work, it took almost 40 years until the synthesis of [6]helicene by Newman and co-workers in 1955 and the highly innovative enantioresolution via a charge-transfer comlex[18,36]. The next milestone in helicene chemistry was the photochemical synthesis of [7]helicene by Martin and co-workers in 1967[37], opening up the way to the preparation of higher helicenes and the studies of the physicochemical properties of helicenes. A major improvement in the synthesis of helicenes in large quantities was a Diels-Alder approach developed by Katz and co-workers in 1990 for producing functionalized [5]- and [6]helicenes[38]. Since then, a variety of strategies for the synthesis of helicenes have been developed. A detailed summary of the synthetic methods to obtain helicenes would be beyond the scope of this thesis. Thus, only the synthetic routes to the studied helicenes are shown briefly in the experimental section and the reader is referred to the reviews [30,31,39] and references therein. For a review focused on the stereoselective synthesis and the chiral separation of helicenes see reference [40].

2.1.3 Previous Work on the Self-Assembly of Helicenes

For the discussion of our results it is required to discuss in detail previous findings on the self-assembly of 7[H] on Ni and Cu surfaces, as studied by Ernst *et al.*. At first, the intact adsorption of [7]H after sublimation at 160 °C was confirmed by time-of-flight secondary ion mass spectrometry (ToF-SIMS) measurements[41] and a quasi-hexagonal 4×4 superstructure was observed by means of STM at room temperature on Ni(111)[42]. In the saturated monolayer of *P*-[7]H on Ni(100) an angle of $43 \pm 5°$ between the helical axis and the surface plane was observed[43]. In contrast to that, X-ray photoelectron diffraction (XPD) studies of *M*-[7]H on Cu(111) showed that the molecules are aligned with their terminal phenantrene group parallel to the surface and the helix is spiraling away from the surface (Fig. 2.5). Six coexisting azimuthal molecular orientations were found[44].

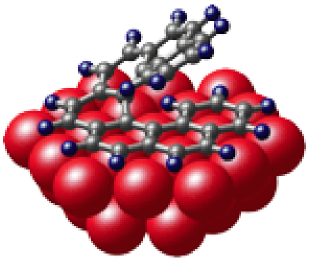

Fig. 2.5: Molecular orientation of *M*-[7]H on Cu(111)[44].

In early LEED studies of racemic and enantiopure [7]H on Cu(111) mirror domains were observed in the case of *rac*-[7]H, but not for enantiopure [7]H and it was concluded, that in the saturated monolayer of the racemate the enantiomers separated into mirror domains[45]. However, STM measurements showed different structures for *rac*-[7]H and enantiopure [7]H[46].

Furthermore, the STM studies on Cu(111) showed that racemic [7]H forms different structures depending on the coverage. An overview of the structures of *rac*-[7]H at different coverages is given in the following Fig. 2.6[47].

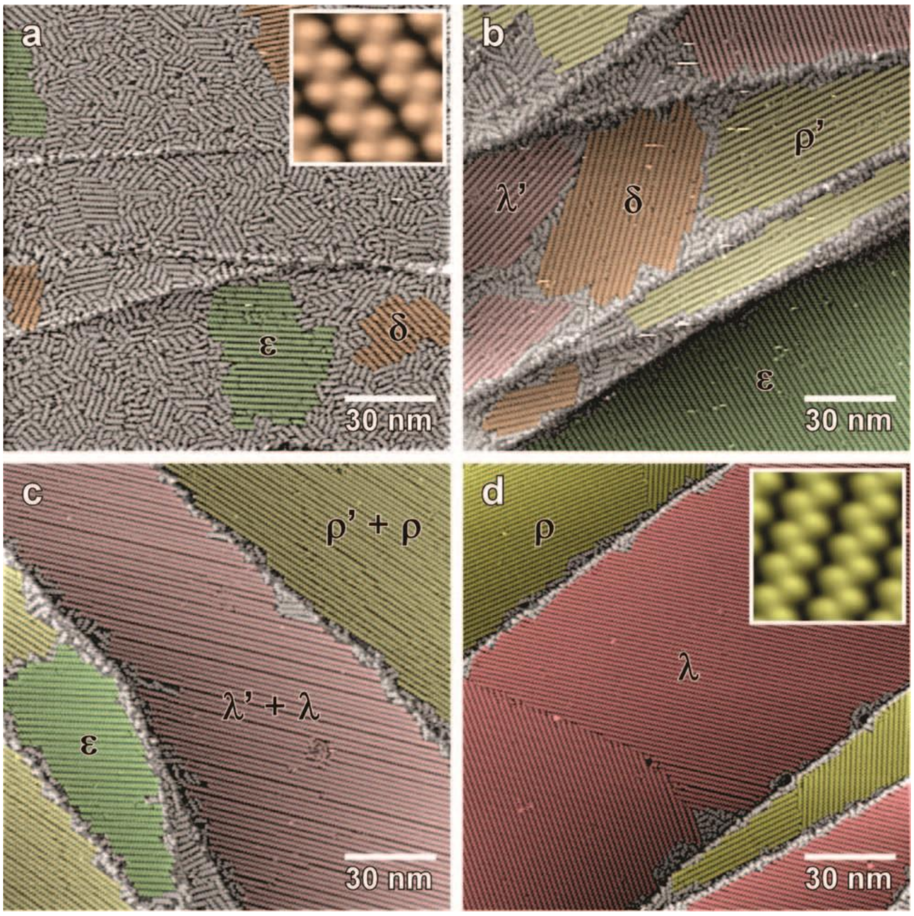

Fig. 2.6: STM images (150 nm x 150 nm) showing different structures and enantiomorphous domains of *rac*-[7]H on Cu(111) with increasing coverage (θ = 0.59 (a), 0.71 (b), 0.85 (c), 0.93 (d)).[47]

For *rac*-[7H] overall three pairs structures showing mirror symmetry were observed with increasing coverage, named ε/δ, λ'/ρ' and λ/ρ. The insets in Fig. 2.6 show that all structures consist of molecular zigzag rows. The difference of the ε/δ structures compared to the λ'/ρ' or λ/ρ, respectively, is the angle between the rows and the close-packed $[1\bar{1}0]$ surface direction. In the ε/δ structures, the angle is ± 22° ± 2.2° and in the λ'/ρ' and λ/ρ the angle is ± 10.5° ± 0.8°. Thus, the enantiomorphous domains are the result of opposite oblique tilt angles between the adlattice, i. e. the zigzag rows, and the surface lattice. With the mentioned tilt angle and distance between the molecules in a double row being identical in the λ'/ρ' and λ/ρ structures, the only difference is the distance between the zigzag rows, which are packed slightly denser in the λ/ρ structures[47].

Heterochiral pairs as building blocks for the zigzag rows were identified by molecular modeling calculations for the λ/ρ phase[48]. Additionally, the exact positions of the molecules within a row were determined by high resolution STM images in cooperation with extended Hückel simulations. The alignment of the molecules is shown in Fig. 2.7[47] by overlapping the molecular frames with a highly resolved STM image.

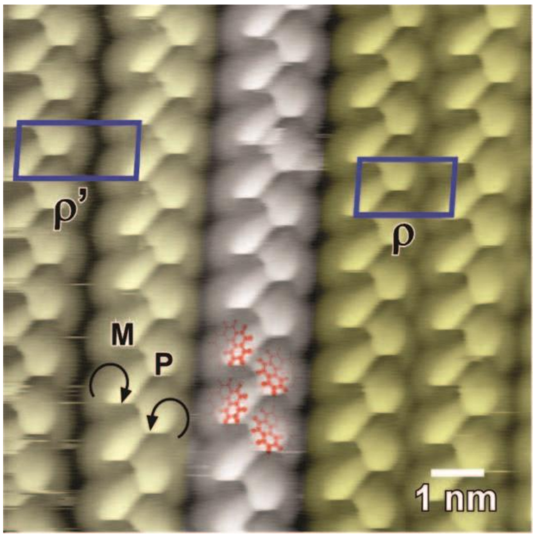

Fig. 2.7: High resolution STM image (10 nm x 10 nm) of the ρ and ρ' structures of *rac*-[7H] on Cu(111). The zigzag rows are formed by heterochiral pairs. The only difference between both structures is the absolute distance between every second row. The positions of the molecules are indicated for two heterochiral pairs in the middle row.[47]

The molecules in one heterochiral pair are rotated by 60° with respect to each other. Including adjacent rows gives a distorted hexagonal packing for the molecules, which appear as zigzag rows due to their different azimuthal orientations.

Since the zigzag rows contain both enantiomers, pure heptahelicenes formed different structures on Cu(111). Depending on the coverage, three different structures were formed, all shown in Fig. 2.8[47]. These findings are equally relevant here, because similar structures are described in this work for pure enantiomers on Au(111) and Ag(111).

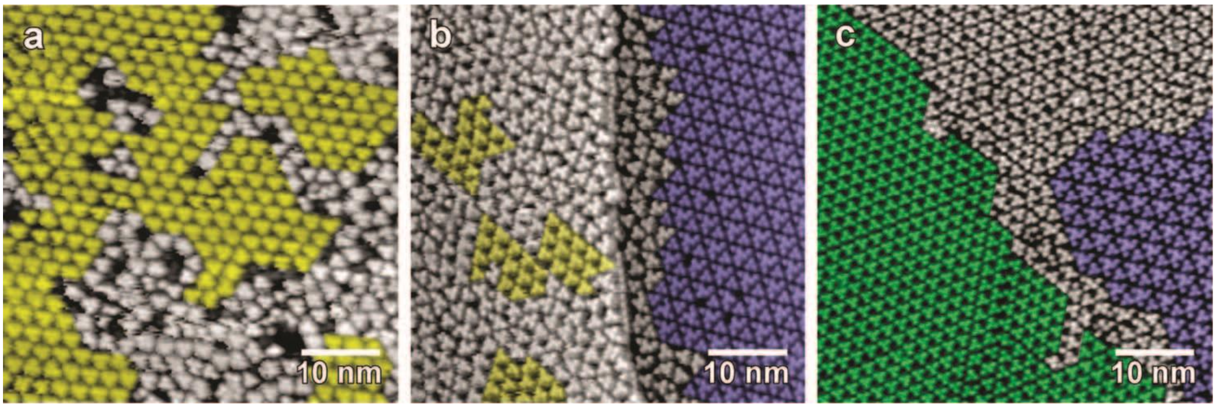

Fig. 2.8: STM images (50 nm x 50 nm) of the different structures of enantiopure [7H] on Cu(111). The coverage increases from left to right. (**a**) *P*-[7H], $\theta = 0.63$, (**b**) *M*-[7H], $\theta = 0.84$, (**c**) *M*-[7H], $\theta = 0.96$.[47]

Starting at a coverage of about 66% of the saturated monolayer, the molecules formed ordered clusters composed of three molecules (α phase, yellow in Fig. 2.8). At higher coverages the repeating feature is a 6&3 molecule unit (β phase, blue in Fig. 2.8). After further increasing the coverage, the densest structure appears as clusters of three molecules (γ phase, green in Fig. 2.8). All three structures may coexist at lower coverages, but the saturated monolayer ($\theta = 1.0$) is exclusively composed of the γ phase.

Molecular modeling calculations performed for the γ phase showed that the structure is also hexagonal and the appearance in the STM images comes from the azimuthal orientations of the molecules[49]. In each cluster the three molecules are rotated by 120° with respect to each other. The tilt angle of the adlattice and the $[1\bar{1}0]$ surface direction is 13.3° ± 2.7°. Using the opposite enantiomer leads to a mirror symmetric structure with the opposite tilt angle of the adlattice and also opposite tilts of the molecules within the adlattice unit cell[49].

A kind of chiral amplification was observed after inducing additional chiral bias in the monolayer of *rac*-[7]H on Cu(111), i. e. an enantiomeric excess (ee) of one enantiomer led to a drastic shift in the ratio between the λ and ρ phases in the saturated monolayer[48]. In a monolayer consisting of 54% *M*-[7]H and 46% *P*-[7]H (ee = 0.08), exclusively λ domains were observed, as shown in Fig. 2.9. At larger ee less ordered, residual areas (marked grey in Fig. 2.9) appeared. They consist of small zigzag rows and structural features characteristic for the pure enantiomers. The size of these residual areas increased linear with increasing ee (Fig. 2.9b). Therefore, it was concluded that the composition of the λ domains does not change with ee and the excess of *M*-[7]H must be accumulated outside the ordered domains.

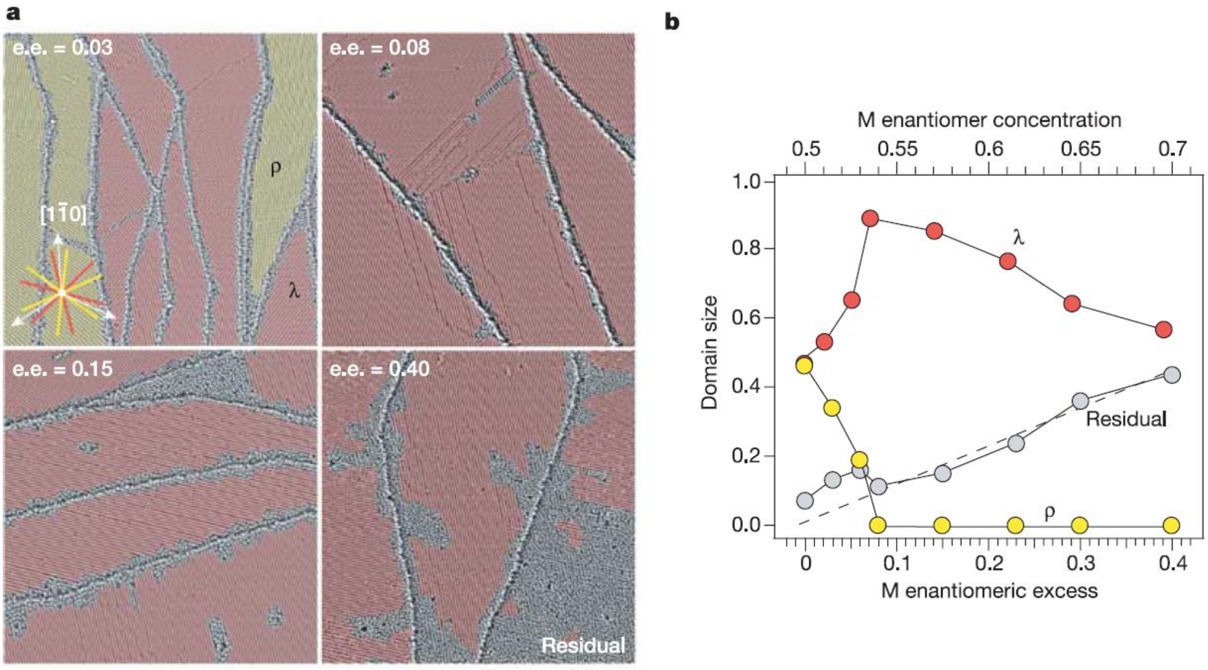

Fig. 2.9: a) Series of STM images (200 nm x 200 nm) with increasing ee. The λ domains are marked red, ρ domains yellow. **b**) Relative sizes of λ (red circles) and ρ domains (yellow circles) for increasing ee, determined from several images as shown in **a**. The "residual areas" (grey circles) consist of small clusters and short zigzag rows.[48]

The drastic change in the balance between both enantiomorphous domains after inducing a small chiral bias was explained by energy differences in the boundaries between mirror domains, rotational domains and the domain/residual area interface. Molecular mechanics calculations showed that mirror domain boundaries have twice the energy then rotational domain boundaries. Additionally, the calculations showed an energetically favored interaction between λ domains edges interacting with an excess of *M*-[7]H and ρ domains interacting with *P*-[7]H, respectively. Thus, the chiral bias is induced by the excess of one enantiomer in the residual areas: the energy difference at the domain/residual boundaries represents a "chiral field" that slightly favors the growth of only one enantiomorphous domain and the energetically unfavorable mirror domain boundaries further prevent the formation of the corresponding mirror domain.

In the second layer of enantiopure [7]H profound differences are observed with respect to the first layer structure (Fig. 2.10)[50].

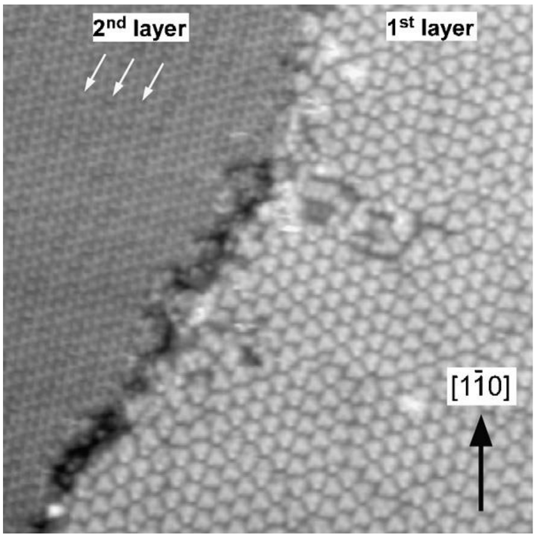

Fig. 2.10: STM image (50 nm x 50 nm) showing *M*-[7]H on Cu(111). Adjacent terraces are covered by a monolayer and a double layer, respectively. A one-dimensional Moiré pattern in the second layer is marked by white arrows.

The second layer started to grow only after the first layer was completely saturated. Due to the observed Moiré pattern a quasi-epitaxially growth was assumed with a lattice mismatch between both layers on a small scale and a coincidence on a larger scale. Within the second layer, the molecules are ordered in a hexagonal fashion. The unit cells of the Moiré patterns adlattice and the $[1\bar{1}0]$ surface direction include opposite oblique tilt angles for the *M*- and *P* enantiomers. Hence, the Moiré pattern transfers the molecular chirality into a larger scale. Furthermore, the second layer exhibited polymorphism with four different, coexisting structures per enantiomer.

Unpublished previous work on the second layer growth of *rac*-[7]H on Cu(111) by Parschau *et al.*[51] showed that extended second layer islands of *rac*-[7]H on Cu(111) are formed as soon as the coverage is slightly increased above the saturated monolayer coverage. Additionally, no long range ordered domains remain in the first layer on the entire surface and only small domains containing a few short zigzag rows are left, in which the rows have the orientation of the λ/ρ structures.

With increasing coverage the 2nd layer domain size also increases until a complete 2nd layer is formed. As in the monolayer two enantiomorphous domains are formed, which have identical lattice density and orientation with respect to the Cu(111) substrate compared to the λ'/ρ' structure observed in the racemic monolayer, but with only one molecule in the unit cell. The matrix notation of the adlattice is $\begin{pmatrix}4 & -1\\ 3 & 5\end{pmatrix}$. High resolution STM images show that the second layer consists only of one enantiomer and a comparison with the contrast of the enantiopure second layer allows the determination of the absolute handedness. The second layer with identical orientation than the λ' structure consist of *M*-[7]H and the second layer on the ρ' structure of *P*-[7]H, respectively.

Compared to the enantiopure 2nd layer, there is no further pattern like Moiré pattern, what implies the absence of any lattice mismatch between the first and second layer. Therefore the second layer grows epitaxially on the first layer and the density is identical in both layers. Compared to the close-packed λ/ρ structures in the first layer the density in the second layer is reduced by 24%. Thus the additional molecule-molecule interactions between both layers influence the molecule-substrate interactions and the density in the bottom layer is also reduced due to the presence of the second layer.

Other helicene derivatives on surfaces

Related studies on the self-assembly in two-dimensions of carbohelicenes derivatives with substituents attached to the helical backbone and other helicenes will be described briefly.

A combined STM and DFT study of 6,13-dicyanoheptahelicene showed conglomerate formation on Cu(111)[52]. Two different polymorphs were found, consisting of dimers and tetramers, respectively. According to the DFT calculations, the main intermolecular forces were $CN \cdots HC(Ar)$ hydrogen bonds and dipolar $CN \cdots CN$ interactions. The spontaneous resolution was explained by more favorable interactions between the molecular dipoles resulting from a substrate-induced polarization and a higher number of intermolecular $CN \cdots HC(Ar)$ hydrogen bonds.

Supported by DFT calculations heptahelicene-2-carboxylic acid ([7]HCA) has been studied on the $(10\bar{1}4)$ cleavage plane of calcite by non-contact atomic force microscopy (nc-AFM). At low coverages well below the monolayer, a racemic mixture of [7]HCA formed wire-like structures, which grew on bare terraces and were unidirectionally aligned along the $(01\bar{1}0)$ surface direction[53,54]. In the full monolayer a 2×3 superstructure with two [7]HCA molecules in the unit cell was observed. The DFT calculations led to the conclusion that these wires consist of racemic double-rows, with the molecules standing in an upright position, which allows $\pi - \pi$ stacking of the molecules along a single row and hydrogen bond formation between the two adjacent rows in the structure. In contrast to the wire-like structures formed by the racemic mixture, enantiopure [7HCA] grew extended islands composed of rows directed along the $(01\bar{1}0)$ surface direction and a 2×3 superstructure within the islands[55].

Racemic mixtures of 7-bromopentahelicene (B[5]H) were studied by means of nc-AFM on Ag(001)[56] and on the Suzuki surface[a,57,58] of sodium chloride[59]. No ordered structures were observed after depositing B[5]H on Ag(001), which was ascribed to an insufficient mobility of the molecules on the

---

[a] The Suzuki phase is composed of alternating pure NaCl layers and layers with positive divalent impurities (Cd^{2+}in the mentioned work) and vacancies for compensating the additional valences. Inside a crystal, the Suzuki phase exists as three-dimensional cubes within the pure NaCl crystal. The cleavage of such a crystal leads to the *Suzuki surface* with areas of the pure NaCl and the Suzuki structure.

surface. In the case of the Suzuki surface of sodium chloride, the B[5]H molecules were found only in the Suzuki regions of the surface and at step edges, but not on the pure sodium chloride terraces.

At the liquid/solid interface the asymmetric substituted 5-aminohexahelicene (A[6]H) was studied on Au(111) and HOPG[60]. Enantiopure A[6]H on Au(111) formed a “three-dot” structure completely analogous to the UHV-γ phase of [7]H on Cu(111) (marked green in Fig. 2.8). The racemic mixture of A[6]H formed a racemic polymorph (38%) co-existing with a conglomerate of the “three-dot” structure (62%). On HOPG no stable self-assembly of monolayers of A[6]H could be observed.

[11]Anthrahelicene ([11]AH) is made of eleven benzene rings, whereby the central ring is *meta* annulated instead of *ortho*. A racemic mixture of this helicene was studied on the InSb(001) c(8x2) surface[61] and the (110) and (011) faces of TiO_2[62]. On the InSb surface [11]AH aligned in a quasi-hexagonal structure within 2D islands and the helical axis almost perpendicular to the surface. Small mirror domains were observed with a quasi-hexagonal ordering of the molecules in the domains on the (110) face of TiO_2. In contrast to that, no ordered structures were observed on the (011) surface of TiO_2.

Racemic hexathia[11]heterohelicene ([11]TH), consisting of five benzene and six thiophene rings, was investigated on polycrystalline gold surfaces, Au(111) and Au(110) by Taniguchi and co-workers[63-65]. On flat Au(111) terraces [11]TH formed a hexagonal lattice with a seemingly random distribution of the *M* and *P* enantiomers[63]. On Au(110) rows running along the $\{1\bar{1}0\}$ directions were observed, but the chirality of the molecules in each chain could not be determined[64]. In multistep regions homochiral molecular rows were observed[65]. In all cases the helical axis aligned almost perpendicular to the surface.

3 Experimental

3.1 Methods

All experiments were carried out in the Molecular Surface Science group at Empa – Swiss Federal Laboratories for Materials Science and Technology.

Unit cell models were prepared with the HyperChem™ Release 7.1 for Windows. For space-filling models the van-der-Waals radius given by the HyperChem software was used. The helicene molecules were aligned with three C6 rings parallel to the surface and the rest of the molecule spiraling away from the surface, a configuration that has been found for 7[H] on Cu(111) by photoelectron diffraction (see Fig. 2.5). The final images were rendered using POV-Ray™ Version 3.0. Unit cells were determined by the superpositioning of the adlattice and substrate lattice. The latter was known from atomically resolved STM images.

3.1.1 Ultra High Vacuum Systems

The STM measurements of [7]H on Ag(111), Au(111), Cu(100) and Ag(100) and db[5]H on Au(111) were performed with a commercial Omicron variable temperature STM apparatus. The system was pumped with a turbo molecular pump and an ion getter pump to a base pressure below $5 \cdot 10^{-10}$ mbar. It was equipped with the tunneling microscope, a water cooled evaporator and standard sample preparation facilities. Unless stated otherwise, the samples were kept at a temperature around 60 K during the STM measurements.

The single molecule measurements and manipulations of bis-[7]H and [5]H on Cu(111) were conducted with a prototype low temperature STM. The system consists of the sample preparation and the STM chamber, which are separated by a shutter. It was pumped with a turbo molecular pump and two ion getter pumps to a base pressure below $5 \cdot 10^{-10}$ mbar and below $5 \cdot 10^{-11}$ mbar in the STM chamber when cooled with liquid helium. The preparation chamber was equipped with a quadrupol mass spectrometer, spectraLEED optics from Omicron with a LaB_6 filament and standard sample preparation facilities. The STM chamber was equipped with the tunneling microscope attached to a 4.3 L cryostat. When cooled with liquid helium the STM had a temperature around 8 K.

3.1.2 Scanning Tunneling Microscopy

Scanning tunneling microscopy was invented by Binnig and Rohrer in 1982[66-69]. Originally the scanning tunneling microscope was developed to image the topography of surfaces, but it has been proven to be a very powerful and versatile tool in various fields, i.e. condensed matter physics, chemistry, materials science, biology and surface science. Additionally it allows the manipulation of single atoms and molecules via the tip. The timely awarded Nobel Prize in Physics for Binnig and Rohrer in 1986 also indicates the importance of their invention.

The conceptionally simple operation principle of STM is shown in Fig. 3.1. The main parts are a *XYZ* piezoelectric actuator (e. g. a piezoelectric tube) with the attached tip and a tunneling current amplifier. The distance control and scanning unit applies a bias between the tip and sample and moves the tip with the piezoelectric actuators with high precision. To take an image, the tip is moved across the surface and thereby, in the commonly used constant current scanning mode, the height of the tip is adjusted to keep the tunneling current constant. The change in tip height while moving across the surface is then recorded at e. g. 512 x 512 points and a three-dimensional dataset is obtained. In general, a STM dataset is represented by a false color image.

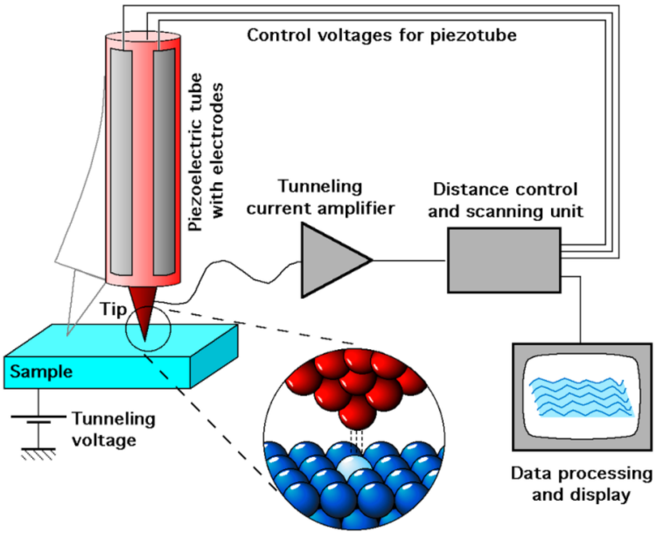

Fig. 3.1: Principal operating diagram of a scanning tunneling microscope.

The previously explained operation principle is based on the tunneling effect, which states that a particle has a finite probability to exist behind a potential barrier without overcoming it. In the case of electrons the tunneling probability, also called transmission coefficient, is given by the following equation.

$$T(E) \propto \frac{E}{V_0} \cdot e^{-ka}$$

Therein, E is the energy of the electron, V_0 the height of the potential barrier, k the momentum of the electron and a the width of the potential barrier. The transmission coefficient $T(E)$ and hence the tunneling current depend on the energy of the electrons, which can be adjusted by the applied bias. Furthermore, the tunneling current decays exponentially with increasing barrier width, i. e. distance between tip and sample. The barrier height V_0 represents the conduction of the tunneling gap, which in turn depends on the density of states in the surface and the tip. Thus, a STM image is always a representation of the surface topography superpositioned with the density of states. In addition to imaging, STM also allows manipulation of single atoms or molecules, i. e. by moving the tip very close to a molecule and applying a short voltage pulse the molecule can be picked up.

Further information on the STM technique can be found in reference [70], a good overview on the versatile applications is given in reference [71] and for an overview with a focus on atomic and molecular manipulation see reference [72]. A recent review on the manipulation of single atoms and molecules is given in reference[73].

Data Analysis

All processing of the STM images was performed using the WSxM 4.0 software[74] unless stated otherwise in the figure caption. All STM images shown are plane subtracted and flattened.

3.2 Materials

3.2.1 Metal Substrates

All single crystals used in the experiments were purchased from MaTeck GmbH showing a purity > 99.999%, a roughness < 0.03 µm and an orientation precision < 0.1°. Prior to the deposition of the molecules the cleanliness was checked by STM. The crystals were prepared by subsequent cycles of Ar^+ ion sputtering followed by annealing to 500 – 600 °C.

3.2.2 Molecules

Rac-[7]H was purchased from Chiracon GmbH (Luckenwalde, Germany). The separation of the enantiomers was achieved by high-performance liquid chromatography (HPLC) on a Daicel Chiracel OD column using an UV detector at 340 nm. Dibenzopentahelicene was synthesized by Oliver Allemann in the group of Prof. Dr. Jay S. Siegel at the University of Zürich. Bisheptahelicene and pentahelicene were synthesized in the group of Prof. Dr. Andreas Terfort at the University of Frankfurt. The routes used for the synthesis of pentahelicene, dibenzopentahelicene and bisheptahelicene are briefly shown in the appendix.

4 Enantiopure Heptahelicenes

The two-dimensional crystallization of *M*-[7]H was investigated on Cu(100), Ag(100), Ag(111) and Au(111) in order to compare the observed structures with *rac*-[7]H (Fig. 2.4) on these surfaces and determine whether the racemate forms a racemic structure or a conglomerate.

Unless stated otherwise, the measurements were performed with an Omicron Variable Temperature STM (see chapter 3.1.1). *M*-[7]H was evaporated from a Knudsen cell held at 160 °C onto the respective crystal kept at RT. After deposition, the crystal was cooled with liquid helium and held at approximately 60 K during the measurements.

4.1 On Cu(100)

The structure formed by enantiopure *M*-[7H] on Cu(100) in the saturated monolayer is shown in Fig. 4.1. Fig. 4.1a shows a large area STM image where all domains have the same orientation. The smaller area STM image in Fig. 4.1b shows that the domains consists of clusters with four molecules, which align in a $\begin{pmatrix} 8 & 2 \\ -2 & 8 \end{pmatrix}$ unit cell. A molecular model for this structure will be presented in chapter 5.1.

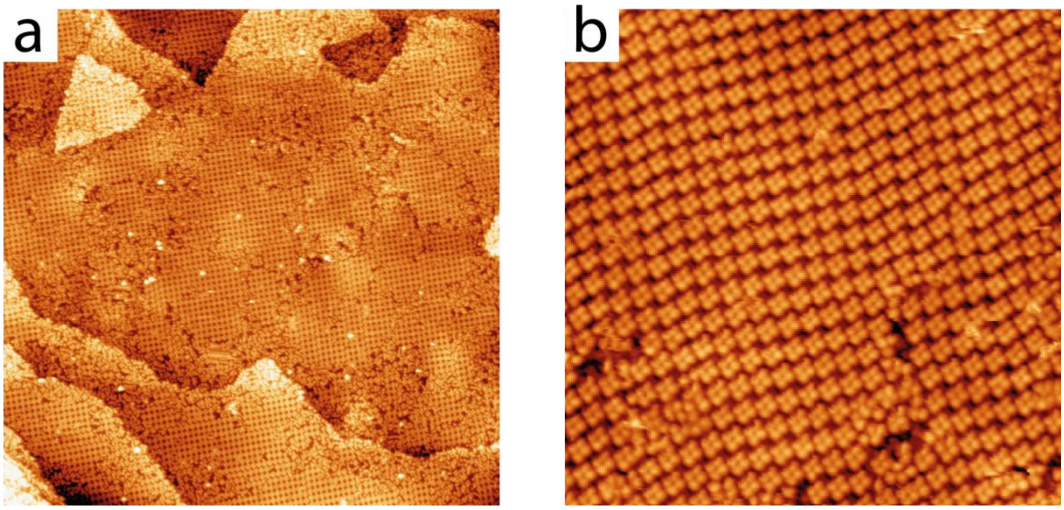

Fig. 4.1: STM images of *M*-[7H] showing a quadruplet structure on Cu(100). No mirror domains are observed. (Measurement parameters: **a**) 200 nm x 200 nm, +2.67 V, 42 pA; **b**) 50 nm x 50 nm, -1.19 V, 29 pA)

4.2 On Ag(100)

The self-assembly of *M*-[7]H on the Ag(100) surface showed basically the same structural motif as observed on Cu(100). Already at low coverage molecular quadruplets are formed, which assemble into an ordered structure only at saturated monolayer coverage (Fig. 4.2). In the saturated monolayer no enantiomorphous domains were found. In the alignment of the quadruplets shown in Fig. 4.2d the unit cell is quadratic and in matrix notation $\begin{pmatrix} 7 & 2 \\ -2 & 7 \end{pmatrix}$. The close-packed $[011]$ surface direction and a vector of the unit cell include an angle of $-14.5° \pm 2°$ and each molecule occupied a surface area of $1.10\ \mathrm{nm}^2$.

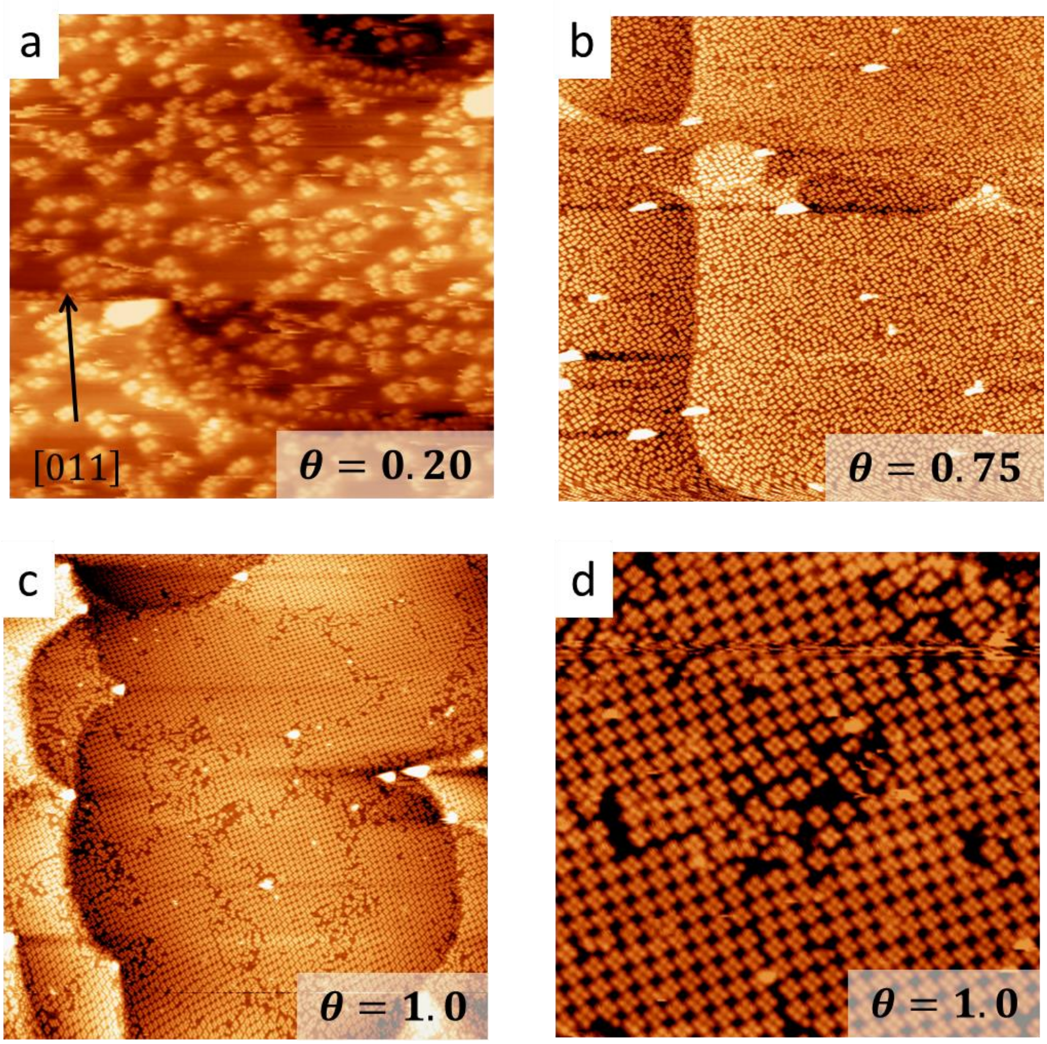

Fig. 4.2: STM images of *M*-[7]H on Ag(100) at different coverages. At low coverage isolated quadruplets are observed (**a**), which increase in number with higher coverage (**b**). Only in the saturated monolayer the quadruplets form an ordered structure (**c**) with identical quadruplet alignment as observed on Cu(100) (**d**). (Measurement parameters: **a**) 60 nm x 60 nm, -2.84 V, 15 pA; **b**) 200 nm x 200 nm, 2.73 V, 27 pA; **c**) 200 nm x 200 nm, 2.73 V, 26 pA; **d**) 50 nm x 50 nm, 2.73 V, 20 pA)

4.2.1 Discussion

Molecular models of the unit cell in Fig. 4.3 of the enantiopure structure show that, in contrast to Cu(100) (see chapter 5.1), on Ag(100) the molecules do not occupy identical adsorption sites. The observed $\begin{pmatrix} 7 & -2 \\ 2 & 7 \end{pmatrix}$ structure can only be built, if the molecules within the unit cell have the same relative alignment as in the unit cell on Cu(100), which leads to different adsorption sites for each molecule on the Ag(100) surface.

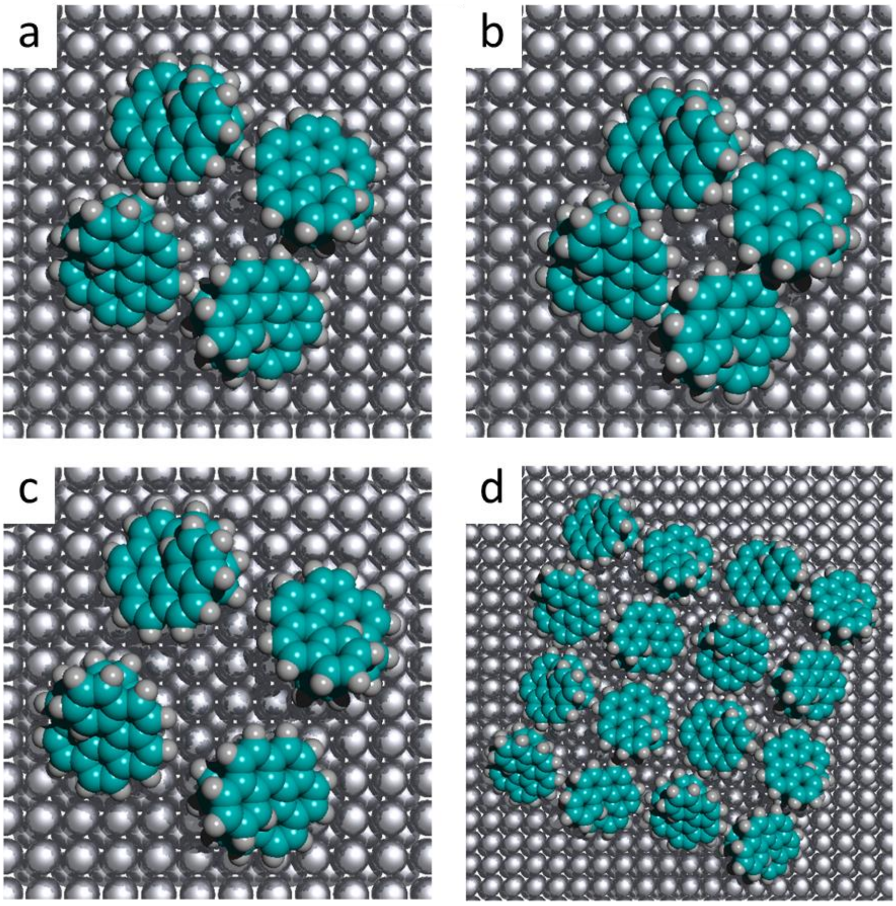

Fig. 4.3: Space-fill models of the *P*-[7]H unit cell on Ag(100). In **a** the molecules are aligned as in the unit cell on Cu(100) and as result do not have identical adsorption sites. In **b** and **c** the molecules are on identical adsorption sites, leading to a significant overlap in **b**. One step further away as in **c** and the molecules are too far apart for attractive interactions. **d**) Close-packing of four unit cells in the observed $\begin{pmatrix} 7 & -2 \\ 2 & 7 \end{pmatrix}$ is only possible with the same unit cell as on Cu (100) and different adsites for each molecule as shown in **a**.

4.3 On Ag(111) and Au(111)

The saturated monolayer ($\theta = 1.0$) of *M*-[7H] deposited on Ag(111) and Au(111) appeared in the STM as clusters of three molecules similar to the structure previously observed on Cu(111) (Fig. 2.8), as shown in Fig. 4.4a and b. At a coverage of $\theta = 0.90$, slightly below the saturated monolayer, the quadruplet structure shown in Fig. 4.4c is found on Au(111), denoted as δ phase in the following. With a coverage between $\theta = 0.90$ and $\theta = 1.0$ non-ordered clusters of three and four molecules coexist in the monolayer on Au(111) (see appendix Fig. 13.1).

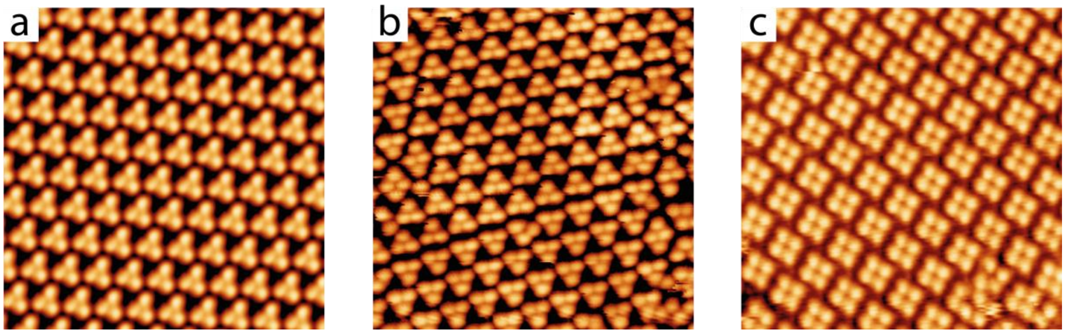

Fig. 4.4: STM image of *M*-[7H] on Ag(111) (**a**) and Au(111) (**b**) at θ = 1.0 showing clusters of three molecules. **c**) At a coverage of θ = 0.90 a quadruplet structure is observed on Au(111). (Measurement parameters: 20 nm x 20 nm, **a**) +2.90 V, 21 pA; **b**) -2.90 V, 43 pA; **c**) +2.73 V, 26 pA)

If a similar ordering than on Cu(111) is assumed, the actual packing of the molecules should be hexagonal and the clusters of three molecules are the result of different azimuthal orientations of the molecules (see chapter 2.1.3). The matrix notation of the superstructure lattice is $\begin{pmatrix} 6 & -1 \\ 1 & 7 \end{pmatrix}$ with a $10° \pm 2°$ tilt angle of the lattice vectors relative to the close-packed $[1\bar{1}0]$ surface direction. The tilt angle of the superstructure lattice is comparable to the 13.3° ± 2.7° on Cu(111), where the matrix notation is $\begin{pmatrix} 8 & 2 \\ -2 & 6 \end{pmatrix}$. In both cases the unit cell is a rhombus with a 120° angle. In the densest structure, the occupied space on the surface by a single molecule is 1.04 nm^2 on Ag(111), which is slightly larger compared to the 0.98 nm^2 on Cu(111).

The quadruplet clusters (Fig. 4.4c) align slightly tilted with respect to the $[1\bar{1}0]$ surface direction in rows, which gives a rhomboid unit cell with an angle of 130° between the unit cell vectors. The matrix notation of this superstructure lattice is $\begin{pmatrix} 6 & -2 \\ 1 & 10 \end{pmatrix}$ with a $5° \pm 2°$ tilt angle of the adlattice relative to the $[1\bar{1}0]$ surface direction. The packing density is with 1.10 nm^2 per molecule slightly lower compared to the *γ* structure density on Ag(111) and Au(111). The structural parameters of all observed enantiopure [7]H phases are summarized in Tab. 4.1. In Fig. 4.5 molecular models of the γ structure on Ag(111) and Cu(111) are shown.

Tab. 4.1: Summary of the adlattice parameters for the discussed structures formed *M*-[7H] on Cu(111), Ag(111) and Au(111). The adlattice tilt angle is given in respect to the $[\mathbf{1\bar{1}0}]$ surface direction. The given surface area was calculated from the matrix notation.

Surface	Matrix Notation	Adlattice Tilt Angle	Surface Area /nm² per Molecule
Cu(111)	γ: $\begin{pmatrix} 8 & -2 \\ -8 & -6 \end{pmatrix}$ β: $\begin{pmatrix} 14 & 12 \\ -12 & -14 \end{pmatrix}$	γ: +13.3° ± 2.7 ° β: -7.7° ± 0.6°	γ: 0.98 β: 1.08
Ag(111)	$\begin{pmatrix} 6 & -1 \\ 1 & 7 \end{pmatrix}$	+10° ± 2°	1.04
Au(111)	γ: $\begin{pmatrix} 6 & -1 \\ 1 & 7 \end{pmatrix}$ δ: $\begin{pmatrix} 6 & -2 \\ 1 & 10 \end{pmatrix}$	γ: +10° ± 2° δ: -5° ± 2°	γ: 1.04 δ: 1.10

4.3.1 Discussion

In the densest phases ($\theta = 1$), enantiopure [7]H align in a hexagonal fashion on Cu(111), Ag(111) and Au(111). This γ phase appears as clusters of three molecules in STM images, where the three molecules are rotated by 120° with respect to each other. The density in the γ phases is higher on Cu(111) with 0.98 nm^2 compared to the 1.04 nm^2 per molecule on Ag(111) and Au(111). A difference in the behavior appears at lower coverages, where on Au(111) the δ phase consisting of molecular quadruplets is formed, in contrast to the β phase on Cu(111) (marked blue in Fig. 2.8).

The hexagonal structure observed for enantiopure [7]H is the densest possible packing. Additionally, the (111) surfaces have the same symmetry, which may support the formation of hexagonal structures. At the temperatures studied here, ordered domains are only formed at high coverage and thus repulsive steric interactions can be considered as the main driving force for the formation of the ordered structures. At lower coverage, the mobility of the molecules at the measurement temperature of 60 K is too high and they cannot be imaged. The slight differences in the packing densities are the result of different lattice parameters, leading to a denser packing on Cu(111) under the premise of identical adsorption sites (Fig. 4.5). The models show that the adsorption grid provided by the substrate results in a better overlap on Cu(111) compared to Ag(111). Additionally, the [7]H molecule “fits” better to the Cu(111) surface, i. e. [7]H can adsorb with three benzene rings sitting on favored identical sites. This is not possible on Ag(111) and Au(111) due to larger atomic distances of 288.9 and 288.4 pm compared to the 255 pm of Cu(111). Thus, the three benzene rings of the terminal phenantrene group cannot occupy identical sites (see also Fig. 2.3). The formation of quadruplets may be the result of a lower adsorption energy on Au(111), an indication that the quadruplet is favored when lateral intermolecular interactions prevail.

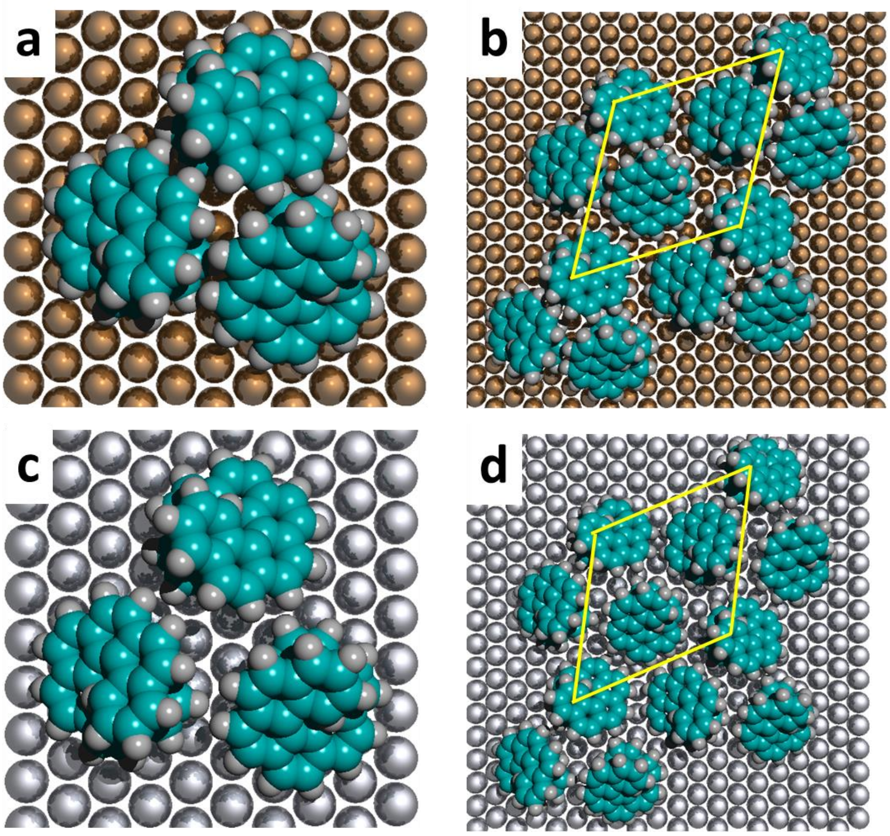

Fig. 4.5: Models of a single unit cell of *M*-[7]H on Cu(111) (**a**) and Ag(111) (**c**). Four unit cells arranged in a $\begin{pmatrix} \mathbf{6} & \mathbf{-2} \\ \mathbf{-8} & \mathbf{-6} \end{pmatrix}$ lattice on Cu(111) (**b**) and a $\begin{pmatrix} \mathbf{6} & \mathbf{-1} \\ \mathbf{1} & \mathbf{7} \end{pmatrix}$ lattice on Ag(111) (**d**). In all models the molecules are on identical adsorption sites, resulting in a slightly denser packing on Cu(111).

This quadruplet motive observed on Au(111) (Fig. 4.4c) also appeared on the Cu(100) and Ag(100) surfaces. The quadruplet formation of *M*-[7]H on Au(111) further shows that this quadruplet is likely an energetically favorable motif in the 2D self-assembly of enantiopure [7]H, which is even more favored on the (100) surfaces that have the same symmetry. With higher coverage the quadruplets are forced into the denser hexagonal packing.

5 Racemic Heptahelicenes

This chapter treats the self-assembly and two-dimensional crystallization of racemic [7]H (Fig. 2.4). The self-assembly at low coverage was investigated on Cu(111), Cu(100) and Ag(100) and the two-dimensional crystallization additionally on Ag(111) and Au(111).

Unless stated otherwise, the measurements were performed with an Omicron Variable Temperature STM (see chapter 3.1.1). *Rac*-[7]H was evaporated from a Knudsen cell held at 160 °C onto the respective crystal kept at RT. After deposition, the crystal was cooled with liquid helium and held at approximately 60 K during the measurements.

5.1 On Cu(100)

5.1.1 Sub-monolayer Coverage

Rac-[7]H aggregates into quadruplet clusters the Cu(100) surface already at a coverage below 10% of the saturated monolayer coverage, as shown in Fig. 5.1a.

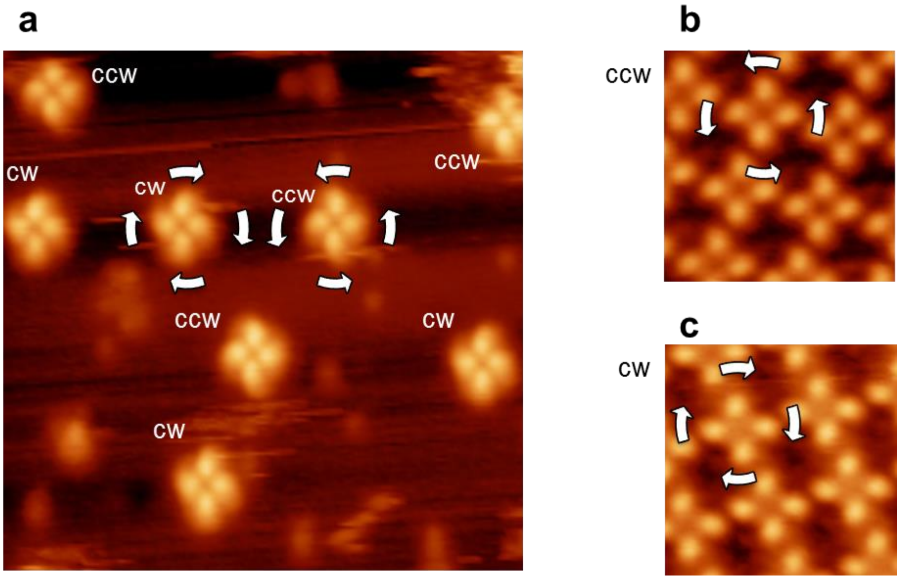

Fig. 5.1: **a**) STM image of *rac*-[7]H at θ = 0.15. Four molecules aggregate to one cluster. Each cluster can be seen as a propeller with four blades, whereby two rotational senses appear. The image shows eight clusters in total, four rotating clockwise (cw) and four counterclockwise (ccw). This counterclockwise (**b**) or clockwise (**c**) appearance can also be assigned to the quadruplets in the monolayer. (Measurement parameters: 20 nm x 20 nm, -3.08 V, 10 pA)

The clusters exhibit two different appearances by “turning” clockwise (cw) or counterclockwise (ccw), respectively. The relative orientations of the clusters with respect to the surface lattice are similar for both cw and ccw and thus the molecules may occupy the same adsorption sides. Also, each molecule within a cluster has the same appearance and each adjacent molecule within a cluster is rotated by 90°. Comparing the isolated quadruplets with the ones in the monolayer (Fig. 5.1b and c) allows the assignment of *M*-[7]H to the cw and *P*-[7]H to the ccw quadruplets, respectively. It is also evident that the relative adsorption orientation between the molecules within the clusters and the substrate is identical at low coverage and in the saturated monolayer, despite the additional intermolecular forces in the monolayer.

5.1.2 The Saturated Monolayer

The two-dimensional crystallization of *rac*-[7]H on the Cu(100) surface leads to mirror domains with molecular quadruplets as building blocks that were already observed for *M*-[7]H on Cu(100) (Fig. 5.2). Similar to the zigzag rows on Cu(111), the mirror domains have an oblique tilt angle with respect to the substrate lattice, i. e. a unit cell vector and the close-packed $[011]$ surface direction include an angle of $+14.5° \pm 2°$ or $-14.5° \pm 2°$, respectively. Hence, the $[011]$ surface direction can be considered as mirror for the enantiomorphous domains. The unit cell of the enantiomorphous adsorbate lattices is quadratic and defined in matrix notation as $\begin{pmatrix} 8 & 2 \\ -2 & 8 \end{pmatrix}$ (green in Fig. 5.2a and b) or $\begin{pmatrix} 8 & -2 \\ 2 & 8 \end{pmatrix}$ (blue in Fig. 5.2a and b), respectively. The surface area occupied per molecule in this structure is 1.10 nm^2, which is a less denser packing compared to the previously described structures on the (111) surfaces, with the exception of the quadruplet δ phase on Au(111) having the same density.

The four molecules in a unit are identical at first glance and the quadruplets appear as four-bladed propellers at higher magnification (insets in Fig. 5.2a). With different tunneling condition and depending on the tip state, the molecules appear as three-lobe pattern, which allows the assignment of the absolute handedness as depicted in Fig. 5.2c and d. Going from bright to weaker lobes (yellow-red-blue) shows that the $\begin{pmatrix} 8 & 2 \\ -2 & 8 \end{pmatrix}$ structure consists only of *M*-[7]H and the $\begin{pmatrix} 8 & -2 \\ 2 & 8 \end{pmatrix}$ structure only of *P*-[7]H. Matching a molecular model of the quadruplet with the corresponding image shows that the molecules are rotated by 90° with respect to each other.

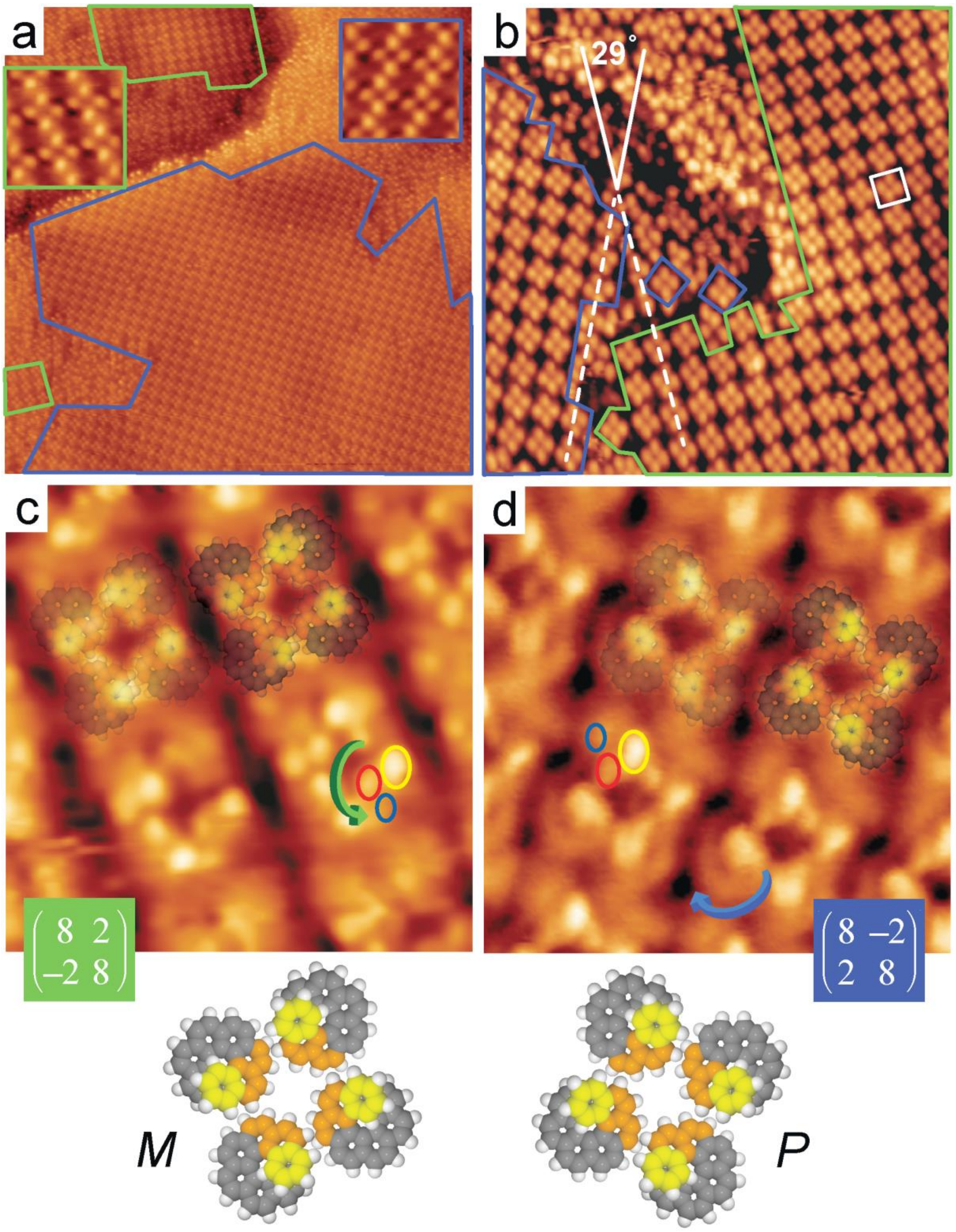

Fig. 5.2: **a**) Enantiomorphous domains (marked green and blue) observed after the deposition of *rac*-[7H] on Cu(100), consisting of molecular quadruplets (insets). **b**) STM image showing a mirror domain boundary and the 29° angle between both domains. **c**, **d**) STM images with submolecular resolution superpositioned with molecular models, suggesting homochiral domains. In the model the distal rings are colored yellow and orange, which matches the appearance in the images. The opposite helicity of the molecules is indicated by arrows pointing to the proximal ends. (Measurement parameters: **a**) 80 nm x 80 nm (insets: 6 nm x 6 nm), -2.78 V, 42 pA; **b**) 35 nm x 35 nm, -2.73 V, 40 pA; **c**) 6 nm x 6 nm, -1.19 V, 179 pA; **d**) 6 nm x 6 nm, -0.773 V, 198 pA)

Simulations of the STM appearance for different quadruplet alignments of [7]H in a $\begin{pmatrix} 8 & -2 \\ 2 & 8 \end{pmatrix}$ unit cell support the assignment of a homochiral *P*-[7]H domain. The LUMO state density was calculated for the entire unit cell and compared to experimental STM images obtained while tunneling from the tip into unoccupied states of the surface. In Fig. 5.3 the results for four *P*-[7]H (c), two *M/P*-[7]H pairs (e) and four *M*-[7]H (f) molecules in a $\begin{pmatrix} 8 & -2 \\ 2 & 8 \end{pmatrix}$ unit cell are shown. The superposition of the calculation for *P*-[7]H and the corresponding molecular model (a, b) shows that the chosen height of 3 Å above the surface reflects predominantly the upper part of the molecule. The distal C_6 ring appears as intense lobe with minor intensity located at the second highest C_6 ring. Only the LUMO density of state calculated for the *P*-[7]H quadruplet matches the STM appearance for this polarity (d). In particular the positions of the brightest lobes distinguish the *P*-[7]H appearance from the other two possibilities.

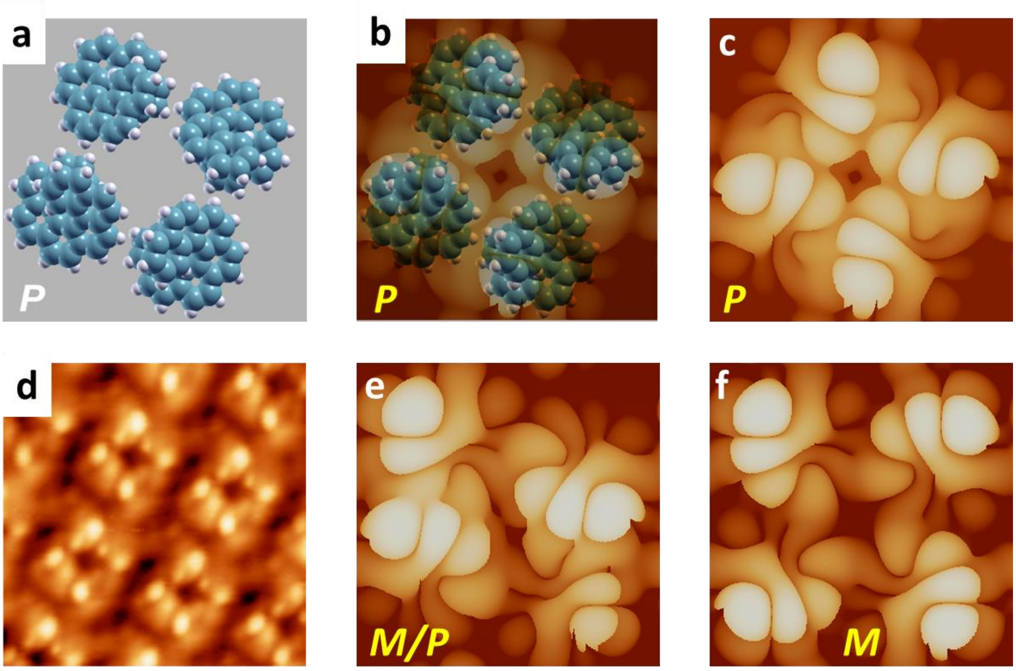

Fig. 5.3: Simulation of the STM appearance of three different quadruplet alignments in a $\begin{pmatrix} \mathbf{8} & -\mathbf{2} \\ \mathbf{2} & \mathbf{8} \end{pmatrix}$ unit cell. **a**) Structural setup for the *P*-[7]H calculations. **b**) Superposition of the setup model with the result for the LUMO electron density 3 Å above the surface shown in **c**. Calculations of the LUMO density of state 3 Å above the surface for two *M/P*-[7]H pairs (**e**) and a *M*-[7]H quadruplet (**f**) have different appearances. Only the modeled appearance for a *P*-[7]H quadruplet matches the experimental appearance shown in **d**. (Measurement parameters: **d**) 6 nm x 6nm, 1.21 V, 198 pA)

Molecular models for the $\begin{pmatrix} 8 & -2 \\ 2 & 8 \end{pmatrix}$ unit cell further support the *P*-[7]H assignment. If the proximal ring of each molecule is placed on identical adsorption sites and C_4 symmetry for the homochiral or C_2 for the heterochiral unit cell, respectively, is assumed, only *P*-[7]H fits in the $\begin{pmatrix} 8 & -2 \\ 2 & 8 \end{pmatrix}$ unit cell (Fig. 5.4 and Fig. 5.5).

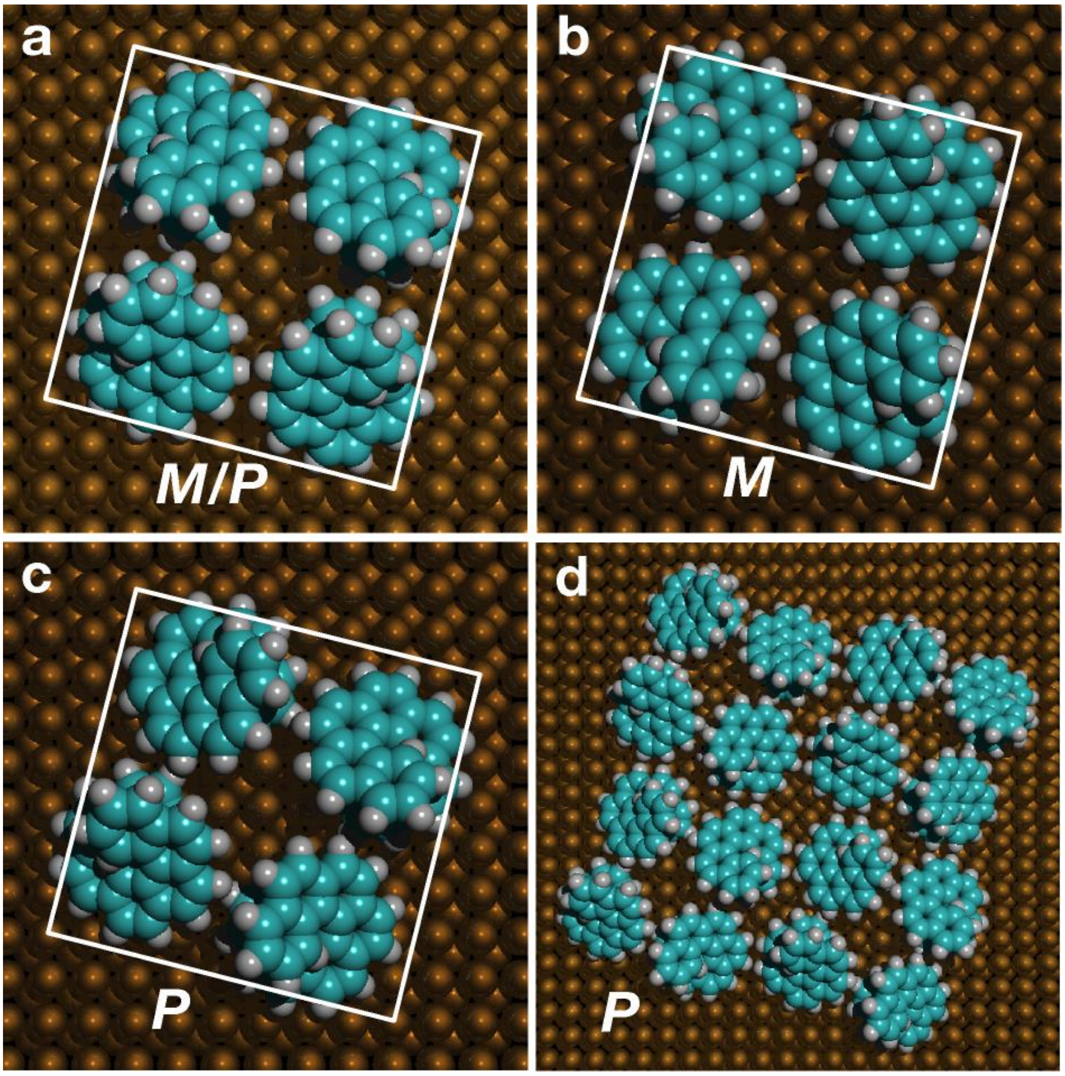

Fig. 5.4: Models for a $\begin{pmatrix} \mathbf{8} & \mathbf{-2} \\ \mathbf{2} & \mathbf{8} \end{pmatrix}$ unit cell containing two pairs of *M/P*-[7]H (**a**), a quadruplet of *M*-[7]H (**b**) and a quadruplet of *P*-[7]H (**c**). Only in the case of *P*-[7]H the molecules occupy identical adsorption sites in the unit cell and are related by $\boldsymbol{C_4}$ symmetry. **d**) Four unit cells of *P*-[7]H showing that this model allows close-packing.

With arbitrary adsorption sites four *M/P*-[7]H or *M*-[7]H can fit in the $\begin{pmatrix} 8 & -2 \\ 2 & 8 \end{pmatrix}$ unit cell, but an extended monolayer cannot be built up with these formations, as illustrated in Fig. 5.5. An overlap of molecules in adjacent unit cells imposes a rather strong repulsion. Building an extended domain is only possible for the quadruplet of *P*-[7]H (Fig. 5.4c, d). In that case the overlap is avoided, because the helicity allows parts of the molecules to slide over/under each other. Thus the model in Fig. 5.4d depicts the densest possible packing.

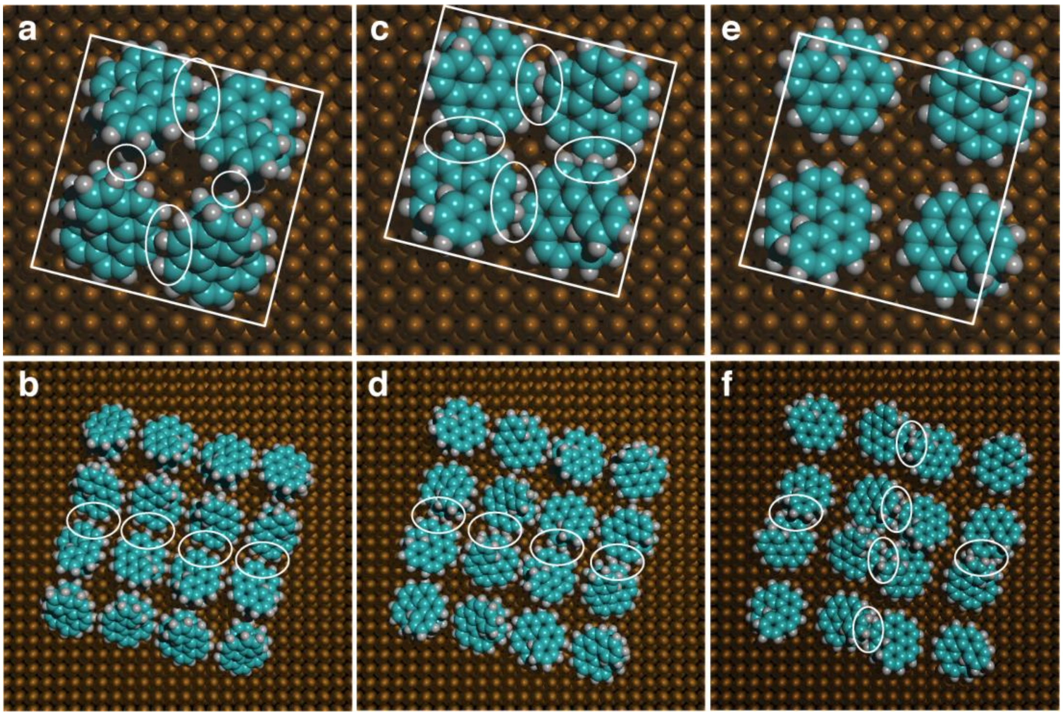

Fig. 5.5: Different packing models for *M/P*-[7]H pairs (**a**, **b**) and *M*-[7]H (**c**-**f**) in a $\begin{pmatrix} 8 & -2 \\ 2 & 8 \end{pmatrix}$ unit cell. Identical adsites for the *M/P*-[7]H pairs do not allow close-packing in the unit cell (**a**) or extended monolayer (**b**). Ignoring the substrate also does not allow close-packing for *M*-[7]H (**c**, **d**). In a less dense packing with identical adsites four *M*-[7]H molecules do not fit in the unit cell (**e**) and thus do not allow an extended monolayer (**f**). The conflicts due to the close-packing are indicated by white ellipsis.

5.1.3 Discussion

The Cu(100) surface is the only surface so far, where *rac*-[7]H resolved into the enantiomers and crystallized as a conglomerate in the saturated monolayer. The molecular ordering shown in Fig. 5.4d for an extended model of the *P*-[7]H domain allows the molecules in a unit cell to partially slide over/under each other due to the helicity. This sliding results in stronger attractive van-der-Waals interactions in a quadruplet and they are already formed at low coverage. Thus, attractive van-der-Waals forces should be responsible for the quadruplet formation. Mainly repulsion drives the ordering of the quadruplets, since the quadruplets only start to form an ordered structure at the monolayer saturation coverage. At a relative coverage of about 80% of the saturated monolayer (see appendix Fig. 13.2 and Fig. 13.3), most molecules form non-ordered quadruplets. In the saturated monolayer, repulsive forces are more pronounced due to an increased influence of steric interactions, resulting in an ordering of the quadruplets. The actual alignment is then the result of maximizing intermolecular attraction in the quadruplet and minimizing the repulsion among quadruplets in the complete layer. The same structure of isolated quadruplets at low coverage and in the close-packed monolayer further indicates that the quadruplet is a stable 2D packing motif for enantiopure [7]H. Compared thereto, the relative molecular alignment in the racemic zigzag rows and in the hexagonal packings of enantiopure [7]H changes with increasing packing density (see chapter 2.1.3).

5.2 On Ag(100)

The self-assembly of *rac*-[7]H on Ag(100) differs from the previously described behavior of *rac*-[7]H, i. e. the observed structures change with increasing coverage. A series of STM images with increasing coverages is shown in Fig. 5.6. At very low coverage quadruplets, like on Cu(100), are observed (a) and with increasing coverage zigzag rows like on the (111) surfaces start to form (b). The relative number of zigzag rows compared to the number of quadruplets as well as their length increase with higher coverage (c and d). At a coverage of about 80% of the saturated monolayer the zigzag rows start to order and only very few quadruplets are left (e), which disappear completely at saturation coverage (f). In the ordered monolayer structure no mirror domains are observed.

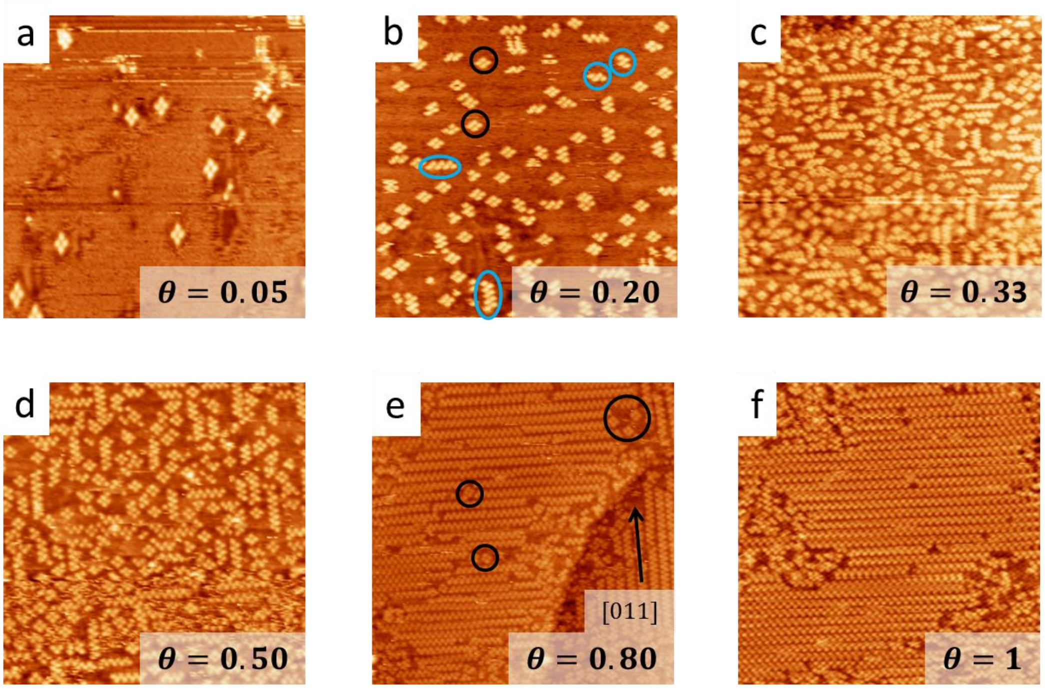

Fig. 5.6: Series of STM images showing *rac*-[7]H on Ag(100) with increasing coverage. At the coverage of $\boldsymbol{\theta = 0.05}$ only quadruplets are observed on the surface (**a**). With increasing coverage zigzag rows start to form (marked blue in **b**) and coexist with the quadruplets (marked black in **b**). Further increasing the coverage leads to more and longer zigzag rows and fewer portion of quadruplets (**c** and **d**). At $\boldsymbol{\theta = 0.80}$ the zigzag rows are ordered and only very few quadruplets are left (marked red in **e**). In the saturated monolayer no quadruplets are left, even in non-ordered areas (**f**). The zigzag rows run along the close-packed $[\mathbf{011}]$ direction and no enantiomorphous domains are observed. (Measurement parameters: **a**) 50 nm x 50 nm, -2.84 V, 31 pA; **b**) 45 nm x 45 nm, 2.84 V, 19 pA; **c**) 70 nm x 70 nm, 2.73 V, 27 pA; **d**) 50 nm x 50 nm, 2.73 V, 27 pA; **e**) 60 nm x 60 nm, -2.73 V, 23 pA; **f**) 50 nm x 50 nm, -2.73 V, 23 pA)

5.2.1 Discussion

There are only a few examples in literature for coverage driven chiral phase transitions in 2D, all comprising prochiral molecules. For 1-Nitronaphtalene (NN) on Au(111) a phase transition from a conglomerate to a racemate was observed. At low coverage homochiral chains were formed and an achiral racemic structure in the monolayer. As a driving force favorable electrostatic interactions for the racemic structure in a close-packed layer were identified[75]. In the case of 4-[*trans*-2-(pyrid-4-yl-vinyl)] benzoic acid (PVBA) on Cu(100), enantiopure domains exhibiting organizational chirality were formed at low coverage. At a critical coverage, the structure abruptly changed and the molecules assembled in a racemic phase. Packing requirements in the denser phase were identified as driving force suppressing the chiral resolution[76]. A change from a racemic mixture to homochiral domains was observed in the adsorption of Ni-tetramethyl-tetraazaannulene (TMTAA) on Au(111). Trimers exhibiting organizational chirality are formed at low coverage and randomly distributed on the surface. With increasing coverage these trimers ordered in homochiral domains due to steric interactions[77].

Compared to the previously mentioned studies, there are no polar interactions here. Packing effects and steric interactions can be excluded as driving forces for the change from conglomerate to racemate formation, since isolated zigzag rows are already observed at low coverage. The coexistence of quadruplets and zigzag rows show that the difference in energy should be minimal between both structures. At low coverage, the minimum nucleation size of double rows consists of four molecules (blue circles in Fig. 5.6b) and no molecular dimers were observed.

In order to form a quadruplet, four molecules of the same handedness have to find each other, for zigzag row nucleation also four molecules – two of each handedness – are required. Statistically, the chance for the collision of four molecules of the same handedness is 12.5% and for two of each handedness 37.5%, respectively. This should support the formation of zigzag rows. Hence the formation of quadruplets shows that they are energetically slightly favored. Additionally, the nucleation of quadruplets and zigzag rows may start at slightly different temperatures and it can be assumed that the crystallization temperature of the quadruplets is slightly higher than the one for the zigzag rows. Now, with a higher effective mean free path at low coverage the homochiral quadruplets can form upon cooling. A higher coverage and reduced effective mean free path of the molecules the probability for quadruplet formation becomes lower. Due to further cooling the nucleation temperature for the zigzag rows is reached and the heterochiral rows are formed instead of the homochiral quadruplets. This scenario is supported by tempering experiments. Keeping a sample at the roughly estimated nucleation temperature of 200 K resulted in a disordered monolayer. Before tempering, the same sample showed formation of the zigzag rows (Fig. 13.4). This is explained by an enantiomeric unbalanced layer, which is the result of a partial separation of the enantiomers during tempering.

Another explanation is based on a higher number of molecules needed for the nucleation of zigzag rows, so that higher coverage is required for nucleation cluster formation. However, the observation of four-molecule clusters for zigzag rows and the statistical higher formation probability for heterochiral nucleation clusters contradict this scenario.

5.3 On Ag(111) and Au(111)

Rac-[7]H deposited on Ag(111) and Au(111) starts to form ordered structures only at coverages close to a full monolayer. At a first glance, the formed structures are very similar to the zigzag rows described in chapter 2.1.3 for *rac*-[7]H on Cu(111). STM images of the observed structures are shown in Fig. 5.7.

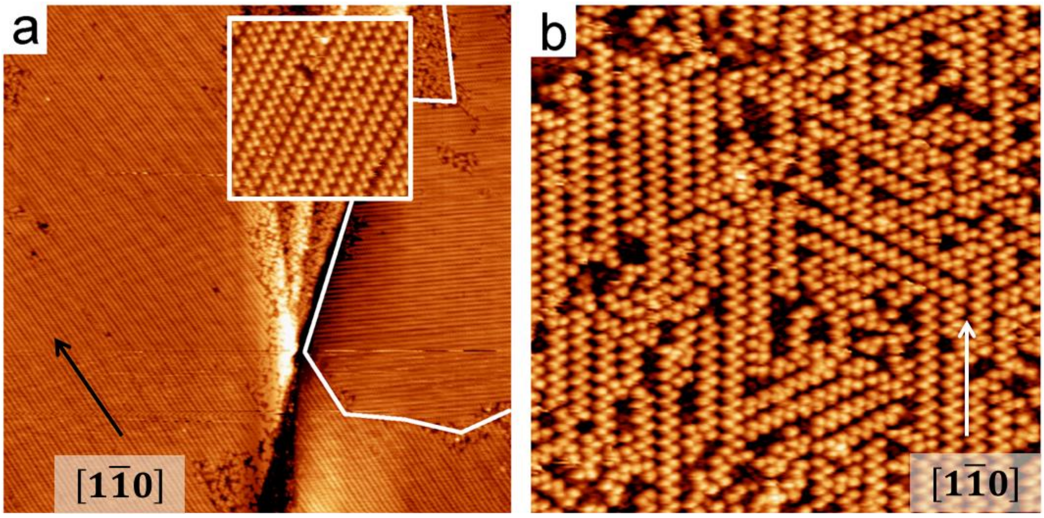

Fig. 5.7: **a**) Large area STM image of *rac*-[7H] on Ag(111) showing the zigzag row structure (inset: 20 nm x 20 nm, 1.23 V, 59 pA). A rotational domain boundary is marked by the white line. **b**) STM image of *rac*-[7]H on Au(111) also showing the zigzag row motif. (Measurement parameters: **a**) 200 nm x 200 nm, +2.781 V, 19 pA; **b**) 40 nm x 40 nm, +2.781 V, 11 pA)

In contrast to the enantiomorphous zigzag rows on Cu(111), no mirror domains were found on Ag(111). The double rows have tilt angles of 120° with respect to each other and run along the close-packed $[1\bar{1}0]$ surface direction. This is in contrast to the opposite tilt angles of the enantiomorphous domains on Cu(111).

The unit cell of the closer packed rows is rhomboid with an angle of 110° and a matrix notation of $\begin{pmatrix} 4 & 0 \\ 1 & 7 \end{pmatrix}$, which gives the same density as the λ/ρ structures on Cu(111) with 1.04 nm^2 per molecule. On Au(111) also zigzag rows running along the $[1\bar{1}0]$ direction without enantiomorphism were observed, but not in long-range ordered domains (Fig. 5.7b). The structural parameters of the structures on the (111) surfaces are summarized in Tab. 5.1.

Tab. 5.1: Summary of the parameters of the closest-packed double row structures formed by *rac*-[7H] on (111) surfaces. The adlattice tilt angle is given in respect to the $[1\bar{1}0]$ surface direction. The given surface area was calculated from the matrix notation.

Surface	Matrix Notation	Adlattice Tilt Angle	Surface Area /nm² per Molecule
Cu(111)	λ: $\begin{pmatrix} 4 & 1 \\ -5 & 8 \end{pmatrix}$ ρ: $\begin{pmatrix} 4 & -1 \\ 5 & 8 \end{pmatrix}$	λ: -10.5° ± 0.8° ρ: +10.5° ± 0.8°	1.04
Ag(111)	λ: $\begin{pmatrix} 4 & 0 \\ 1 & 7 \end{pmatrix}$	λ: 0° ± 2°	1.04
Au(111)	---	0° ± 2°	---

To get a better understanding of the alignment of the molecules in the double rows and for the lack of enantiomorphous domains on Ag(111), high resolution STM images of the zigzag rows on Cu(111) and Ag(111) are shown in Fig. 5.8. In the STM image of the zigzag row structure of *rac*-[7]H on Cu(111) shown in Fig. 5.8a each molecule has a three-lobe appearance. Going from the brightest to weakest lobe (yellow-red-blue) reveals the absolute helicity of the molecule and shows that the rows consist of heterochiral pairs (see also chapter 2.1.3).

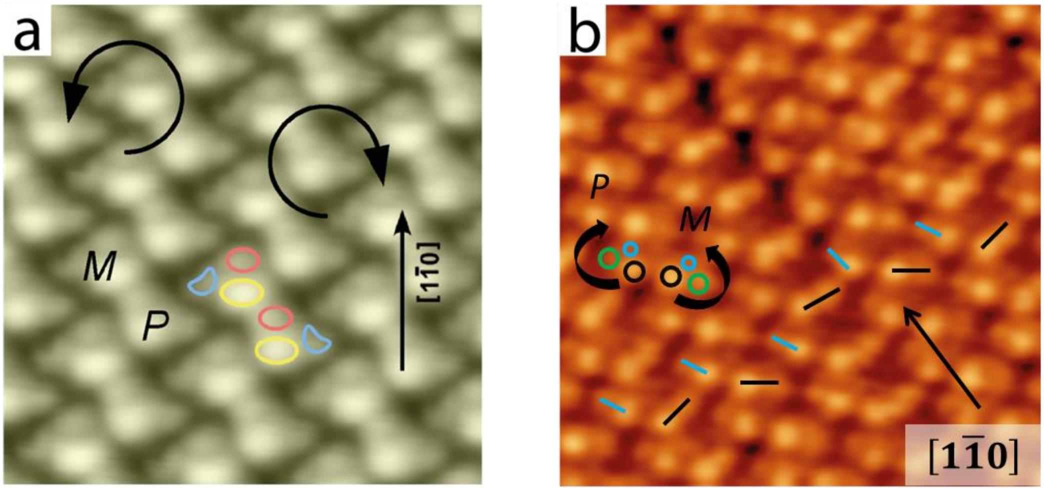

Fig. 5.8: **a**) STM image of *rac*-[7]H on Cu(111) (courtesy of M. Parschau). The zigzag rows have an oblique tilt angle with respect to the $[1\bar{1}0]$ surface direction and consist of heterochiral pairs. **b**) STM image of the zigzag rows on Ag(111). The rows run along the $[1\bar{1}0]$ direction and also consist of heterochiral pairs as indicated by going from bright to dark within a molecule (black-green-blue). Along each row the molecules all have the same relative orientation, but in contrast to Cu(111) there are different orientations of the molecules in adjacent rows as indicated by the black and blue lines. (Measurement parameters: **a**) 6 nm x 6 nm, 2.40 V, 126 pA; **b**) 10 nm x 10 nm, -2.84 V, 10 pA)

The heterochiral composition of the zigzag rows on Ag(111) can be deduced by going from bright to dark lobes within one molecule (indicated black-green-blue in Fig. 5.8b). Despite both structures appearing as zigzag rows, there are significant differences between the molecular alignments on Ag(111) compared to Cu(111), that is, there are different relative orientations of the molecules in adjacent rows on Ag(111) as indicated by the black and blue lines in Fig. 5.8b. Only the molecules along one row in the direction of the $[1\bar{1}0]$ surface direction, as indicated in Fig. 5.8b by the black arrow, have the same relative orientation. In contrast, the molecules in adjacent rows on Cu(111) all have identical orientations.

5.3.1 Discussion

On all investigated (111) surfaces, *rac*-[7H] aligns in double rows consisting of the *M*-[7]H and *P*-[7]H enantiomers in an equal ratio. In general, there are two major structural differences between the zigzag rows on Cu(111), Ag(111) and Au(111): (I) the lack of enantiomorphous domains and (II) differences in the relative molecular orientations in adjacent zigzag rows within one domain. The distance between these rows and thus the packing density depends on the coverage and was intensively studied on Cu(111)[47], where enantiomorphous domains are formed. Here, the coverage dependence was not further investigated. On Ag(111) the inter-row distances are very similar to the domains with λ'/ρ' and λ/ρ structures on Cu(111). However, the double row structure on Ag(111) does not show any enantiomorphous features, and the zigzag rows run along the close-packed $[1\bar{1}0]$ surface direction, whereas on Cu(111) the tilt angle of the rows is $-10.5° \pm 0.8°$ for the λ and $+10.5° \pm 0.8°$ for the ρ structure. Unfortunately, on Au(111) no well-ordered domains were found, but zigzag rows running along the $[1\bar{1}0]$ surface direction are observed. The poor ordering on Au(111) may be ascribed to the herringbone reconstruction and its alternating hcp-fcc sites[78]. High resolution STM images (Fig. 5.8) reveal that the molecules in the zigzag rows have all identical orientation on Cu(111) within one domain, whereas on Ag(111) the molecular orientation is only identical along a zigzag row. As indicated by the black and blue lines in Fig. 5.8b, the molecules are differently aligned in adjacent rows, but along each row (arrow in Fig. 5.8b) the orientations of the molecules are identical. Due to these differences in the orientations of molecules in adjacent parallel zigzag rows and different distances between zigzag rows (inset in Fig. 5.7a), determining the matrix notation and building a molecular model for the monolayer as on Cu(111) is not unambiguously possible for the rows on Ag(111). In contrast to Cu(111), identical adsorption sites lead to significant overlap in the unit cell on Ag(111) (Fig. 5.9c). Thus, the molecules in the possible arrangements in zigzag rows shown in Fig. 5.9 are on random adsorption sites and have probably a different relative alignment compared to Cu(111).

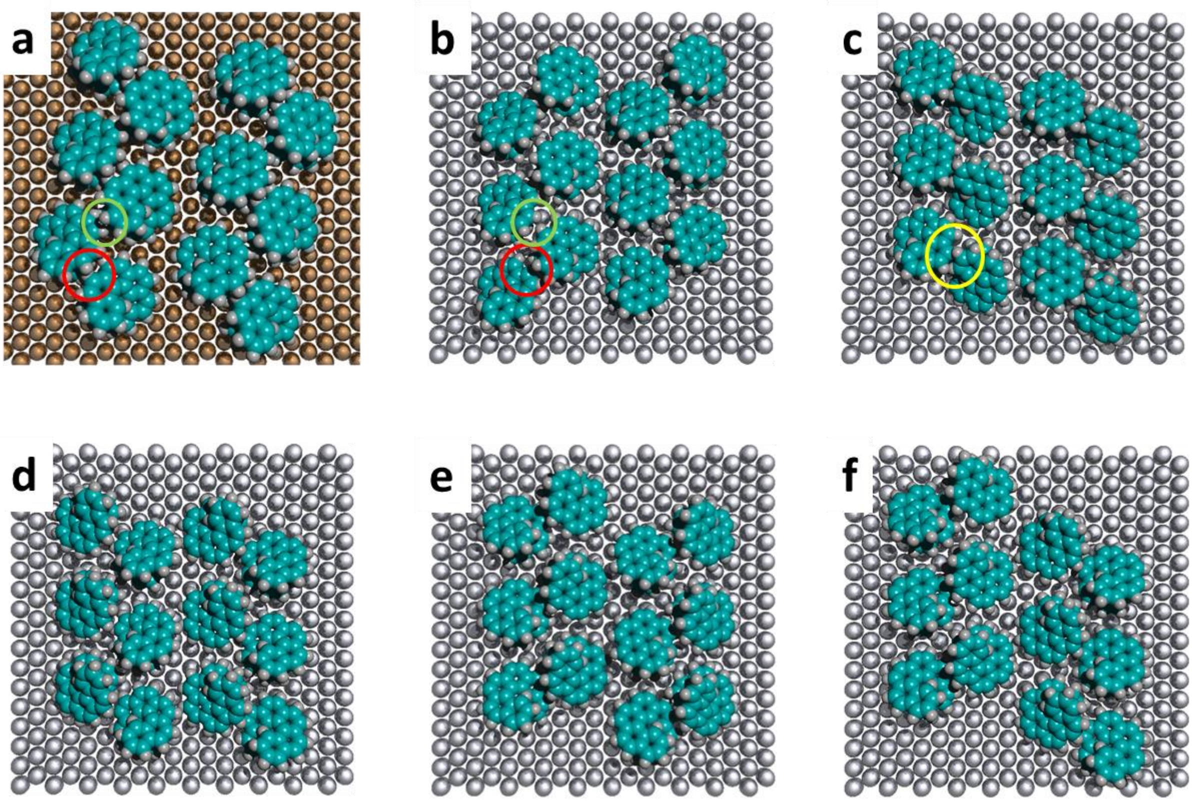

Fig. 5.9: Molecular models for zigzag rows. On Cu(111) the rows have an oblique tilt angle with respect to the close-packed $[\mathbf{1\bar{1}0}]$ surface direction and the molecules are on identical adsorption sites (**a**). Dimers with the same relative alignment as on Cu(111) arranged along the $[\mathbf{1\bar{1}0}]$ surface direction result in a $\begin{pmatrix}\mathbf{4} & \mathbf{0}\\ \mathbf{3} & \mathbf{7}\end{pmatrix}$ matrix on Ag(111) (**b**). Identical adsorption sites on Ag(111) lead to a significant overlap (yellow circle in **c**). Possible alignments of the molecules for two enantiomorphous rows with the experimentally determined $\begin{pmatrix}\mathbf{4} & \mathbf{0}\\ \mathbf{1} & \mathbf{7}\end{pmatrix}$ structure are shown in **d** and **e**. Due to the alignment along the closed–packed surface direction, rows from both mirror domains in **d** and **e** can be incorporated into a single domain with a $\begin{pmatrix}\mathbf{4} & \mathbf{0}\\ \mathbf{1} & \mathbf{7}\end{pmatrix}$ unit cell (**f**).

The identical orientation of molecules along each zigzag row on Cu(111) and Ag(111) (Fig. 5.8) may be the result of attractive van-der-Waals interactions of the molecules along a row due to the molecules sliding over/under each other as indicated by red and green circles in Fig. 5.9.

In the rows *M-P* pairs form chiral entities that exist in mirror forms and align in the observed zigzag rows, whereby identical *M-P* pairs form one row. On Cu(111) the rows consisting of enantiomorphous *M-P* pairs have opposite oblique tilt angles with respect to the $[1\bar{1}0]$ surface direction (Fig. 5.9a) and thus form mirror domains (see also chapter 2.1.3). In contrast thereto, the rows on Au(111), Ag(111) and Ag(100) run along the close-packed $[1\bar{1}0]$ surface direction as shown for Ag(111) in Fig. 5.9.

M-*P* pairs with opposite handedness can form rows that are mirror images of each other (Fig. 5.9d and e). However, with all rows running along the $[1\bar{1}0]$ surface direction, rows that are mirror images of each other can be incorporated into a single domain (Fig. 5.9f), which leads to the lack of mirror domains in the zigzag row structures of *rac*-[7]H on Au(111), Ag(111) and Ag(100).

5.4 Dimer Formation of Racemic Heptahelicenes on Cu(111)

After evaporating small amounts of *rac*-[7]H on the Cu(111) crystal held at 373 K, at a temperature of 6 K almost exclusively molecular dimers were observed (Fig. 5.10). These dimers appeared asymmetric and with two mirror forms, both shown in Fig. 5.10b. The absolute chirality of single molecules could be determined by high resolution images by going from bright to dark contrast, as indicated by increasing numbers in Fig. 5.10c (Experiments performed by K.-H. Ernst at IBM Almaden Research Center).

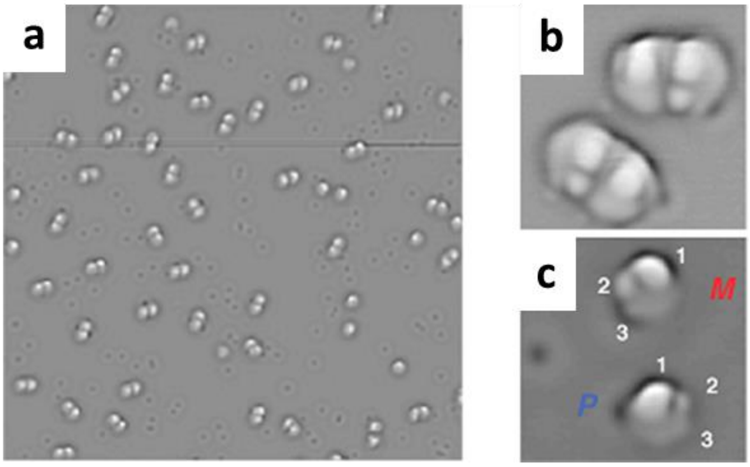

Fig. 5.10: **a**) STM image of *rac*-[7]H on Cu(111) showing the formation of molecular dimers, which appear in two enantiomorphous forms (**b**). **c**) Two single enantiomers, where the absolute handedness can be assigned due to the descent of the helix (indicated by increasing numbers). The dark spots are CO molecules**.** (Measurement parameters: **a**) 50 nm x 50 nm, 0.5 V, 20 pA; **b**) 5 nm x 5 nm, 1.6 V, 10 pA; **c**) 5 nm x 5 nm, 0.5 V, 20 pA)

In order to determine whether the molecular dimers are homochiral or heterochiral, molecular models were prepared under the premise of identical adsorption sites and their relative energies estimated by AMBER force field geometry optimization calculations with HyperChem 7.1™. The calculated energies in Fig. 5.11 are given relative to the lowest energy dimer. Due to the premise of identical adsorption sites, two alignments for homochiral dimers have *a priori* a too strong overlap between both molecules (Fig. 5.11e, f). The homochiral dimer without strong overlap has an energy 8.7 kcal/mol higher than the lowest heterochiral dimer. For heterochiral dimers, three possible alignments with identical adsorption sites were found. Two alignments have very similar energies (Fig. 5.11b, c) and one possibility has a significant higher energy close to the homochiral dimer energy (Fig. 5.11a).

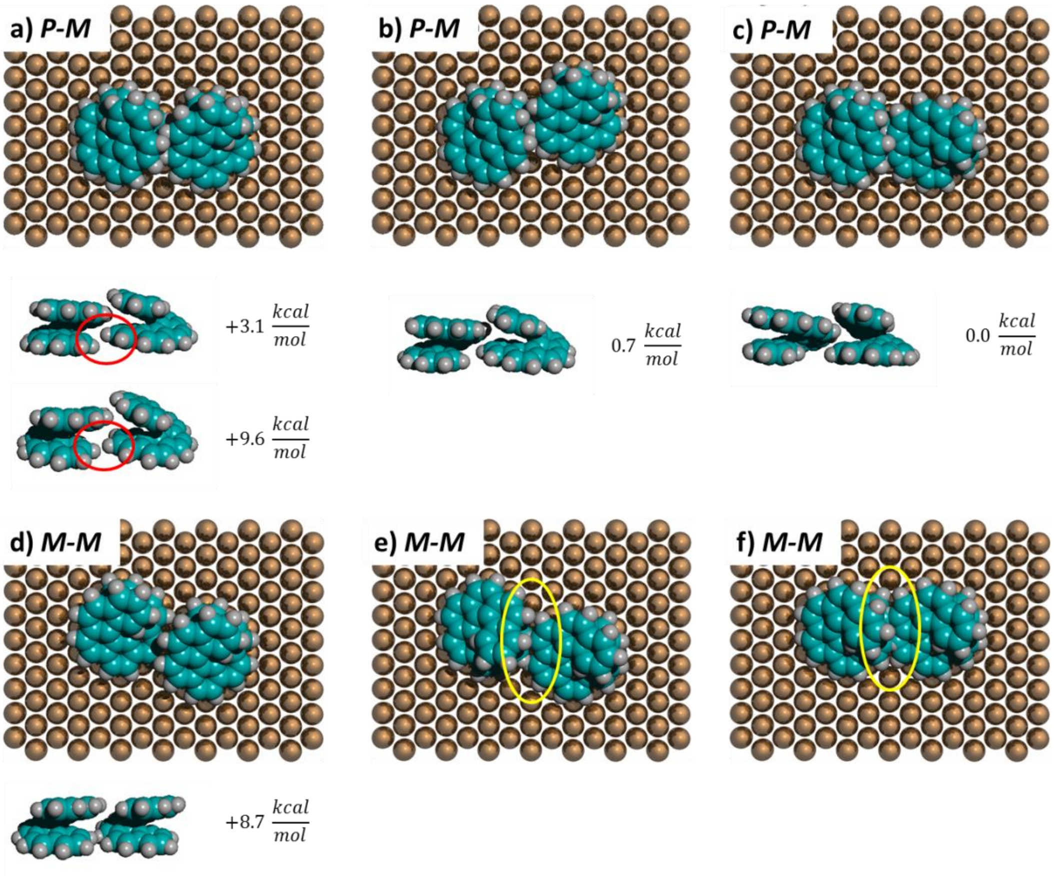

Fig. 5.11: Space-filling models for heterochiral (**a**-**c**) and homochiral (**d**-**f**) dimers with identical adsorption sites. The energies are given relative to the lowest energy heterochiral dimer in **c**. The energy of the heterochiral dimer in **a** was calculated with fixed (lower dimer) and relaxing (upper dimer) terminal hydrogen atoms (red ellipse), which lead to a considerable difference in energy. The homochiral dimers in **e** and **f** have *a priori* a strong overlap (yellow ellipse) and the homochiral dimer without overlap (**d**) a significantly higher energy than the heterochiral dimers.

To evaluate if the heterochiral dimer with the lowest calculated energy is identical to the experimentally observed one, its appearance in the STM was calculated (by Laura Zoppi at the University of Zürich) and compared to the obtained STM images, as illustrated in Fig. 5.12. And indeed, the experimental STM appearance was thereby best modeled by the heterochiral dimer with the lowest calculated energy shown in Fig. 5.12c. However, the difference in energy between the two lowest energy heterodimers is very small, because molecule-surface interactions are not included in the calculations and the substrate positions were fixed manually.

The heterochiral composition of the dimers was also confirmed by STM manipulation experiments. By taking several dimers apart with a modified STM tip the absolute handedness of the single molecules was determined (see appendix **Error! Reference source not found.** and Fig. 5.12c)[79].

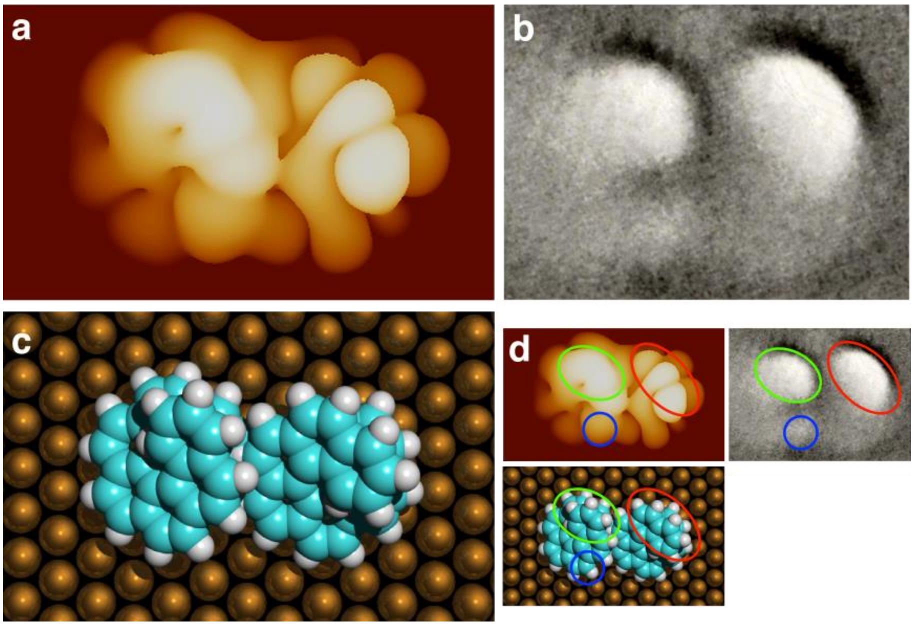

Fig. 5.12: **a**) Calculation for the STM appearance in constant current imaging at a bias of 1.8 V including the LUMO, LUMO+1 and LUMO+2 states. **b**) High resolution STM image of a dimer (2.6 nm x 2.1 nm, 0.5 V, 50 pA). **c**) Molecular model used for the calculations in **a**. **d**) The most striking features of the calculation, molecular model and STM image are labeled with colored ellipses.

5.4.1 Discussion

A significant contribution to the differences in energy is most likely a strong repulsion between terminal hydrogen atoms. That is, if the hydrogen atoms were allowed to relax during the energy calculation, the resulting energy of the heterochiral dimer was significantly lower (Fig. 5.11a top dimer) compared to a dimer with fixed hydrogen positions (Fig. 5.11a bottom dimer). The small difference between the two heterochiral dimers may be attributed to slight differences in the overlap of both helices, resulting in the heterochiral dimer shown in Fig. 5.11c having the lowest energy. It should be noted that the molecules in a dimer are differently aligned than in the zigzag rows in the close-packed monolayer, which is likely the result of additional repulsive forces due to close-packing. Different alignments of the molecules have been found depending on the coverage[47].

5.5 Summary and Conclusions

In summary, the results for enantiopure and racemic [7]H reflect an important aspect of molecular self-assembly on crystalline surfaces. Molecules can only establish dense layers in the limitation of an adsorption grid, which is the result of preferred adsorption sites. This grid only allows certain intermolecular distances; i. e. one step on the grid closer imposes substantial repulsion and one step further away leads to much lower attraction and density of the 2D crystal. Slight differences in the adsorption grid, i. e. higher atomic distances on Ag(111) and Au(111) compared to Cu(111) can than lead to less denser packing as found for enantiopure [7]H (see Tab. 4.1 and Fig. 4.5). This kind of site limitation seems to enhance stereochemical recognition processes.

In addition to the intermolecular interactions and lower dimensionality of the 2D system, in particular the interplay between molecule-molecule and molecule-substrate interactions governs the outcome of close packing[80]. The molecular interactions depend on the coverage, in a way that with increasing coverage, repulsive steric interactions increase and possibly lead to a change in structure, e. g. as observed for *M*-[7]H on Au(111) and the different zigzag row structures on Cu(111)[47].

However, it is possible that the interplay between available adsorption sites and intermolecular interactions does not lead to favorable structure with identical adsorption sites. If the molecule-molecule interactions are sufficient compared to the molecule-substrate interactions, structures where the molecules have different adsorption sites can be formed. This is the case in the close-packed structure of *M*-[7]H on Ag(100) (Fig. 4.3) and the quadruplet polymorph on Au(111) (Fig. 4.4c), where the adlattice has even a different symmetry than the substrate.

6 2D Crystallization of [5,6,9,10]-Dibenzopentahelicene

In this chapter the self-assembly of [5,6,9,10]-dibenzopentahelicene (db[5]H) on an Au(111) surface will be described. Db[5]H is an isomer to [7]H also exhibiting helical chirality, as shown in Fig. 6.1.

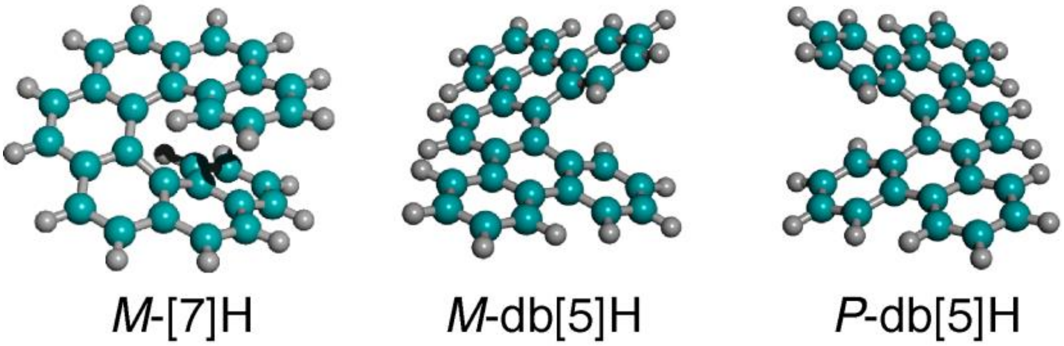

Fig. 6.1: Ball-and-stick molecular models for the $C_{30}H_{18}$ isomers *M*-[7]H, *M*-db[5]H and *P*-db[5]H.

All images in this chapter were taken with an Omicron Variable Temperature STM (see chapter 3.1.1). *Rac*-db[5]H and *M*-[7]H were evaporated from a Knudsen cell held at 170 °C and 160 °C, respectively, onto the crystal kept at RT. After deposition, the crystal was cooled with liquid helium to approximately 60 K during the measurements. The $[1\bar{1}0]$ surface direction is pointing up (north) in the images.

6.1 The First Layer on Au(111)

After the deposition of db[5]H on the Au(111) surface ordered structures were only observed at full monolayer coverage ($\theta = 1$). At lower coverages, the mobility of the molecules was too high to observe ordered structures. The ordered structures formed by *rac*- db[5]H are shown in the following Fig. 6.2.

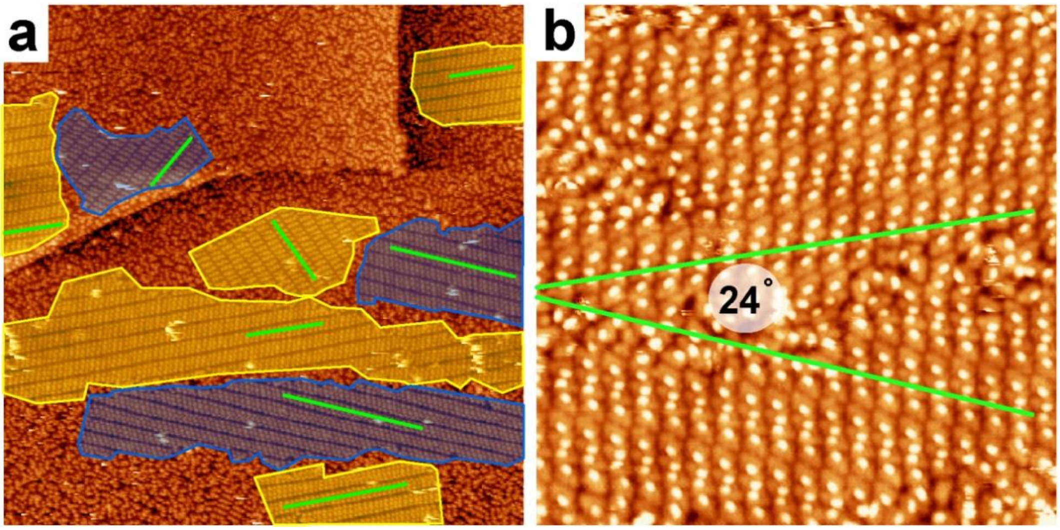

Fig. 6.2: STM image of the first layer db-[5H] on Au(111). (**a**) Enantiomorphous and rotational domains coexisting with disordered areas. Opposite mirror domains are marked in blue and yellow (150 nm x 150 nm, -2.725 V, 0.025 nA). (**b**) STM image two mirror domains and their disordered boundary. The rows include an angle of 24° (30 nm x 30 nm, 2.051 V, 0.028 nA).

Ordered crystalline structures are embedded in non-ordered areas. Even at small cooling rates a completely ordered monolayer could not be prepared, most likely because the mobility of the molecules at the nucleation and growth temperature was too low. On a larger scale, the ordered structures appear as rows running along a specific direction marked with green lines in Fig. 6.2a. Some domains can be superimposed by a rotation of 120° (marked in the same color) and some have to be reflected (marked in different colors). These mirror domains include an angle of 24° (Fig. 6.2b) and have an angle of ± 12° with respect to the $[11\bar{2}]$ surface direction.

Whether the observed mirror domains are racemic, or consist only of one enantiomer can be deducted from STM images with submolecular resolution. In Fig. 6.3 STM images of both mirror domains are shown.

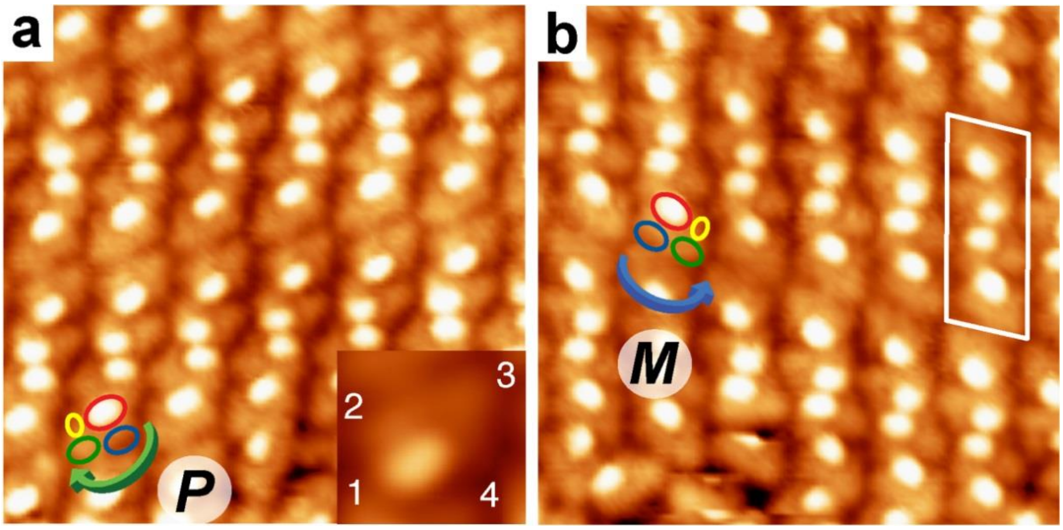

Fig. 6.3: STM images with submolecular resolution of two mirror domains consisting of *P*-db[5H] (**a**) and *M*-db[5H] (**b**). The appearance of a single molecule is dominated by an off-centered bright protrusion. Averaged over 30 positions four protrusions within one molecule are visible (inset in **a**). Going from bright to dark within the molecule allows the assignment of the absolute helicity. The unit cell (marked in **b**) contains four molecules (10 nm x 10 nm, 2.051 V, 0.028 nA).

The molecular appearance is dominated by a slightly off-centered bright protrusion. Within one domain this protrusion is always on the same side for all molecules, indicating homochiral domains. By averaging over 30 positions (inset in Fig. 6.3a) three additional protrusions are distinguishable, marked red-blue-green-yellow in Fig. 6.3 and Fig. 6.4d. Going from the brightest to the darkest protrusion gives a clockwise or anticlockwise descent and thus the absolute helicity. Following this procedure, the yellow marked domains in Fig. 6.2a consist only of *M*-db[5H] and the blue domains of *P*-db[5H]. The unit cell – marked in Fig. 6.3b – is composed of four molecules arranged as two pairs rotated by 180° with respect to each other.

The exact alignment of the molecules in such a dimer is obtained by superpositioning a high resolution STM image with molecular model of db[5]H as shown in Fig. 6.4. The upper rings of the helices of the molecules are placed to coincide with the bright protrusions and the lower edge to fit the contrast in the image. As a result, the molecules are tilted by 45° with respect to each other. They also overlap slightly; i. e. the upper terminal ring of one molecule is located above the 3rd ring of the second. In the unit cell two dimers are rotated by 180° as shown in Fig. 6.4 d, which is the result of the extended model described below.

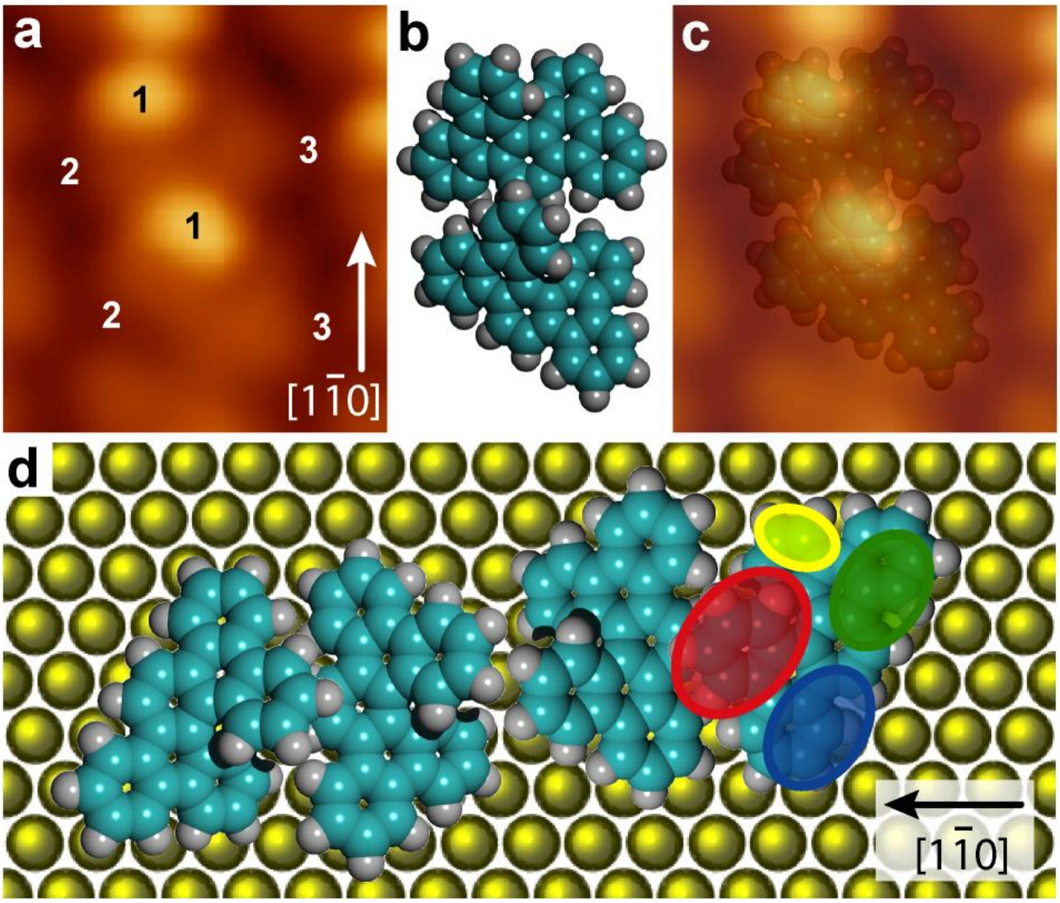

Fig. 6.4: STM image (**a**, 2.051 V, 28 pA, 30 times averaged), molecular model of a homochiral db[5]H dimer (**b**) and their superposition (**c**). The two molecules in the dimer are rotated by 45° with respect to each other and overlap slightly. (**d**) Arrangement of two dimers in the unit cell as a result of the extended model in Fig. 6.5.

To further confirm the expected conglomerate formation of *rac*-db[5H] and obtain the exact arrangement in the unit cell of the ordered monolayer, molecular models of homo- and heterochiral packing motifs were superimposed with a STM image. Therefore, three different db[5]H dimers – the homochiral dimer derived from Fig. 6.4 (Fig. 6.5 a) and two heterochiral dimers (Fig. 6.5 b, c) – were tested for the possibility to build a close packing motif in agreement with the STM image. The best fit is achieved with the homochiral dimer (*M*-*M* in Fig. 6.5 d): the upper terminal ring of each molecule coincides with the bright protrusions in the STM image and the lower molecular edge fits the STM contrast (blue ellipse). If the dimers are assembled with identical packing density, one heterochiral dimer has *a priori* a strong overlap (Fig. 6.5 b, red ellipse). Another arrangement of the heterodimer can be packed with a similar overlap and equal density as the homodimer, but its close packing contradicts the contrast in the STM image.

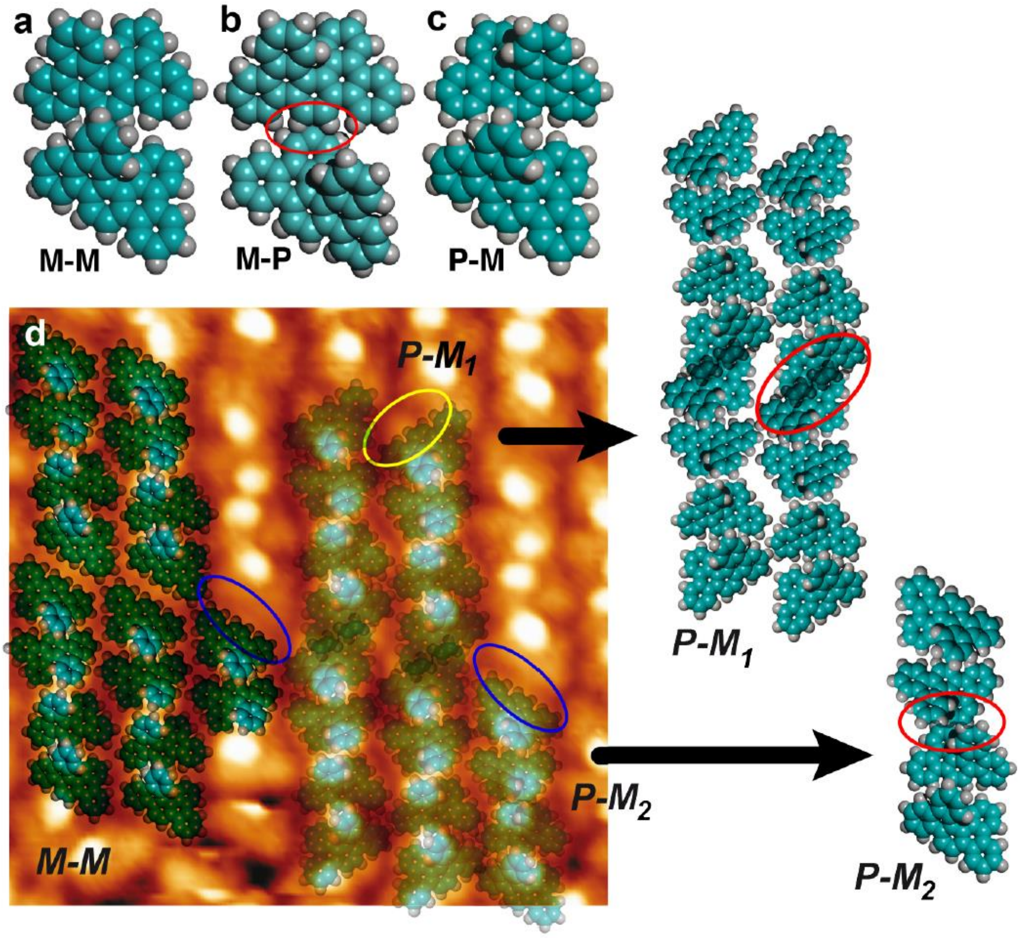

Fig. 6.5: Superposition of homochiral (**a**) and heterochiral (**b, c**) dimers with the high resolution STM image identical to Fig. 6.3 b (**d**, 10 nm x 10 nm, 2.051 V, 0.028 nA). Close packing of the *M-M* dimer fits the STM image. The *M-P* dimer has *a priori* a too strong overlap (**b**, red ellipse), if packed with the same density as the homodimer. The *P-M* dimer can be packed with an equal density, but the close packing does not fit to the STM image.

Even though the upper helix of each molecule can be arranged to coincide with the bright protrusions, the lower molecular edge does not fit the STM contrast (Fig. 6.5 *P-M$_1$*, yellow ellipse) and in an extended layer there is a strong overlap between the unit cells (Fig. 6.5 *P-M$_1$*, red ellipse). By taking the opposite enantiomers in the Fig. 6.5 c heterodimer, the lower molecular edge fits the STM contrast (Fig. 6.5 *P-M$_2$*, blue ellipse). However, the upper terminal ring of the molecules does not coincide with the bright protrusions and the close packing required for a pair of dimers to fit into the unit cell results in a too strong overlap (Fig. 6.5 *P-M$_2$*, red ellipse).

To summarize the 2-dimensional crystalline structure formed by db[5]M, a 2 x 3 unit cell model of the *M*-enantiomer with the Au(111) surface is depicted in Fig. 6.6. It shows the partly overlap of the molecules along the $[1\bar{1}0]$ direction, but no overlap is existent perpendicular to this, i. e. along the

$[11\bar{2}]$ direction. A unit cell contains four molecules and covers 78 gold atoms. The matrix notation of the unit cell is $\begin{pmatrix} 6 & 2 \\ 0 & 13 \end{pmatrix}$ and the length of the vectors is 1.52 nm and 3.74 nm, respectively.

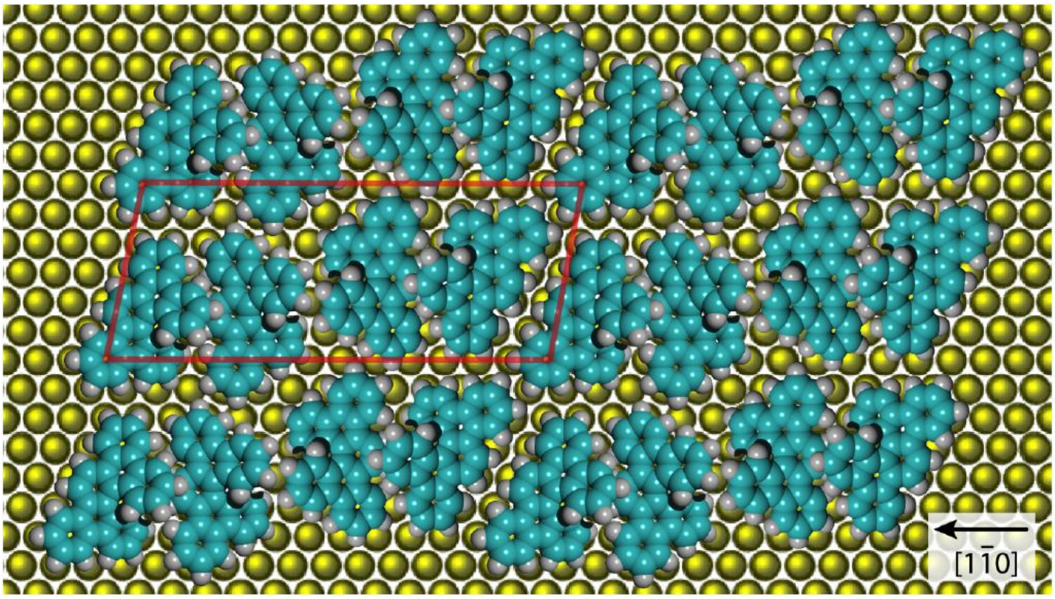

Fig. 6.6: Model of a 2 x 3 unit cell arrangement of *M*-db[5]H on Au(111) as a result of the modeling described above. The arrangement of the molecules is identical to the *M*-*M* superposition model in Fig. 6.5 d, rotated by 90°.

6.2 Doping with *M*-Heptahelicene

In order to study diastereomeric recognition processes based purely on van-der-Waals interactions, *M*-[7]H is mixed into the *rac*-db[5]H monolayer. This mixing lead to a shift in the balance between the enantiomorphous domains of *M*- and *P*-db[5]H. In a monolayer consisting of only 10% *M*-[7]H and 90% db[5]H the balance seemed to be already shifted toward the *M*-db[5]H enantiomorph, marked blue in Fig. 6.7.

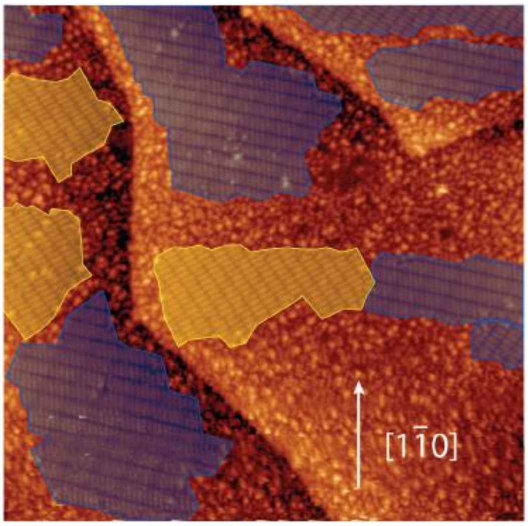

Fig. 6.7: STM image of a monolayer containing 90% *rac*-db[5]H and 10% *M*-[7]H. The area covered by the *P*-db[5]H enantiomorph (yellow) is smaller than the area covered by the *M*-db[5]H enantiomorph (blue). (Measurement parameters: 150 nm x 150 nm, -2.725 V, 31 pA)

In a monolayer containing 80% *rac*-db[5]H and 20% *M*-[7]H, the domains consisting of *M*-db[5]H are the only ordered structures left, as shown in Fig. 6.8. In addition to the suppression of the formation of the *P*-db[5]H domain, the doping with *M*-[7]H also seems to lead to a higher degree of disorder and overall smaller ordered domains in the monolayer.

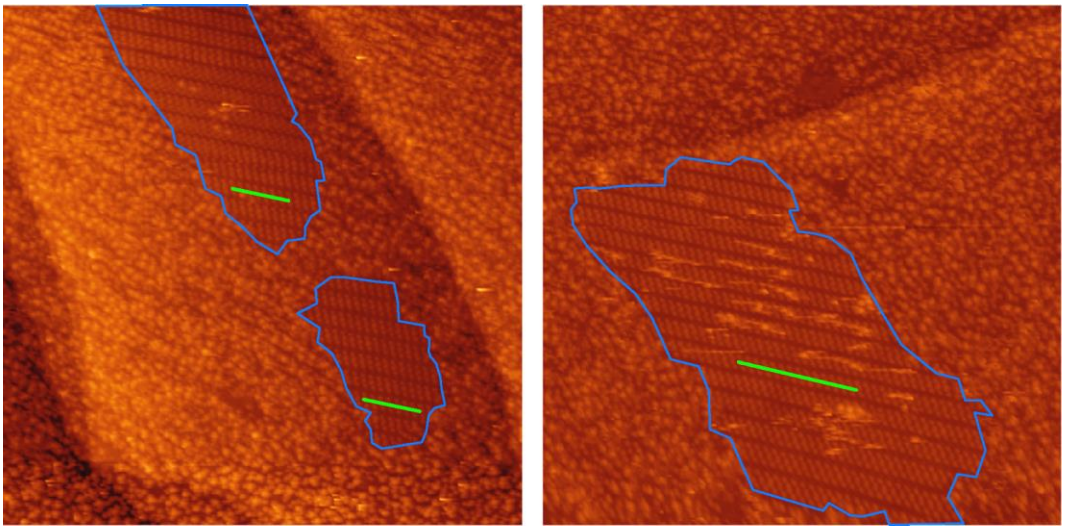

Fig. 6.8: STM images of a monolayer consisting of 80% *rac*-db[5]H and 20% *M*-[7]H (Measurement parameters: 100 nm x 100 nm, -2.725 V, 66 pA (left) and 31 pA (right))

To evaluate the overall effect of the doping with *M*-[7]H, the domain distribution, number and size of ten 200 nm x 200 nm images doped with 5%, 10%, 15% and 20%, respectively, were analyzed. In Fig.

6.9 the percentage of *M*-db[5]H domains and the overall ordered area are plotted against the amount of *M*-[7]H in the monolayer. It clearly shows a gradual increase in the percentage of the *M*-db[5]H enantiomorph with increasing doping amounts until only the *M*-db[5]H enantiomorph is left in the monolayer.

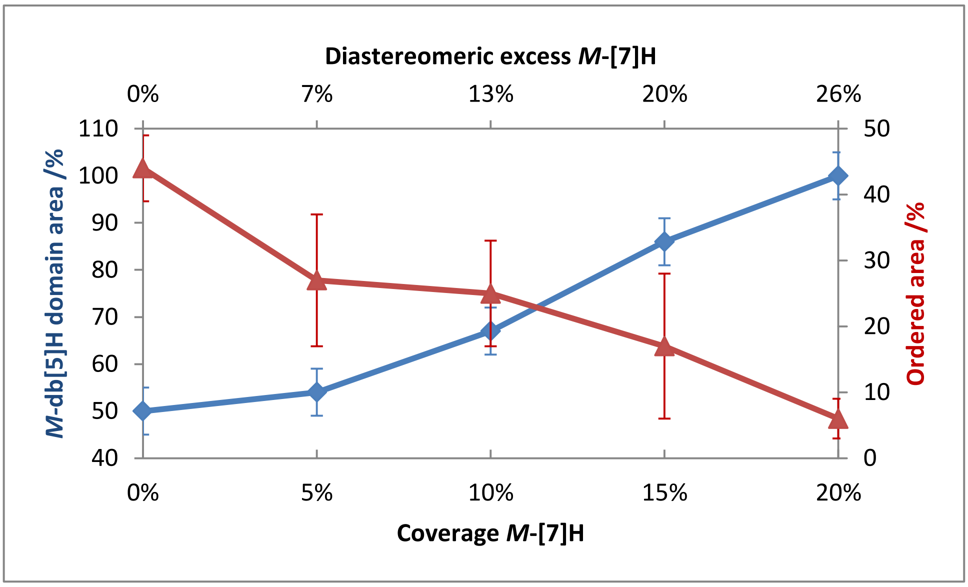

Fig. 6.9: Dependence of the overall ordered area (red) and the percentage of *M*-db[5]H domains in the monolayer on the doping with *M*-[7]H. The amount of *M*-[7]H in the monolayer is given in percentage of the covered area (bottom axis) and as relative molar amount (top axis).

In addition to the shift in balance between the enantiomorphous domains the degree of disorder also increases with the amount of *M*-[7]H mixed into *rac*-db[5]H, e. g. less than 10% of the surface is on average covered with ordered *M*-db[5]H domains with a coverage doping of 20% and the domain size drops below half of the size observed without doping. All obtained statistics are summarized in Table 6.1.

Table 6.1: Summary of the statistical analyses.

Coverage doping	Amount of *M*-7[H]	Nr of 200 x 200 nm images	Total area probed /nm^2	Ordered area /nm^2	Percentage of ordered area	Percentage *M* domains	Avg. Domain Size (*M*)	Avg. Domain Size (*P*)
0%	0.00%	10	400000	17627	44 ± 5	50	1091	
5%	6.60%	10	400000	10876	27 ± 10	54	655	498
10%	13.20%	10	400000	9815	25 ± 8	67	1119	714
15%	19.80%	10	400000	6860	17 ± 11	86	689	250
20%	26.40%	10	400000	2576	6 ± 3	100	447	

6.3 Discussion

All obtained STM images show a substantial amount of disordered areas. Even without doping with *M*-[7]H only about half of the surface is covered with ordered domains. The amount of disorder can be explained by the mass transport required for the conglomerate formation: apparently the cooling rate was too fast and thus during nucleation and growth the mobility of the molecules was too low. In contrast to the high amount of disorder, a much higher degree of order was achieved for *rac*-[7]H on Cu(111), where a racemic monolayer is formed and thus no mass transport was required. Additionally, mixing only 9% of *P*-[7]H in a monolayer of *M*-[7]H on Cu(111) was enough to prevent the formation of ordered domains[47]. This incomplete segregation of the enantiomers leads to unbalanced mixtures in the vicinity of the enantiopure domains, which is the actual reason for the observed disorder. By mixing *M*-[7]H in the monolayer the amount of disorder further increases down to less than 10% of the surface covered with ordered domains. The doping induces an additional chiral conflict and decreases the enantiomeric balance and thus supports the scenario that an enantiomerically unbalanced layer suppresses the formation of ordered structures.

The shift in balance between both enantiomorphous domains upon mixing *M*-[7]H into the *rac*-db[5]H layer should be discussed in the context of co-operative effects in the interaction of different chiral species at surfaces. These are similar to the “sergeant-and-soldiers” or “majority-rule” experiments in polymer science, where a small chiral bias from side chains in helical polyisocyanate co-polymers induced single helicity[81,82]. In 2D systems single handed enantiomorphism could be induced with the prochiral molecules succinic acid and *meso*-tartaric acid, which turn chiral at the Cu(110) surface and form 2D conglomerates[83,84], presumably by the formation of a distorted zigzag adsorbate[85]. A small chiral bias induced by doping with (*R, R*)- or (*S, S*)-tartaric acid on Cu(110) was sufficient to switch all prochiral molecules into a single handedness[86,87]. Thereby, the handedness of a single molecule is defined by the zigzag alignment of the molecular C_4 backbone, which has been shown by XPD measurements for (*R, R*)- and (*S, S*)-tartaric acid on Cu(110)[88]. Chiral amplification in 2D has also been shown for [7]H on Cu(111). In that case, chiral bias from a rather small *ee* caused the single handedness of the entire surface. The chiral entity was not a single molecule, but a heterochiral pair with two possible enantiomorphous alignments, as described in detail in chapter 2.1.3.

In contrast to the described amplification mechanisms, the imbalance of the enantiomorphous domains changes gradually with increasing *M*-[7]H content (Fig. 6.9). Therefore, in the present helicene mixtures *M*-[7]H apparently captures preferably *P*-db[5]H in the disordered area and a chiral conflict between the two species is the basic cause for the shift in balance between the mirror domains. Since there are no polar groups present, the interaction between the diastereomers has to be of van-der-Waals type. Thus, the diastereomeric pair formation is stronger with more overlap between the molecules. Different models for possible pair formations between *P*-db[5]H and *M*-[7]H (a-c) and *M*-db[5]H and *M*-[7]H, respectively, are shown in Fig. 6.10. The largest overlap is found for the heterochiral pair in Fig. 6.10 b, supporting the scenario that *M*-[7]H preferably captures *P*-db[5]H in the disordered area.

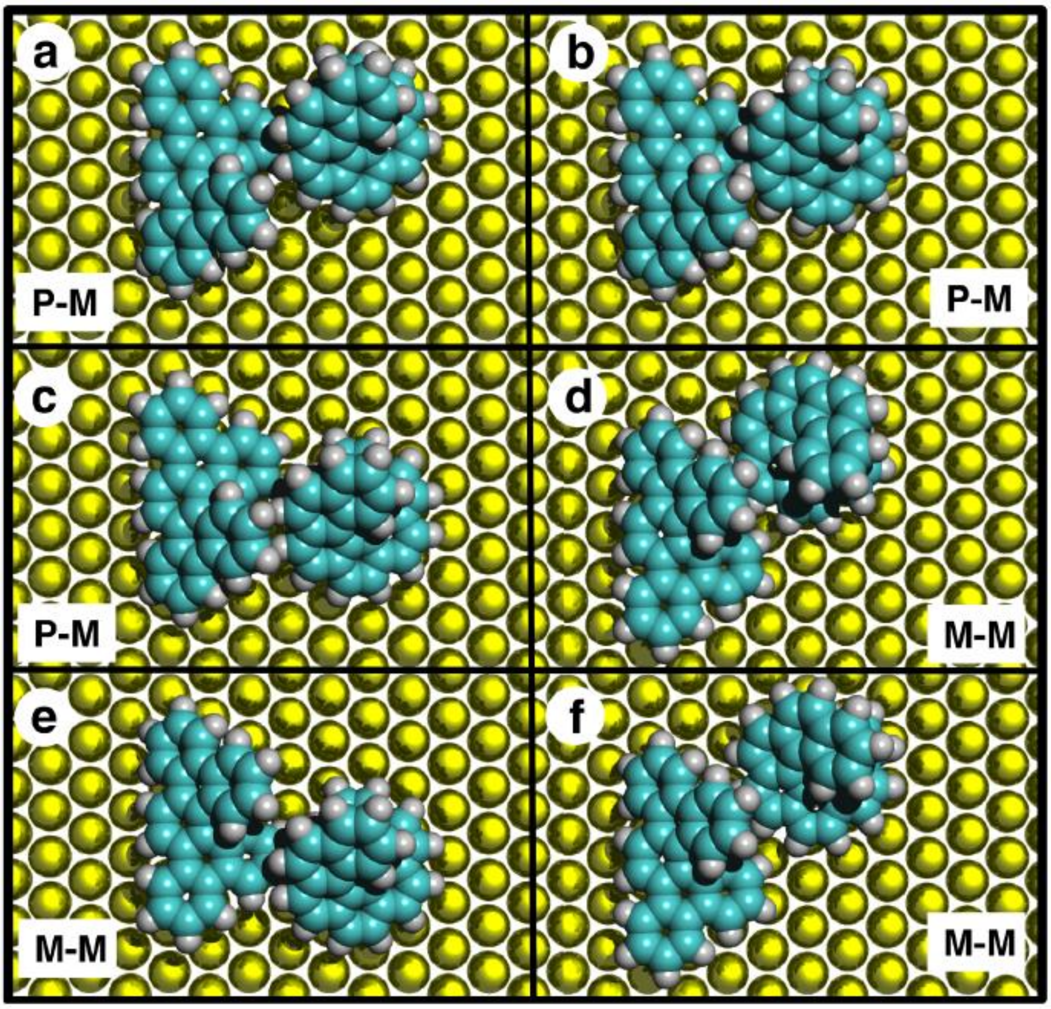

Fig. 6.10: Models for possible diastereomeric interactions between *P*-db[5]H and *M*-[7]H (a-c) and *M*-db[5]H and *M*-[7]H (d-f). These examples show the closest arrangements found for *P*-*M* and *M*-*M* combinations.

Such a diastereomeric pair may induce disorder in the surrounding layer, increasing the overall disorder and the effect of enantiomorph suppression as a co-operative effect to the diastereomeric pair formation: assuming that the db[5]H enantiomers have to separate for nucleation and growth and the mixed in *M*-[7]H are preferably present in areas with a high *P*-db[5]H concentration, only *M*-db[5]H has the ability to nucleate.

All in all, these results show that polar forces are not required in order to suppress the formation of a single enantiomorph, like previously observed for dicarboxylic acids Cu(110). Tartaric acid forms a conglomerate on Cu(110) and the growth of one enantiomorph was suppressed by coadsorbing one malic acid enantiomer[89]. Adsorbing an excess of one enantiomer suppressed the formation of the domains containing the minority enantiomer[90]. Responsible for the suppression of the *P*-db[5]H enantiomorph by doping with *M*-[7]H is rather the balance of homo- and heterochiral interactions and thus the intermolecular lateral recognition should be purely based on van-der-Waals forces.

The surface has been shown to play an important role in the enantiospecific interaction between adenine and phenylglycine[91], where the selective diastereomer interaction was explained by a substrate mediated charge transfer and Coulomb repulsion between the amino groups of the two species[92]. A substrate-induced polarization has also been shown to support the conglomerate formation of 6,13-dicyanoheptahelicene on Cu(111)[52]. The surface may be important for chiral interactions of other polar molecules as well, e. g. chiral reconstructions of Cu(110) were observed in STM studies with adsorbed malic acid[93,94] and tartaric acid[95]. Here, however, the influence of the surface should be limited to favored binding sites, since even the herringbone reconstruction is still visible below the monolayer (dark stripes in Fig. 6.2 b).

7 Bisheptahelicene

In this chapter the self-assembly of two covalent coupled heptahelicene molecules is investigated. They are coupled in the 9-position and the coupling reaction (see appendix) was carried out with a racemic mixture of 9-bromo[7]H, which leads to the three possible isomers shown in Fig. 7.1. If equal probabilities for each coupling possibility are assumed, the resulting mixture consist of 50% of the *meso*-compound (*P, M*)-[9,9']-bisheptahelicene ((*P, M*)-bis[7]H), 25 % of the chiral (*M, M*)-bis[7]H and 25% (P, *P*)-bis[7]H.

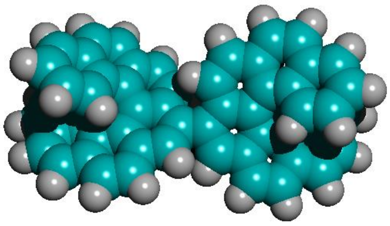

(*P, M*) -[9,9']-bisheptahelicene

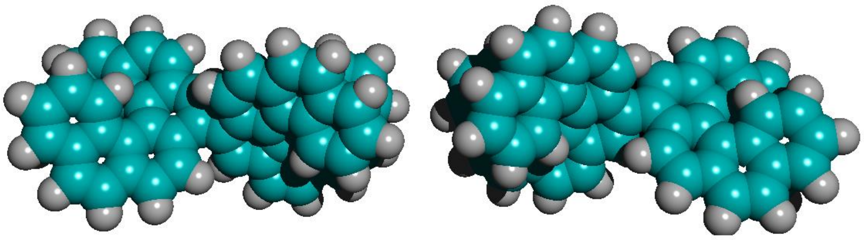

(*M, M*) -[9,9']-bisheptahelicene

(*P, P*) -[9,9']-bisheptahelicene

Fig. 7.1: Space-fill models of the three possible isomers of [9,9']-bisheptahelicene.

The STM measurements of the monolayer structures have been performed earlier by Dr. Manfred Parschau with the commercial Variable Temperature Omicron STM (see chapter 3.1.1) at a sample temperature of 50 K. The single molecule and cluster images and manipulations were performed at the home-built low temperature STM (see chapter 3.1.1) at a sample temperature of 10 K. In both cases, the molecules were evaporated from a Knudsen cell held at 300 °C.

7.1 Ordered Structures on Cu(111)

The structures formed by bis[7]H in the saturated monolayer on Cu(111) are shown in Fig. 7.2. One of the observed structures exhibits enantiomorphism, i. e. the unit cell consists of clusters with four bright lobes, which are aligned in a clockwise or counter clockwise fashion as indicated in the insets in Fig. 7.2a. In the following, this structure will be referred to as α structure. The second, in the following called β structure, is coexisting with the α structure, preferentially on different terraces as shown in Fig. 7.2b. In this β structure the bright lobes are aligned in lines, in which four lobes are closer packed at a time as marked yellow in the inset in Fig. 7.2b.

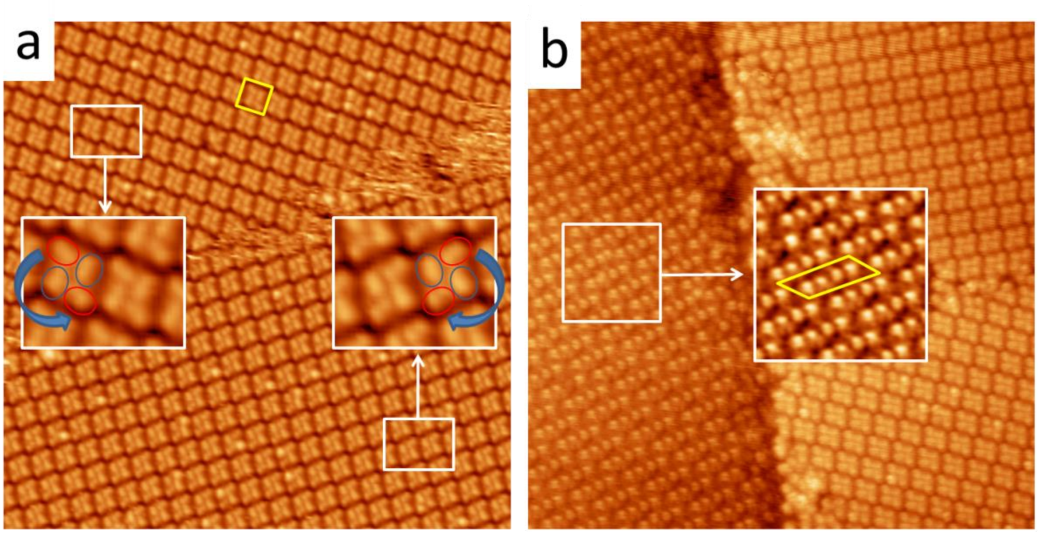

Fig. 7.2: STM images of the saturated monolayer of bis[7]H on Cu(111). **a**) The unit cell (marked yellow) in the two adjacent enantiomorphous domains consists of four protrusions aligned in a mirror-like fashion as highlighted in the insets (α structure). **b**) In a coexisting second (β) structure a possible unit cell (marked yellow in the inset) consists of four closer aligned protrusions. (Measurement parameters: **a**) 40 nm x 40 nm, 2.09 V, 20 pA; **b**) 40 nm x 40 nm, 1.93 V, 43 pA) Images courtesy of M. Parschau.

In order to determine the exact alignment of the molecules in the monolayer, molecular models were fit to the obtained STM images. Therefore, it was assumed that each bright protrusion corresponds to one helix in the bis[7]H molecule. A distinct assignment of the molecular ordering in the monolayer was not possible, that is, for the α structure three possibilities shown in Fig. 7.3a-c were found and two for the β structure shown in Fig. 7.3d-e. In the α structure there could be two ways for the arrangement of two molecules in each clusters (a + b) or two molecules may connect two clusters (c). In the β structure the molecules could be aligned in lines with two molecules being closer together (d), or three molecules could be arranged as a “Z” (e).Additionally, it was not possible to determine of which of the bis[7]H isomers each structure consists.

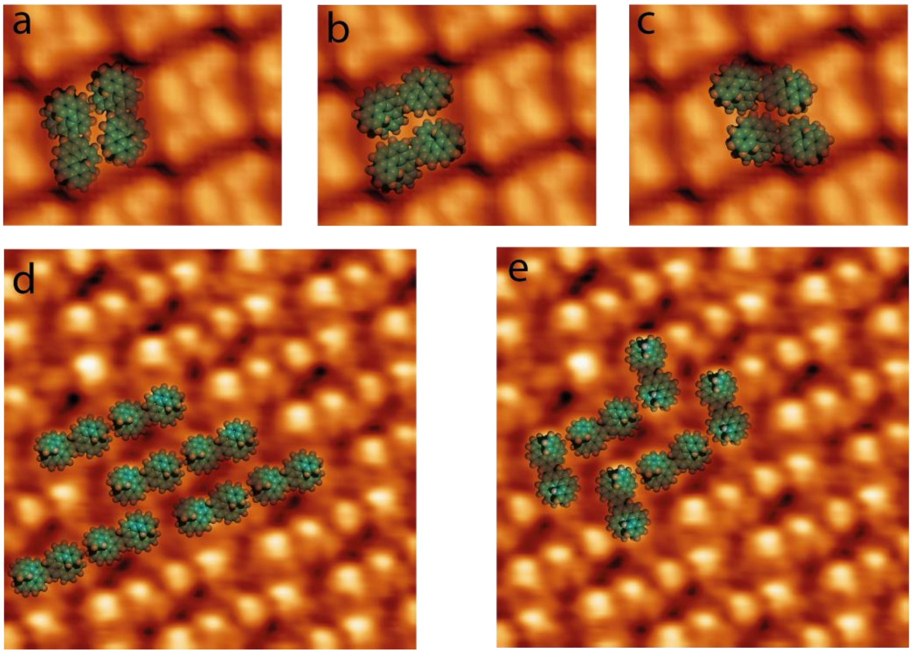

Fig. 7.3: Superposition of high resolution STM images and molecular models. If each bright protrusion is related to one helix, several molecular alignments are possible. **a**-**c** show three alignments of two bis[7]H molecules in the α structure; **d**-**e** show two possibilities for the molecular alignment in the β structure. (Measurement parameters: **a**-**c**) 5 nm x 4 nm, 2.09 V, 20 pA; **d**-**e**) 10 nm x 10 nm 1.93 V, 43 pA)

7.2 Clusters and Single Molecules on Cu(111)

If the Cu(111) was cooled to approximately 40 K during the deposition of the bis[7]H molecules, mostly single isolated molecules were found on the terraces. High resolution images of these showed different contrasts, that is, symmetric and asymmetric appearing molecules as illustrated in Fig. 7.4. A comparison of the STM images and molecular models allows the assignment of the *meso M, P*-bis[7]H to the symmetric molecules and the chiral *M, M*- or *P, P*- bis[7]H (Fig. 7.4e), respectively, to the asymmetric molecules. These appear as mirror images in the STM (Fig. 7.4c, f), but the obtained resolution is not sufficient to assign the *M, M* or *P, P* isomers to a specific molecule in the STM image.

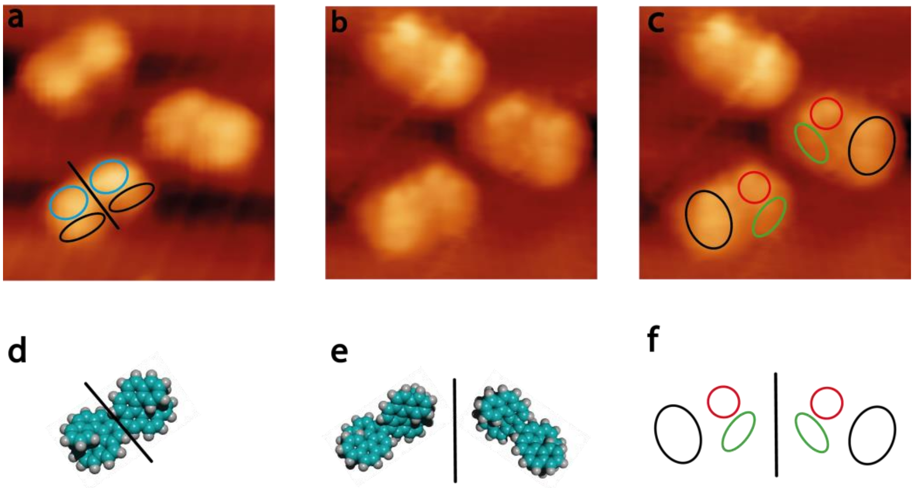

Fig. 7.4: **a**) STM image showing three isolated bis[7]H molecules. The molecules have two different appearances, i. e. asymmetric protrusions (right molecule) or two symmetric protrusions with a mirror plane (both left molecules). The *meso P,M*-bis[7]H (d) has also a mirror plane. **b**) STM image showing two asymmetric molecules. The asymmetric molecules exhibit enantiomorphism similar the *M,M*-bis[7]H and *P,P*-bis[7]H pair (**e**), that is, the molecules can be imaged as three lobes (**c**) with mirror symmetry (**f**). (Measurement parameters: 6 nm x 6 nm, **a**) 1.63 V, 74 pA; **b** and **c**) 1.29 V, 87 pA)

After annealing the sample with the single molecules to room temperature, decorated step edges and clusters composed of a few molecules each on the flat terraces (Fig. 7.5a) were formed. Frequently observed clusters consisting of four and six lobes are shown in Fig. 7.5b and d. Both of these clusters appear as mirror images as indicated in Fig. 7.5c and e and exhibit C_2 or C_3 symmetry, respectively.

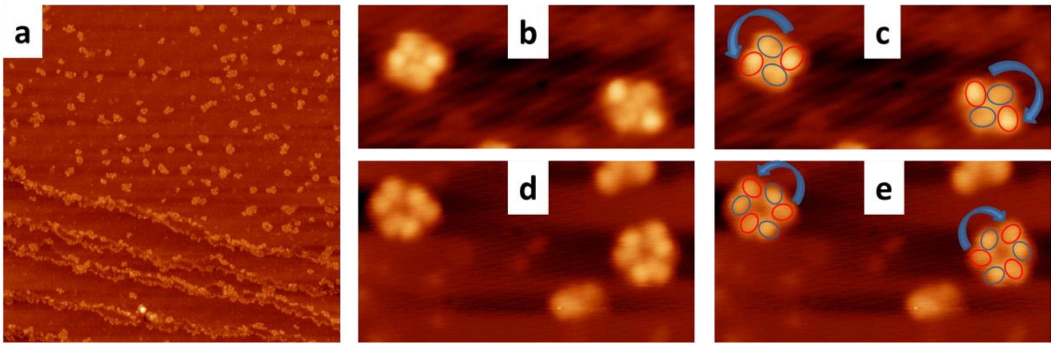

Fig. 7.5: **a**) Large area STM image showing decorated steps and clusters on a flat terrace. **b** and **d**) High resolution images of frequently observed clusters. The clusters in **b** consist of four lobes, two of which are darker. In **c** the different lobes are superimposed with blue and red ellipses, respectively, to illustrate the clockwise or counterclockwise arrangement of the clusters. The clusters in **d** consist of six lobes with alternating two different brightnesses. In **e** the superposition with red and blue ellipses illustrates the mirror-like relation of the two clusters. (Measurement parameters: **a**) 137 nm x 137 nm, 1.29 V, 59 pA; **b**) 12.7 nm x 5.4 nm, 1.29 V, 59 pA; **d**) 16 nm x 8.7 nm, 1.51 V, 64 pA)

In order to identify the composition and position of the molecules in the observed clusters, they were taken apart with the lateral manipulation function, i. e. the STM tip was moved to the starting point, brought closer to the surface and moved to the end point with a fixed tunneling current and voltage applied during the lateral movement. In Fig. 7.6 the manipulation series of two four lobe and one six lobe clusters are shown. In the first manipulation attempt from Fig. 7.6a to b the molecules were not completely separated and a second manipulation was necessary (Fig. 7.6b), in which the other molecule was moved. In the second series (Fig. 7.6d and e) one lateral manipulation attempt, starting at a brighter lobe instead of a darker as in the series before, was sufficient to separate the cluster. The manipulation series of the six lobe cluster (Fig. 7.6f-h) shows its separation into three single molecules. Additionally, the molecules also were slightly rotated during the lateral movement.

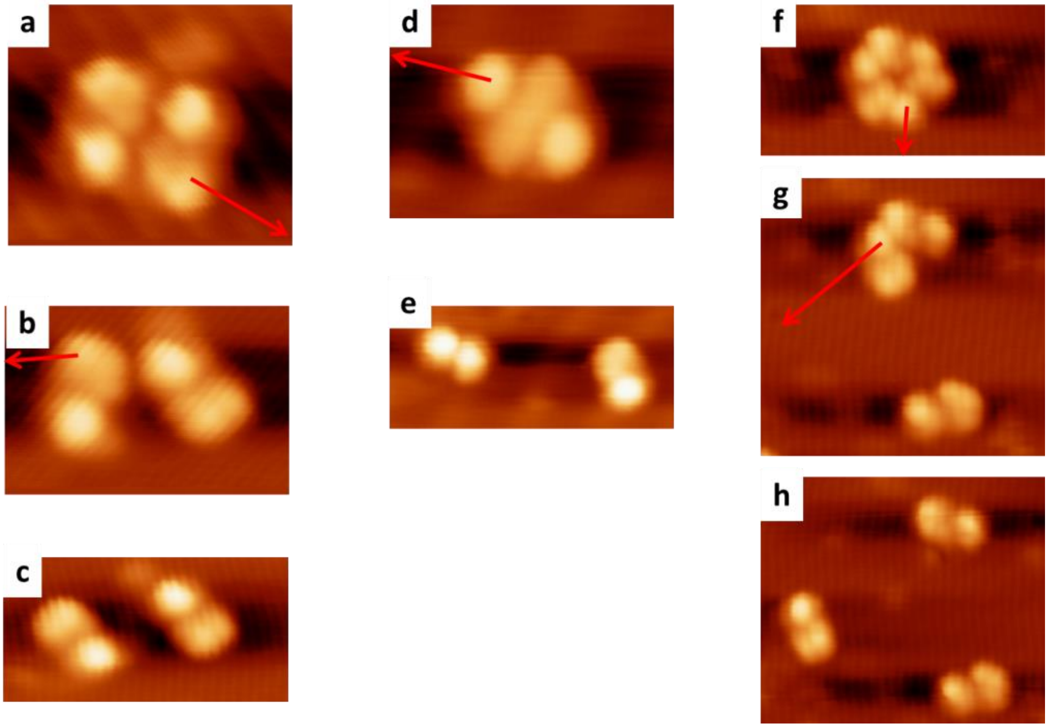

Fig. 7.6: Series of STM images showing the lateral manipulations of a dimer (**a**-**c** and **d**-**e**) and a trimer (**f**-**h**). The starting point and movement direction of the tip during the manipulation are indicated by the red arrows. (Measurement parameters: **a**) 4.6 nm x 3.9 nm, **b**) 5.2 nm x 3.4 nm, **c**) 7.1 nm x 3.6 nm, **d**) 5.3 nm x 3.9 nm, **e**) 8.6 nm x 3.7 nm, 1.51 V, 59 pA; **f**) 8.0 nm x 4.2 nm, **g**) 8.0 nm x 7.8 nm, **h**) 8.7 nm x 7.5 nm, 1.51 V, 220 pA)

7.3 Discussion

The single molecule STM images in Fig. 7.4 reveal symmetric and asymmetric appearing molecules, which can be attributed to the isomers of bis[7]H shown in Fig. 7.1. The different apparent height of the two helices within one molecule can be attributed to a different tilt angle with respect to the surface. The ratio of the isomers may differ from the statistical distribution during the synthesis, if a coupling between homochiral or heterochiral helices is favored. This was observed in an experiment with a racemic mixture of helicinol, where a preferred coupling between two molecules of the same helicity was found[96].

The molecular alignment and composition of the α structure in Fig. 7.2 can be deduced by a comparison with the low coverage structures. From the low coverage cluster, the molecular alignment shown in Fig. 7.3c can be excluded, which leaves the possibilities shown in Fig. 7.3a and b. The manipulation series in Fig. 7.6 reveals the position of the two molecules within a cluster as shown in Fig. 7.7a and b for both mirror domains in the monolayer and the isolated cluster in Fig. 7.7c.

Comparing the single symmetric and asymmetric molecules shown in Fig. 7.4 with the single molecules after the manipulation in Fig. 7.6 indicates that the clusters are composed of the asymmetric appearing *P, P-* bis[7]H or *M, M-* bis[7]H, respectively. In contrast thereto, the *meso P, M*-bis[7]H appears symmetric (Fig. 7.4a). This assignment is supported by symmetry considerations, i. e. molecular models for dimers built of *P, M*-bis[7]H shown in Fig. 7.7e and h have C_{1v} symmetry, dimers of *P, P*-bis[7]H or *M, M*-bis[7]H, respectively, exhibit C_2 symmetry. The isolated as well as the dimers in the monolayer also exhibit C_2 symmetry (Fig. 7.7a, b and d). Thus it can be concluded that the α structure consists of chiral *M, M-* bis[7]H or *P, P-* bis[7]H, respectively, which are separated in the mirror domains and aligned as indicated in Fig. 7.7a and b. Since the β structure coexists it is likely to consist of the *meso M, P*-bis[7]H. No structure containing a trimer-like feature was found in the monolayer.

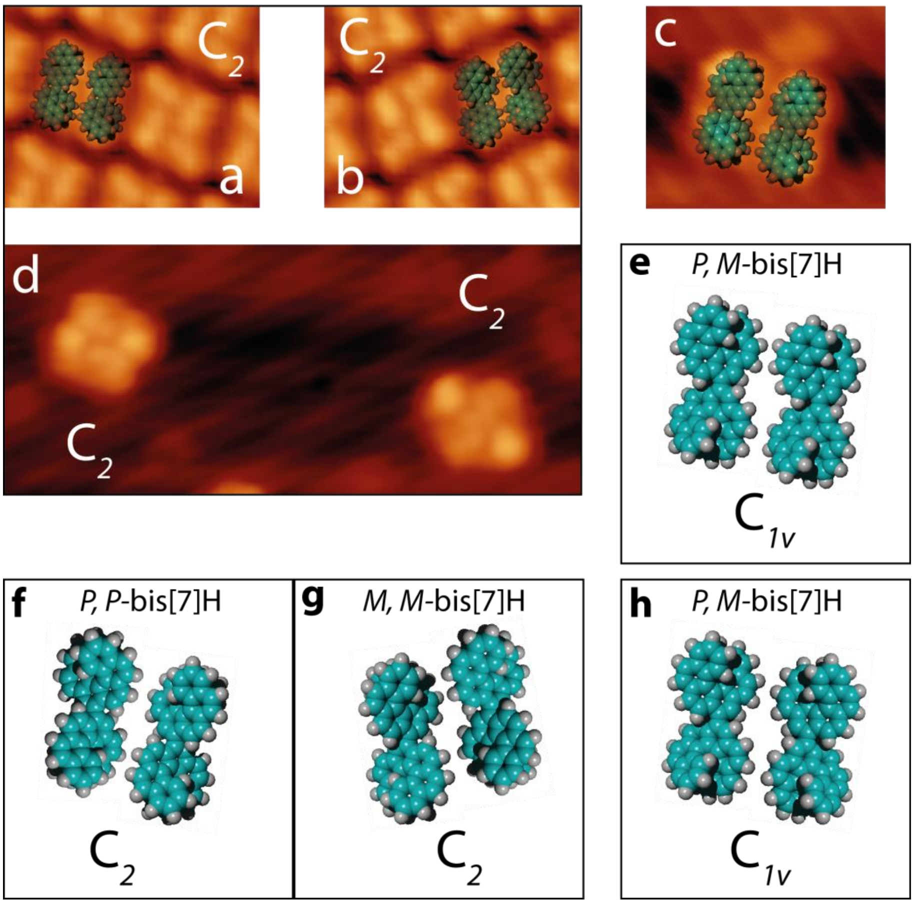

Fig. 7.7: a and **b**) STM images showing both enantiomorphs of the α structure in the monolayer and isolated dimers (**c** and **d**). The positions of the molecules shown in **c** are deduced from the manipulation experiments. The shown isolated dimers and in the ones in the monolayer exhibit enantiomorphism identical to the molecular models of *M, M-* and *P, P-* bis[7]H shown in **f** and **g**. Additionally, the dimers in the STM images and in **f** and **g** exhibit C_2 symmetry, which is not the case for the dimers consisting of *P, M-* bis[7]H shown in **e** and **h**. (Measurement parameters: **a** - **b**) 5 nm x 4 nm, 2.09 V, 20 pA; **c**) 4.6 nm x 3.9 nm, 1.51 V, 220 pA; **d**) 12.7 nm x 5.4 nm, 1.29 V, 59 pA)

In summary, the imaging and manipulation of single molecules and small clusters supported the analysis of complex structures observed in the saturated monolayer. The alignment of the molecules within the monolayer could be deduced unambiguously. However, for the presented interpretation of the isomer composition it was necessary to assume that the *meso M, P*-[7]H is achiral and appears as a symmetric molecule in the STM. However, if the rotation around the bond connecting the helicenes is hindered, the helices in the *M, P-* bis[7]H can be arranged in two enantiomorphous ways and one could think of a dimer with C_2 symmetry. Thus, for an unambiguous evaluation of the data, STM images showing the helicity of each helix would be necessary.

8 Pentahelicene

In this chapter, first experiments with pentahelicene ([5]H) on Cu(111) will be described. The molecular structures of *M*- and *P*-[5]H are shown in Fig. 8.1.

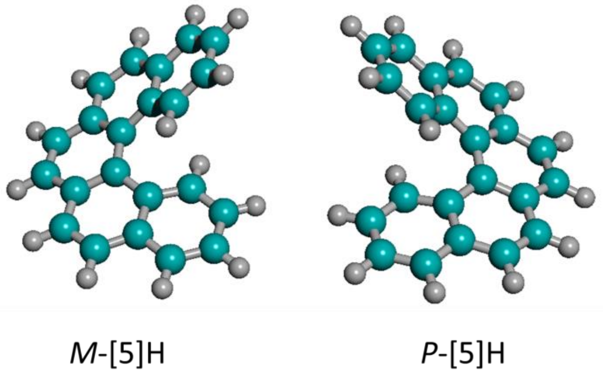

Fig. 8.1: Ball-and-stick molecular model for *M*-[5]H and *P*-[5]H.

All STM images in this chapter were obtained at with the home-built low temperature STM (see chapter 3.1.1) and a sample temperature of ca. 10 K. The [5]H molecules were evaporated from a Knudsen cell kept at a temperature of 100 °C onto the Cu(111) crystal kept at room temperature.

8.1 Single Molecules and Clusters

A racemic mixture of [5]H was evaporated on a Cu(111) crystal held at room temperature during the evaporation. In order to observe single molecules or clusters, the coverage was kept very low. After deposition, the step edges were decorated with [5]H molecules, the molecules on the flat terraces mostly adsorpted isolated and only a few in clusters, as shown in Fig. 8.2a. In the high resolution STM image, the single molecules appear round with a slightly off-centered protrusion. In some cases, two molecules form a dimer, where they are rotated by approximately 180° with respect to each other (Fig. 8.2b).

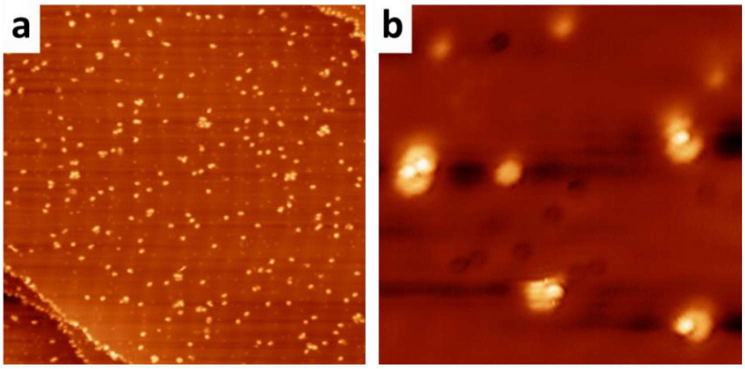

Fig. 8.2: **a**) Large area STM image of [5]H on Cu(111) at low coverage. Single molecules are located at the step edges, mostly isolated on the flat terrace and in some cases aggregated in small clusters. **b**) The molecules appear round with a brighter off-centered protrusion. (Measurement parameters: **a**) 100 nm x 100 nm, 1.914 V, 69 pA, **b**) 11 nm x 11 nm, 89 mV, 40 pA)

To determine the chirality of the single 5[H] and distinguish both enantiomers, molecular models were fit to the obtained STM data. In Fig. 8.3 high resolution STM images of a dimer, a single *M*- and *P*[5]H, respectively, are superimposed with a molecular model. This model clearly shows that the dimer is homochiral with the enantiomers rotated by 180° with respect to each other. The chirality of the single molecules can be determined by the position of the bright protrusion, which corresponds to the upper terminal ring of the [5]H molecule. Furthermore, all molecules shown in Fig. 8.3 are placed on identical adsorption sites.

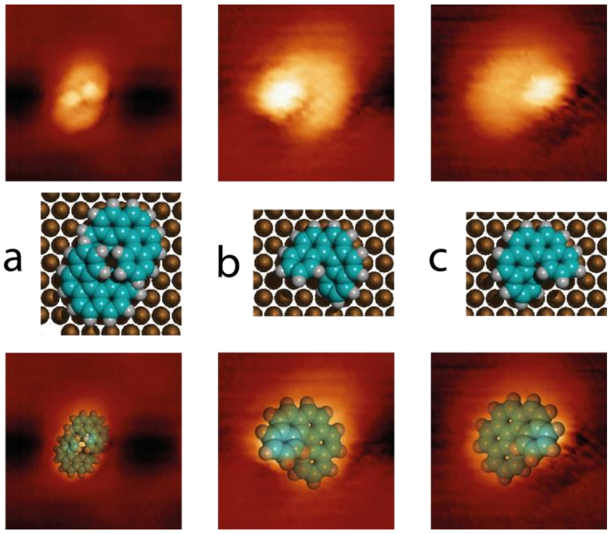

Fig. 8.3: STM images of a dimer and two single molecules (top), molecular models for the dimer (**a**), a single *P*-[5]H (**b**) and *M*-[5]H (**c**) and the superposition of the STM images and the fitting model (bottom). The upper terminal ring of a [5]H molecules coincides with the bright protrusion in the image. The dimer is homochiral and consists of two *M*-[5]H rotated by 180° with respect to each other. (Measurement parameters: **a**) 4 nm x 4 nm; **b** and **c**) 2 nm x 2 nm, 89 mV, 40 pA)

8.2 Manipulation of Single Molecules

The single [5]H molecules were deposited on the Cu(111) surface in order to perform manipulation experiments, i. e. switching the chirality of a molecule from *M*-[5]H to *P*-[5]H or *vice versa* by inelastic electron tunneling (IET). Therefore, the STM tip was moved to the bright protrusion of a [5]H molecule, a constant voltage applied and the current *vs.* time recorded. However, instead of a chirality switching, only jumps and rotations of the excited molecules were observed, even with applied voltages up to 2.2 V. At first sight, the rotation of a molecule seemed to favor one direction, as shown with a series of manipulations in Fig. 8.4. Therein, the position of the tip during the IET is marked by a black dot. In each spectra, after which a rotation occurred, one or more changes in the current trace are observed, whereas no rotation took place after the spectra without a change in current. After the last spectrum, the molecule disappeared by jumping out of the scanning area or attaching to the tip. In general, the current decreases after a change in the spectra prior to a rotation event, but in some cases the current increases again after a second or third step. Thus, the rotational motion of a single molecule cannot be attributed to a specific change in the current.

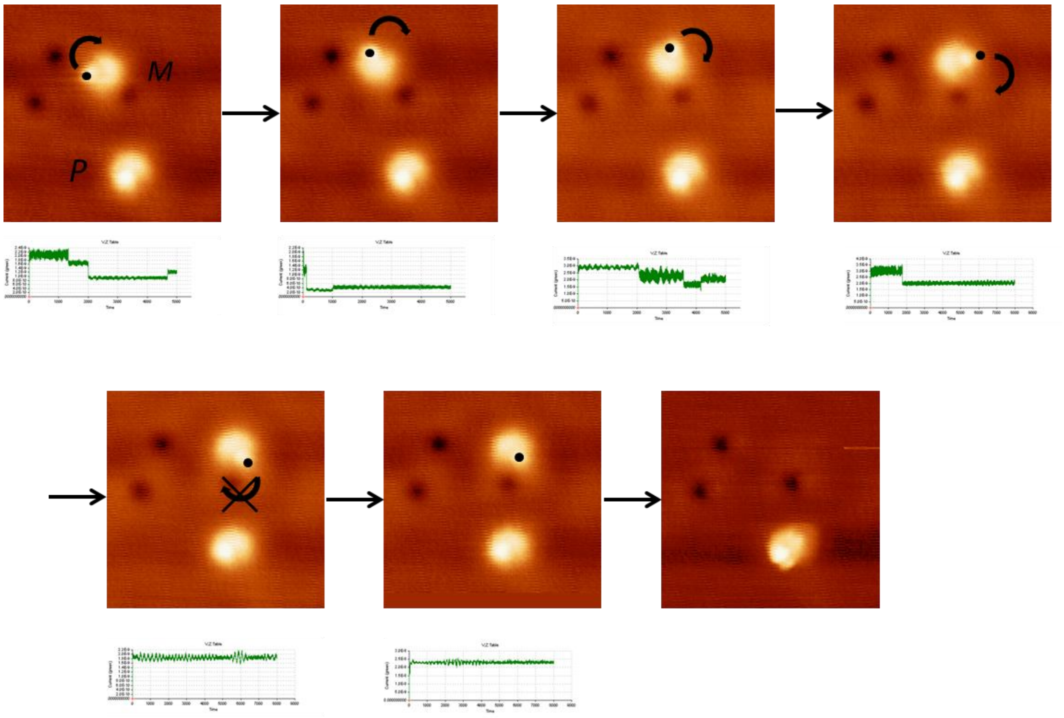

Fig. 8.4: Series of STM images taken subsequently after a manipulation event of *M*-[5]H. The tip position during the IET is marked by a black dot and the corresponding spectra obtained are placed under the image. The rotation direction of the molecule is indicated by a black arrow. The IET spectra were taken with an applied voltage of 400 mV over 5 seconds. (Measurement parameters: 6 nm x 6 nm, 82 mV, 32 pA)

8.3 Discussion

Compared to the single molecule measurements of [7]H in chapter 5.4, the chirality assignment of [5]H is more apparent with the distinct off-centered protrusion (Fig. 8.3). The reason therefore is likely the less pronounced helicity and the greater helix pitch of [5]H. The interplanar angles between both terminal benzene rings increases to 58.5° for [6]H and decreases significantly with further elongation after the first complete overlap of both terminal rings in [7]H (30.7°)[97].

The formation of homochiral dimers with the molecules rotated by 180° with respect to each other allows the best overlap between two molecules, i. e. of both upper terminal rings with the adverse molecule. Such an overlap is not possible for [7]H, where heterochiral dimers are formed. It is rather similar to the motive observed in the monolayer of db[5]H, where homochiral dimers are rotated by 180° with respect to each other (Fig. 6.4).

A rotational motion of molecules has been coupled to vibrational excitation for acetylene on Cu(100), where a reversible 90° rotation was the result of the excitation of the $C-H$ stretch mode[98,99]. The favorite rotational direction shown in Fig. 8.4 may be a result of vibrations of the helical backbone induced by the inelastically scattered tunneling electrons. However, further statistical analysis is required to confirm the observation. To exclude tip induced effects, opposite rotation directions for enantiomers should be observed with the same tip.

The less pronounced helicity compared to [7]H results in a lower racemization barrier, which is with 24.1 $\frac{kcal}{mol}$ (293 K)[21] only about half of the barrier for [7]H (41.7 $\frac{kcal}{mol}$, 300 K)[22]. This racemization barrier corresponds to an energy of 1.045 eV per molecule. Thus, with the applied voltage of up to 2.2 V, it was thought that the electrons should have enough energy to excite vibrations via IET that may lead to the switching of chirality. Since no switching in chirality was observed, the threshold energy for jumping or rotation is likely to be much lower than for a possible chirality switching. In the observed interconversion of enantiomeric states of propene adsorbed on Cu(211), the energy barrier for the chirality switching was also higher than for hopping or rotation, and yet only a change in the adsorption geometry was required for the switching[100].

A possibility to switch the chirality may be by performing the IET in a saturated monolayer, where the rotation or hopping of the molecule is hindered, similar to the *cis/trans* isomerization of an azobenzene on Au(111)[101]. Another possibility to switch the chirality could be similar experiments with [4]helicene. Both [4]helicene enantiomers should still be distinguishable in the STM image, but their racemization energy is much lower with estimated 3.5[102] to 7.6[103] $\frac{kcal}{mol}$.

9 Second Layer Formation of Heptahelicene

If the coverage was further increased compared to the first layer depositions of [7]H, the observed structures changed significantly. These structural changes in the second layers will be described and discussed in the following chapter.

All measurements in this chapter were performed with an Omicron Variable Temperature STM (see chapter 3.1.1). *Rac*-[7]H was evaporated from a Knudsen cell held at 160 °C, onto the respective crystal kept at RT. After deposition, the crystal was cooled with liquid helium to approximately 60 K during the measurements.

9.1 On Ag(111) and Au(111)

After the coverage of *rac*-[7]H on Ag(111) is increased above the monolayer, second layer islands start to from, while simultaneously the first layer structure disappears. At a coverage between the saturated monolayer and saturated second layer ($1.0 < \theta < 2.0$), the second layer islands are embedded in disordered areas and bright stripes are visible in the second layer (Fig. 9.1a). These stripes disappear in the saturated second layer and well-ordered domains extending over whole terraces are formed (Fig. 9.1b).

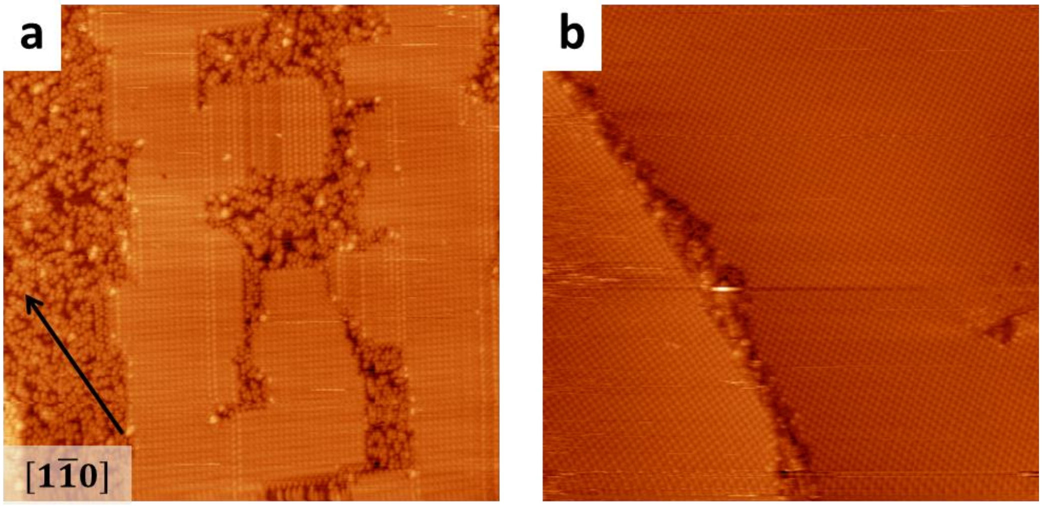

Fig. 9.1: **a**) STM image of *rac*-[7]H on Ag(111) showing the second layer growth, where only non-ordered areas in the first layer and the second layer islands are observed. In the second layer islands bright stripes are visible. **b**) STM image of the saturated second layer, where brighter stripes are not observed anymore. (Measurement parameters: 100 nm x 100 nm, **a**) -2.84 V, 28 pA; **b**) -2.78 V, 34 pA)

High resolution images show that the second layer consists of homochiral domains (Fig. 9.2). The absolute handedness of the molecules can be determined by going from bright to dark contrast within a single molecule as illustrated in Fig. 9.2 for two domains of opposite chirality. In contrast to the conglomerates of the monolayer of *rac*-[7]H on Cu(100) and *rac*-db[5]H, the mirror domains in the second layer of *rac*-[7]H on Ag(111) do not have opposite tilt angles with respect to the close-packed $[1\bar{1}0]$ surface direction. That is, the mirror domains run in opposite directions of the $[1\bar{1}0]$ surface direction, which leads to the observed angle of 60° (Fig. 9.2).

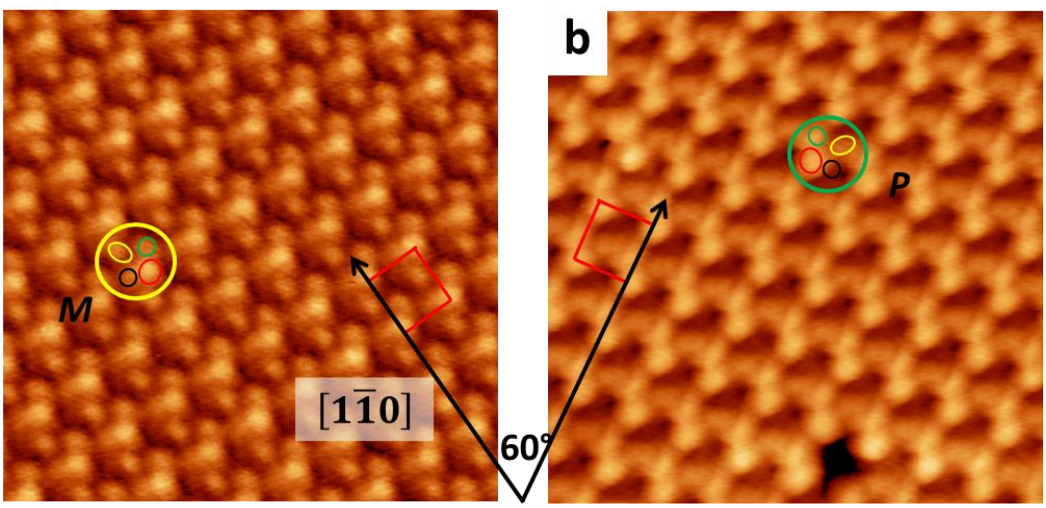

Fig. 9.2: High resolution STM images of the second layer structure on Ag(111). A single molecule appears as four protrusions. Going from bright to dark (red-green-yellow-black) allows the determination of the absolute helicity as illustrated for *M*-[7]H in **a** and *P*-[7]H in **b**. (Measurement parameters: 10 nm x 10 nm, **a**) -1.85 V, 28 pA; **b**) -2.18 V, 32 pA)

On Au(111) the second layer grows similar to Ag(111) and forms islands surrounded by non-ordered areas (Fig. 9.3a). Again, bright stripes are visible in the second layer islands. In contrast to Ag(111), these stripes do not disappear and are still present in the second layer at saturation coverage and have opposite oblique tilt angles with respect to the $[1\bar{1}0]$ surface direction. Due to the different directions of the brighter stripes, enantiomorphous domains can be clearly distinguished in the second layer on Au(111) (Fig. 9.3b). As on Ag(111), the domains in general extent over a whole terrace (Fig. 9.3b).

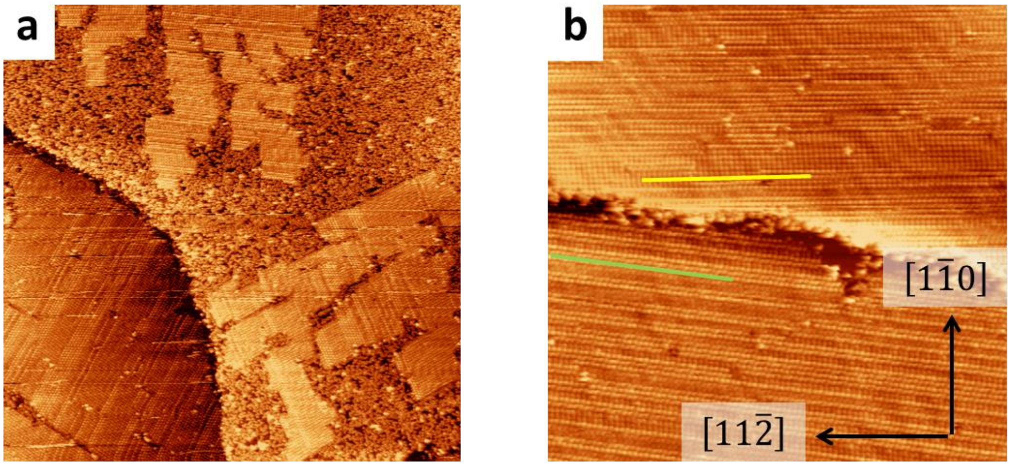

Fig. 9.3: a) Large area STM image showing the growing 2nd layer of *rac*-[7]H on Au(111) surrounded by non-ordered area. **b**) STM image of the saturated 2nd layer. Irregular dark and bright stripes are visible, which run in slightly different directions as indicated by the green and blue lines and have opposite oblique tilt angles with respect to the $[\mathbf{1\bar{1}0}]$ surface direction**.** The herringbone reconstruction of the Au(111) surface is still visible underneath the double layer of *rac*-[7]H. (Measurement parameters: **a**) 200 nm x 200 nm, 2.56 V, 10 pA; **b**) 100 nm x 100 nm, 2.73 V, 10 pA)

High resolution images show that the brighter appearing stripes originate from rows of molecules having the opposite handedness compared to the majority of molecules in the domain. This is illustrated with two enantiomorphous domains in Fig. 9.4. The domain in Fig. 9.4b consists mainly of *M*-[7]H and the domain in c of *P*-[7]H, respectively. Each domain contains rows of molecules with the opposite handedness that appear as brighter stripes in the long-range STM images. Additionally, there are molecular rows rotated by 180° (marked with black circles in Fig. 9.4). The unit cells of the enantiomorphous domains are slightly tilted in opposite directions with respect to the close-packed $[1\bar{1}0]$ surface direction (marked red in Fig. 9.4).

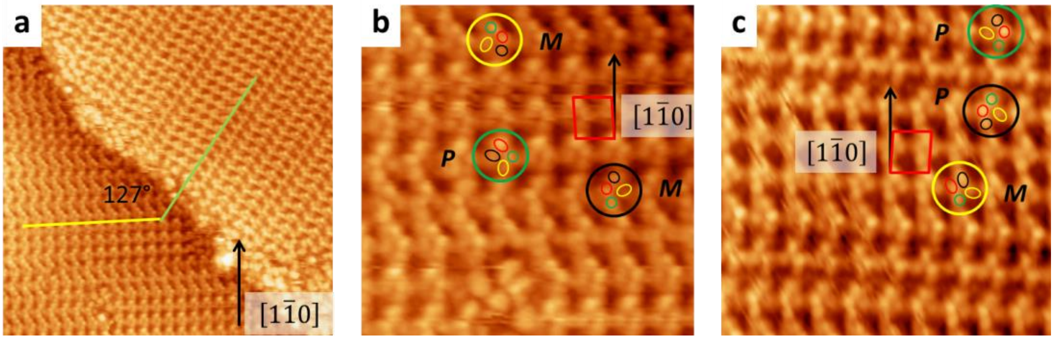

Fig. 9.4: **a**) STM image showing two domains on adjacent terraces that include an angle of 127°. The high-resolution images in **b** and **c** reveal that the unit cells of the two domains have opposite oblique tilt angles with respect to the close-packed $[\mathbf{1\bar{1}0}]$ surface direction and are thus enantiomorphous domains. A single molecule appears again as four protrusions and going from bright to dark (red-green-yellow-black) reveals that the domain in **b** consists mainly of *M*-[7]H and the one in **c** of *P*-[7]H. Moreover, there are complete rows of molecules of the same helicity rotated by 180° in each domain (black circle) as well as molecules of the opposite helicity. (Measurement parameters: **a**) 30 nm x 30 nm, 2.78 V, 10 pA; **b** and **c**) 10 nm x 10 nm, 2.78 V, 10 pA)

9.2 On Cu(100)

A large area STM image of the second layer of *rac*-[7]H on Cu(100) is shown in Fig. 9.5a. As on the (111) surfaces, the first layer structure is no longer present and only non-ordered areas are found between the ordered second layer structures (black circle). Similar to Au(111), bright stripes are visible in the saturated second layer. Due to the surface symmetry, the angle between rotational domains is 90° (yellow lines in Fig. 9.5b). Mirror domains include an angle of 50° and have opposite tilt angles with respect to the close-packed $[011]$ surface direction (green and yellow in Fig. 9.5b). In contrast to the second layer on Ag(111) and Au(111), domain boundaries are frequently observed on a single terrace on Cu(100).

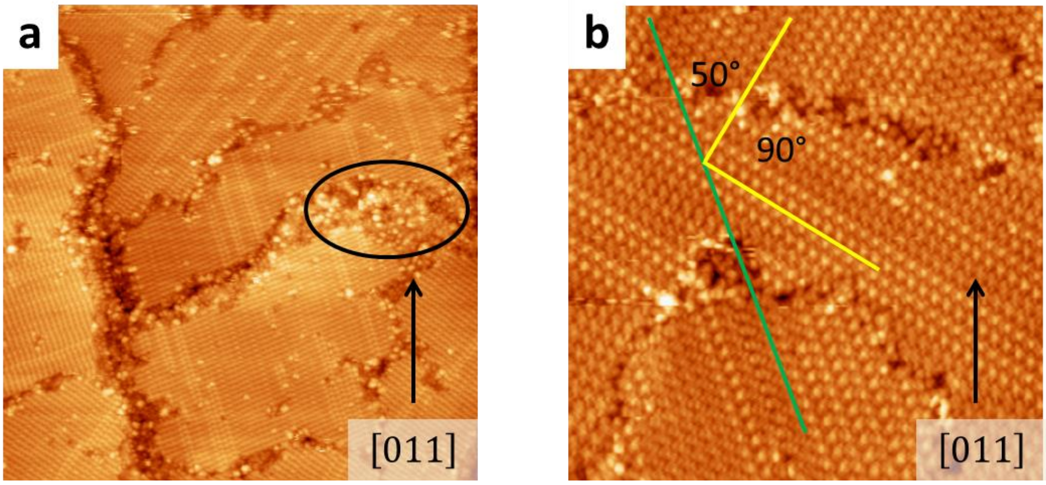

Fig. 9.5: **a**) Large area STM image of *rac*-[7]H on Cu(100). Within the ordered second layer some rows appear brighter. In non-ordered areas (black ellipse) the first layer quadruplet structure is not found. **b**) STM image showing two rotational domains (90° angle between yellow lines) and one enantiomorphous domain with a 50° with respect to the mirror domain (green line). (Measurement parameters: **a**) 100 nm x 100 nm, 2.56 V, 32 pA; **b**) 40 nm x 40 nm, -2.73 V, 24 pA)

High resolution images of two mirror domains show that the second layer is homochiral. The brighter stripes originate from rows of molecules that have the opposite handedness (Fig. 9.6). Each molecule appears as four protrusions and by going from bright to dark (black-red-green-yellow) the absolute helicity can be determined as illustrated in Fig. 9.6. The unit cells (marked red) have opposite oblique tilt angles of 25° with respect to the close-packed $[011]$ surface direction.

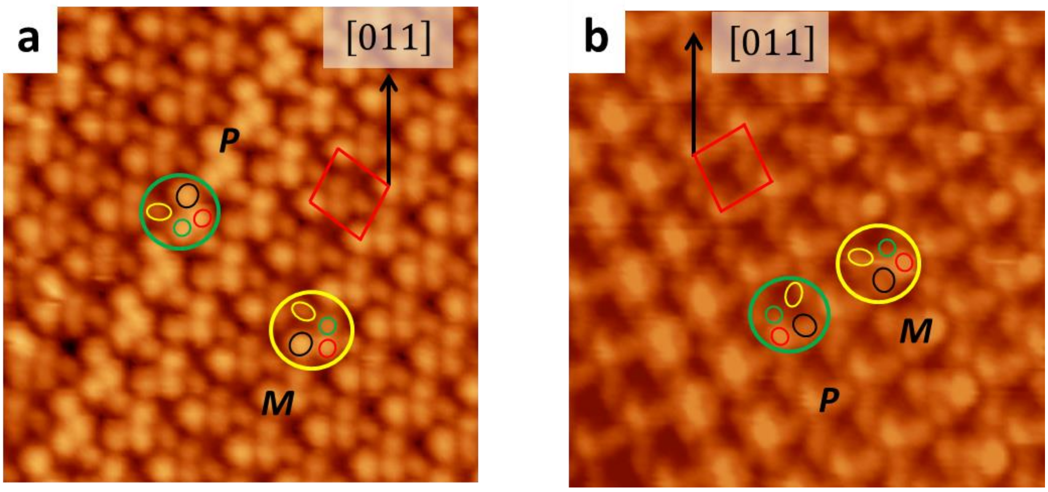

Fig. 9.6: High resolution STM images showing two mirror domains of *rac*-[7]H on Cu(100). Again, a single molecule appears as four protrusions. Going from bright to dark (black-red-green-yellow) reveals *M*-helicity for the domain shown in **a** and *P*-helicity for **b**. However, the brighter appearing row in **a** consists of the opposite *P*-[7]H. Rows with molecules of the opposite helicity are also present in the *P*-[7]H domain as illustrated in **b**. (Measurement parameters: 10 nm x 10 nm, **a**) -2.67 V, 35 pA; **b**) -2.67 V, 27pA)

Thus, the domain shown in Fig. 9.6a consists of *M*-[7]H in the second layer and the second layer of the domain in b of *P*-[7]H, respectively. An exception is the brighter appearing row in Fig. 9.6a, which consists of the opposite *P*-[7]H. In the domain shown in Fig. 9.6b there are also molecules of the “wrong” chirality and a different contrast.

9.3 Discussion

Overall, the second layer growth of *rac*-[7]H is very similar on all investigated surfaces, that is, second layer islands start to grow as soon as the coverage is increased above the saturated monolayer coverage. The areas between these islands exhibit reduced ordering (Cu(111)) or complete disorder (Au(111), Ag(111) and Cu(100)).

The mechanism of the observed second layer island growth and disorder in adjacent areas can be explained under the assumption that the critical temperature for the crystallization of the second layer is higher compared to the crystallization temperature of the racemic zigzag row structure[51].

During preparation at RT molecules have to be transferred into the second layer, as soon as the coverage is higher than in the saturated monolayer. Upon cooling, double layer islands start growing when their critical crystallization temperature is reached. Due to the progression in second layer growth there are no molecules left for further second layer formation, interlayer molecule-molecule interactions are no longer present and the first layer structure could start to form. However, due to the continuous cooling during second layer crystallization the mobility of the molecules in the first layer is too low for the formation of ordered domains, resulting in disorder in the remaining areas adjacent to the second layer islands. The first layer may be destabilized due to remaining second layer molecules and interlayer molecule-molecule interactions.

Interestingly, in contrast to the zigzag rows in the first layer, the unit cell of the second layer on Au(111) has an oblique tilt angle with respect to the close-packed $[1\bar{1}0]$ surface direction and exhibits enantiomorphism. Even though the unit cell vector is parallel to the close-packed $[1\bar{1}0]$ surface direction, the second layer on Ag(111) also exhibits enantiomorphism because of the opposite handedness of the molecules in the homochiral second layer structure. Thus, the chiral expression of *rac*-[7]H on Ag(111) and Au(111) changes with the second layer formation.

Due to the change from a racemic structure in the saturated monolayer and enantiopure domains in the second layer structure, the bottom layer has to have a different structure than the racemic zigzag rows in the monolayer. Moreover, the structures observed in the enantiopure monolayer can be excluded for the bottom layer, due to the lower density. Hence it is not possible to determine the bottom layer structure.

It should be noted that the possibility of tilted helicene molecules in the double layer, i. e. the molecules are not aligned with three benzene rings parallel to the surface as in the first layer, cannot be excluded. This kind of tilting has been observed in multilayer of pentacene on Cu(100)[104].

10 Second Layer of [5,6,9,10]-Dibenzopentahelicene

All measurements in this chapter were performed with an Omicron Variable Temperature STM (see chapter 3.1.1). *Rac*-db[5]H was evaporated from a Knudsen cell held at 170 °C, onto the Au(111) crystal kept at RT. After deposition, the crystal was cooled with liquid helium to approximately 60 K during the measurements.

The second layer of *rac*-db[5]H on Au(111) starts to grow in islands, but in contrast to the growth on *rac*-[7]H the first layer structure underneath is visible at the second layer boundaries (Fig. 10.1). Furthermore, the bottom layer structure differs significantly from the structure observed at coverages up to the saturated monolayer (chapter 6), that is, molecular zigzag rows are formed in the first layer. Enantiomorphous domains of these rows are shown in Fig. 10.1b and c and have opposite oblique tilt angles of $\pm 11.5°$ with respect to the close-packed $[1\bar{1}0]$ surface direction (green and yellow lines). The bottom layer zigzag rows have a different relative alignment every second row, so that the unit cell contains four molecules (marked blue in Fig. 10.1).

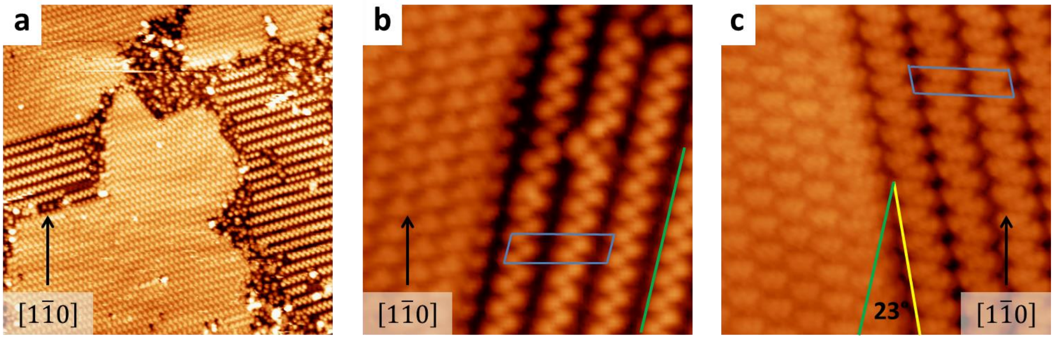

Fig. 10.1: **a**) STM image showing the second layer of *rac*-db[5]H on Au(111) and the zigzag row structure of the first layer underneath. **b** and **c**) Boundary between the first and second layer for two enantiomorphous domains. The enantiomorphous zigzag rows of the first layer include an angle of 23° or 11.5° with respect to the close-packed $[\mathbf{1\bar{1}0}]$ surface direction. (Measurement parameters: **a**) 70 nm x 70 nm, 2.84 V, 29 pA; **b**) 15 nm x 15 nm, 2.84 V, 29 pA; **c**) 15 nm x 15 nm, -2.18 V, 30 pA)

A large area STM image of the saturated second layer is shown in Fig. 10.2a. In this layer, several additional structures co-exist (see also Fig. 13.7). In Fig. 10.2b a boundary between two enantiomorphous domains is shown, where three rows of molecules with the helicity of the right domain align in the lattice of the left domain.

The molecules appear as five protrusions – with different contrasts in b and c – which allow the distinction of homochiral mirror domains. Additionally, in c there are two different alignments of molecules with the same chirality. A coexisting racemic structure shown in d is found on a few terraces (see also appendix Fig. 13.8). Unfortunately, no image with sufficient resolution to determine the absolute chirality of the molecules in the racemic structure was obtained. Of the structures observed at double layer coverage, the one shown in Fig. 10.2a is observed most frequently.

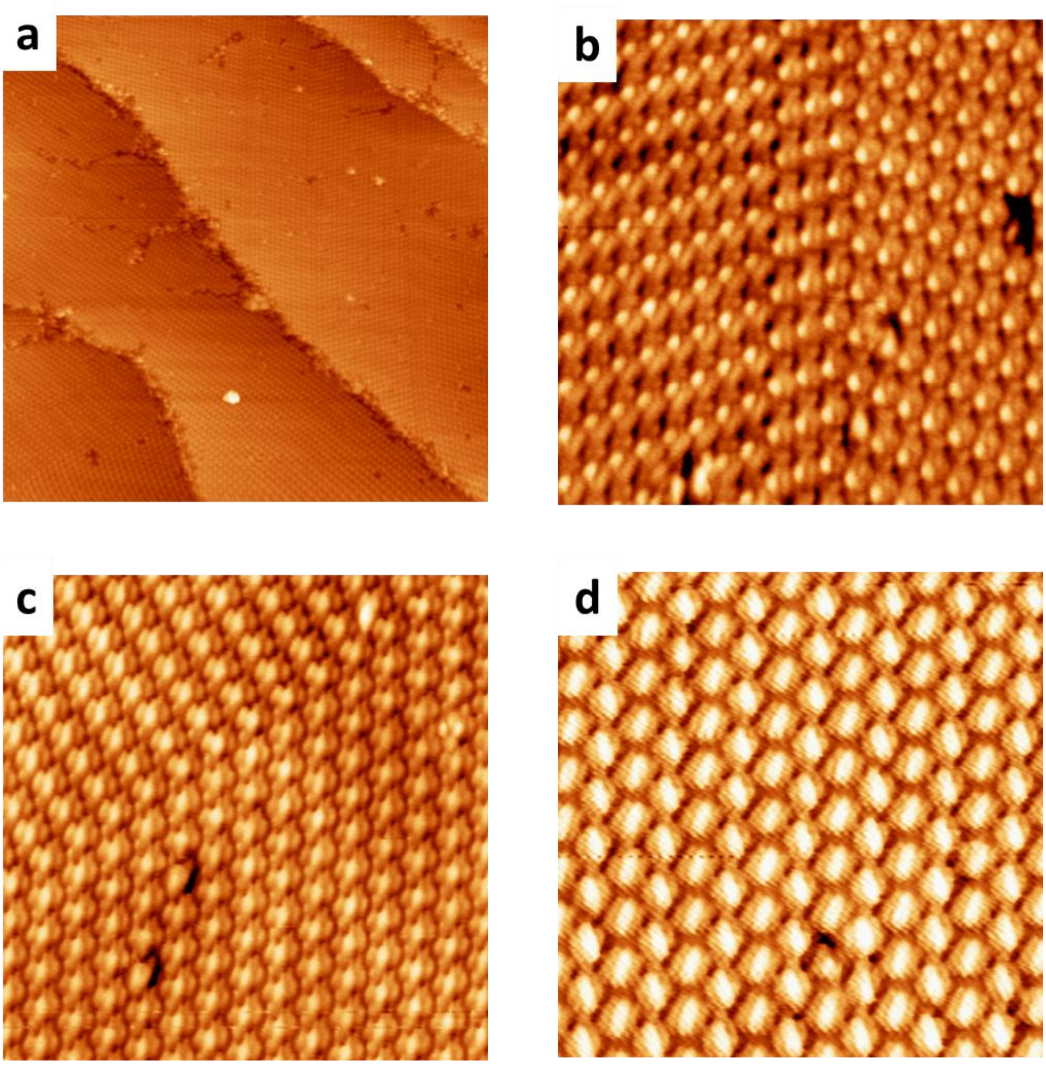

Fig. 10.2: **a**) Large area STM image of the saturated second layer. **b**) Mirror domain boundary in the second layer. **c**) Two different molecular alignments consisting of molecules of the same helicity. **d**) A coexisting racemic structure in the second layer. (Measurement parameters: **a**) 100 nm x 100 nm, 2.73 V, 23 pA; **b**) 20 nm x 20 nm, 1.89 V, 23 pA; **c**) 20 nm x 20 nm, 1.39 V, 26 pA, **d**) 20 nm x 20 nm, -2.05 V, 29 pA)

10.1 Discussion

The obtained STM images of the double layer growth of *rac*-db[5]H on Au(111) show that the second layer grows on top of a bottom layer. Thereby, the top and bottom layer have different structures, which is observed at boundaries of the incomplete top layer (Fig. 10.1). Additionally, in the double layer structure the bottom layer has a different structure compared to the monolayer. A similar structural change in the double layer compared to the monolayer was also assumed for the bottom layer of the *rac*-[7]H double layer, but the bottom layer did not extend sideways beyond the top layer. Both layers exhibit enantiomorphism (Fig. 10.1) and have homochiral composition. This was concluded from the high resolution images (Fig. 10.2a).

Unfortunately, the contrast in the STM images does not allow the unambiguous determination of the absolute handedness of the molecules in the bottom and top layer and the exact molecular alignment can only be determined in the top layer. The polymorphism in the saturated second layer (Fig. 10.2) further impedes the construction of a molecular model for the alignment of the molecules in the bottom and top layer. However, the top layer structure and possible molecular alignments in the bottom layer rows are shown in Fig. 10.3.

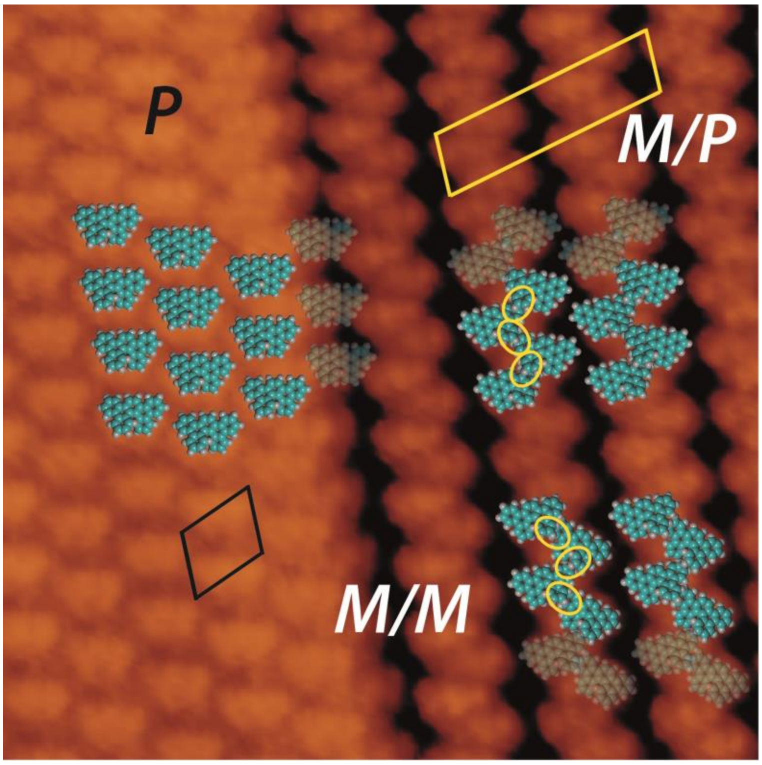

Fig. 10.3: Superposition of db[5]H space-fill models and an STM image at the second layer boundary showing possible molecular alignments. In the top layer the molecules have a hexagonal structure. In the bottom layer the molecules are aligned to slide over/under each other along a row (yellow ellipses). However, building a double row with the molecules along the row sliding over/under each

other is possible with a heterochiral (top *M*/*P* model) or homochiral (bottom *M*/*M* model) row. The top layer has a $\begin{pmatrix}\mathbf{5} & \mathbf{1}\\ \mathbf{0} & \mathbf{5}\end{pmatrix}$ unit cell containing one molecule (marked black) and the bottom layer a $\begin{pmatrix}\mathbf{5} & \mathbf{1}\\ \mathbf{0} & \mathbf{16}\end{pmatrix}$ unit cell with four molecules (marked yellow). (Measurement parameters: 15 nm x 15 nm, -2.18 V, 30 pA)

One reason for the lack of molecular resolution in the bottom layer may be a significant tilt of the molecular plane relative to the surface leading to the dark areas in the STM images. These dark areas are in particular problematic for building a molecular model and as shown in Fig. 10.3. Thus, a homochiral second layer consisting of *M*-db[5]H may grow on a bottom layer consisting of *M*-db[5]H, *P*-db[5]H or *rac*-db[5]H.

The unit cell of the top layer is $\begin{pmatrix}5 & 1\\ 0 & 5\end{pmatrix}$ and of the bottom layer $\begin{pmatrix}5 & 1\\ 0 & 16\end{pmatrix}$, which reveals different densities for the top and bottom layer. The density in the bottom layer (20 surface atoms per molecule) is comparable to the monolayer density (19.5 surface atoms per molecule), but is significantly reduced in the top layer (25 surface atoms per molecule). This is similar to the reduced density of the second layer of *rac*-[7]H on Cu(111) compared to the monolayer (see chapter 2.1.3). The short unit cell vector $\begin{pmatrix}5 & 1\end{pmatrix}$ is identical in the bottom and top layer and since there is no Moiré pattern, as observed in the double layer of enantiopure [7]H (Fig. 2.10), there should also be no lattice mismatch between both layers in the long unit cell vector direction despite the different densities. This may be explained by considering the bottom layer as “new” surface, which provides an adsorption grid that fits to the top layer structure.

The double layer growth can be explained similar than the structures of [7]H, i. e. with a higher crystallization temperature of the double layer compared the monolayer. The double layer than forms at that temperature, until there are not enough molecules left for double layer formation. In contrast to [7]H, the mobility of db[5]H molecules is still sufficient to order. Due to the boundary to the double layer, instead of the monolayer structure the zigzag row structure of the bottom layer is formed.

11 Summary and Outlook

On the investigated (111)-terminated surfaces racemic zigzag row structures were observed for [7]H. In contrast to Cu(111), no mirror domains were identified on Au(111) and Ag(111). There, the zigzag rows run along the highly symmetric $[1\bar{1}0]$ surface direction. On Cu(100) *rac*-[7]H separated into its enantiomers and formed a conglomerate with a molecular quadruplet as building blocks, that were already formed at low coverage. In summary, a significant influence of the substrate symmetry on the racemate or conglomerate formation in 2D crystallization of *rac*-[7]H has been observed. Moreover, conglomerate formation of non-functionalized helicenes was observed for the first time in the cases of *rac*-[7]H on Cu(100) as well as for *rac*-db[5]H on Au(111). To evaluate if the surface metal and symmetry dependence on the crystallization of helical molecules is limited to [7]H, the 2D racemate or conglomerate formation of db5[H], 5[H] or [6]H on (111) and (100) surfaces could be investigated including the effect of chiral doping. Moreover, the 2D crystallization of helicenes on (110) terminated surfaces has not been investigated so far.

A different situation was observed in the 2D crystallization on Ag(100), that is, at low coverage homochiral quadruplets were observed as on Cu(100), but with increasing coverage racemic zigzag rows started to form. The balance between the homochiral quadruplets and racemic zigzag rows shifted gradually towards the racemic rows with increasing coverage, until only zigzag rows were left in the saturated monolayer. This behavior may be explained by the relatively fast cooling of the sample, i. e. at higher coverage the enantiomers do not have the chance to separate and form a conglomerate before the crystallization temperature of the racemic zigzag rows is reached. First tempering experiments lead to non-ordered layers, likely due to an enantiomeric unbalanced layer. However, the exact crystallization temperature could not be determined by STM measurements, rendering the tempering experiments less promising. In further experiments the crystallization temperature should be determined, e. g. by low energy electron diffraction while slowly cooling the sample. Tempering at this temperature then may lead to conglomerate instead of racemate formation and thus supporting the presented theory.

In addition to *rac*-[7]H on Cu(100), conglomerate formation was observed for *rac*-db[5]H on Au(111). Doping with 26% enantiopure *M*-[7]H then lead a complete suppression of the *P*-db[5]H enantiomorph, whereby the balance between the *P*-db[5]H and *M*-db[5]H shifted gradually with an increasing *M*-[7]H content in the monolayer. These results show that dispersive forces can act in a similar manner compared to polar forces in diastereomeric chiral recognition at surfaces.

Furthermore, a change in the structures as soon as the coverage was increased above the saturated monolayer was observed, that is, *rac*-[7]H formed a homochiral second layer on all investigated surfaces. The double layers grew as islands with a significantly reduced ordering in the areas between the islands. In contrast to the racemic zigzag rows in the monolayer, the second layers on Au(111) and Ag(111) exhibited enantiomorphism. The double layer of *rac*-db[5]H on Au(111) also grew as islands with a homochiral second layer. In contrast to *rac*-[7]H the bottom layer structure extended beyond the double layer areas, showing a different structure in bottom layer compared to the monolayer. These structural changes in the double layer are explained by additional interlayer molecule-molecule interactions and a higher crystallization temperature of the double layer compared to the monolayer. Unfortunately, the exact structure and enantiomeric composition in the double layer of *rac*-db[5]H on Au(111) could not be determined. This may be possible with additional STM measurements to obtain high resolution images revealing the absolute helicity of single molecules.

Inelastic electron tunneling (IET) experiments of [5]H on Cu(111) did not lead to the expected switching of absolute handedness a single molecule. Instead, hopping and rotation of the molecules were observed with a preferred direction of the rotation for one enantiomer. However, for proving this preferred rotational hopping direction of [5]H on Cu(111) induced by IET, further measurements are required in order to provide solid statistical data and exclude tip effects. Switching the absolute helicity of a helicene molecule by IET may be possible by performing the IET at molecules in a saturated monolayer to prevent hoping and rotation, or by employing [4]helicene, which has a significantly lower racemization barrier.

Unfortunately, the exact structure and conformation of the 9,9'-bis[7]H molecules could not be determined explicitly. Therefore, additional simulations of the STM appearance are necessary, ideally accompanied by high-resolution AFM measurements.

12 References

(1) Pasteur, L. *Ann. Chim. Phys.* **1848**, *24*, 442.

(2) Cahn, R. S.; Ingold, C.; Prelog, V. *Angewandte Chemie* **1966**, *5*, 385.

(3) Siegel, J. S. *Chirality* **1998**, *10*, 24.

(4) Lemieux, R. P. *Acc. Chem. Res.* **2001**, *34*, 845.

(5) Kipping, F. S.; Pope, W. J. *J. Chem. Soc. Trans.* **1893**, *63*, 548.

(6) Sheldon, R. *Chiral Technologies: Industrial synthesis of optically active compounds*; M. Dekker: New York, 1993.

(7) Addadi, L.; Weiner, S. *Nature* **2001**, *411*, 753.

(8) Maddox, J. *Nature* **1989**, *341*, 101.

(9) Ernst, K.-H. In *Top. Curr. Chem.*; Springer Verlag: Heidelberg, 2006; Vol. 265, p 209.

(10) Ernst, K.-H. *physica status solidi b* **2012**, *249*, 2057.

(11) Wood, E. A. *J. Appl. Phys.* **1964**, *35*, 1306.

(12) Park, R. L.; Madden, H. H. *Surf. Sci.* **1968**, *11*, 188.

(13) Merz, L.; Ernst, K.-H. *Surf. Sci.* **2010**, *604*, 1049.

(14) Barlow, S.; Raval, R. *Curr. Opin. Colloid Interface Sci.* **2008**, *13*, 65.

(15) Barlow, S. M.; Raval, R. *Surf. Sci. Rep.* **2003**, *50*, 201.

(16) Raval, R. *Chem. Soc. Rev.* **2009**, *38*, 707.

(17) Ernst, K.-H. *Orig. Life Evol. Biosph.* **2010**, *40*, 41.

(18) Newman, M. S.; Lednicer, D. *J. Am. Chem. Soc.* **1956**, *78*, 4765.

(19) Martin, R. H. *Angewandte Chemie* **1974**, *13*, 649.

(20) Lightner, D. A.; Hefelfinger, D. T.; Frank, G. W.; Powers, T. W.; Trueblood, K. N. *Nat. Phys. Sci.* **1971**, *232*, 124.

(21) Goedicke, C.; Stegemeyer, H. *Tetrahedron Lett.* **1970**, 937.

(22) Martin, R. H.; Marchant, M. J. *Tetrahedron* **1974**, *30*, 347.

(23) Lindner, H. J. *Tetrahedron* **1975**, *31*, 281.

(24) Ermer, O.; Neudörfl, J. *Helv. Chim. Acta* **2001**, *84*, 1268.

(25) Brown, J. M.; Field, I. P.; Sidebottom, P. J. *Tetrahedron Lett.* **1981**, *22*, 4867.

(26) Lebon, F.; Longhi, G.; Gangemi, F.; Abbate, S.; Priess, J.; Juza, M.; Bazzini, C.; Caronna, T.; Mele, A. *J. Phys. Chem. A* **2004**, *108*, 11752.

(27) Botek, E.; Champagne, B. *J. Chem. Phys.* **2007**, *127*, 204101.

(28) Furche, F.; Ahlrichs, R.; Wachsmann, C.; Weber, E.; Sobanski, A.; Vögtle, F.; Grimme, S. *J. Am. Chem. Soc.* **2000**, *122*, 1717.

(29) Nuckolls, C.; Katz, T. J.; Verbiest, T.; van Elshocht, S.; Kuball, H.-G.; Kiesewalter, S.; Lovinger, A. J.; Persoons, A. *J. Am. Chem. Soc.* **1998**, *120*, 8656.

(30) Gingras, M. *Chem. Soc. Rev.* **2013**, *42*, 968.

(31) Shen, Y.; Chen, C. F. *Chem. Rev.* **2012**, *112*, 1463.

(32) Gingras, M. *Chem. Soc. Rev.* **2013**, *42*, 1051.

(33) Weitzenböck, R.; Lieb, H. *Monatsh. Chem.* **1913**, *33*, 549.

(34) Weitzenböck, R.; Klingler, A. *Monatsh. Chem.* **1918**, *39*, 315.

(35) Weitzenböck, R.; Klingler, A. *J. Chem. Soc.* **1918**, *114*, 494.

(36) Newman, M. S.; Lutz, W. B.; Lednicer, D. *J. Am. Chem. Soc.* **1955**, *77*, 3420.

(37) Flammand-Barbieux, M.; Nasielski, J.; Martin, R. H. *Tetrahedron Lett.* **1967**, *7*, 743.

(38) Liu, L. B.; Katz, T. J. *Tetrahedron Lett.* **1990**, *31*, 3983.

(39) Urbano, A. *Angewandte Chemie* **2003**, *42*, 3986.

(40) Gingras, M.; Felix, G.; Peresutti, R. *Chem. Soc. Rev.* **2013**, *42*, 1007.

(41) Ernst, K.-H.; Böhringer, M.; McFadden, C. F.; Hug, P.; Müller, U.; Ellerbeck, U. *Nanotechnology* **1999**, *10*, 355.

(42) Ernst, K.-H.; Kuster, Y.; Fasel, R.; McFadden, C. F.; Ellerbeck, U. *Surf. Sci.* **2003**, *530*, 195.

(43) Ernst, K.-H.; Neuber, M.; Grunze, M.; Ellerbeck, U. *J. Am. Chem. Soc.* **2001**, *123*, 493.

(44) Fasel, R.; Cossy, A.; Ernst, K. H.; Baumberger, F.; Greber, T.; Osterwalder, J. *J. Chem. Phys.* **2001**, *115*, 1020.

(45) Ernst, K.-H.; Kuster, Y.; Fasel, R.; Müller, M.; Ellerbeck, U. *Chirality* **2001**, *13*, 675.

(46) Ernst, K.-H.; Parschau, M.; Fasel, R. *e-J. Surf. Sci. Nanotech.* **2004**, *2*, 136.

(47) Parschau, M.; Fasel, R.; Ernst, K.-H. *Crys. Growth & Des.* **2008**, *8*, 1890.

(48) Fasel, R.; Parschau, M.; Ernst, K. H. *Nature* **2006**, *439*, 449.

(49) Fasel, R.; Parschau, M.; Ernst, K. H. *Angewandte Chemie* **2003**, *42*, 5178.

(50) Parschau, M.; Ellerbeck, U.; Ernst, K.-H. *Colloids Surf. A: Physicochem. Eng. Aspects* **2010**, *354*, 240.

(51) Parschau, M.; Ernst, K.-H. *unpublished data*.

(52) Stohr, M.; Boz, S.; Schar, M.; Nguyen, M. T.; Pignedoli, C. A.; Passerone, D.; Schweizer, W. B.; Thilgen, C.; Jung, T. A.; Diederich, F. *Angewandte Chemie* **2011**, *50*, 9982.

(53) Rahe, P.; Nimmrich, M.; Greuling, A.; Schütte, J.; Stara, I. G.; Rybáček, J.; Huerta-Angeles, G.; Stary, I.; Rohlfing, M.; Kühnle, A. *J. Phys. Chem. C* **2010**, *114*, 1547.

(54) Rybáček, J.; Huerta-Angeles, G.; Kollárovič, A.; Stará, I. G.; Starý, I.; Rahe, P.; Nimmrich, M.; Kühnle, A. *Eur. J. Org. Chem.* **2011**, *2011*, 853.

(55) Hauke, C. M.; Rahe, P.; Nimmrich, M.; Schütte, J.; Kittelmann, M.; Stará, I. G.; Starý, I.; Rybáček, J.; Kühnle, A. *J. Phys. Chem. C* **2012**, *116*, 4637.

(56) Goretta, S.; Tasciotti, C.; Mathieu, S.; Smet, M.; Maes, W.; Chabre, Y. M.; Dehaen, W.; Giasson, R.; Raimundo, J.-M.; Henry, C. R.; Barth, C.; Gingras, M. *Org. Lett.* **2009**, *11*, 3846.

(57) Barth, C.; Henry, C. R. *New J. Phys.* **2009**, *11*, 043003.

(58) Suzuki, K. *J. Phys. Soc. Jpn.* **1961**, *16*, 67.

(59) Barth, C.; Gingras, M.; Foster, A. S.; Gulans, A.; Felix, G.; Hynninen, T.; Peresutti, R.; Henry, C. R. *Adv. Mater.* **2012**, *24*, 3228.

(60) Balandina, T.; van der Meijden, M. W.; Ivasenko, O.; Cornil, D.; Cornil, J.; Lazzaroni, R.; Kellogg, R. M.; De Feyter, S. *Chem. Commun.* **2013**, *49*, 2207.

(61) Prauzner-Bechcicki, J. S.; Godlewski, S.; Budzioch, J.; Goryl, G.; Walczak, L.; Sehnal, P.; Stara, I. G.; Stary, I.; Ample, F.; Joachim, C.; Szymonski, M. *Chemphyschem : a European journal of chemical physics and physical chemistry* **2010**, *11*, 3522.

(62) Godlewski, S.; Prauzner-Bechcicki, J. S.; Budzioch, J.; Walczak, L.; Stará, I. G.; Starý, I.; Sehnal, P.; Szymonski, M. *Surface Science* **2012**, *606*, 1600.

(63) Taniguchi, M.; Nakagawa, H.; Yamagishi, A.; Yamada, K. *Surface Science* **2000**, *454*, 1005.

(64) Taniguchi, M.; Nakagawa, H.; Yamagishi, A.; Yamada, K. *Surface Science* **2002**, *507*, 458.

(65) Taniguchi, M.; Nakagawa, H.; Yamagishi, A.; Yamada, K. *J. Mol. Catal. A Chem.* **2003**, *199*, 65.

(66) Binnig, G.; Rohrer, H. *Rev. Mod. Phys.* **1987**, *59*, 615.

(67) Binnig, G.; Rohrer, H.; Gerber, C.; Weibel, E. *Appl. Phys. Lett.* **1982**, *40*, 178.

(68) Binnig, G.; Rohrer, H.; Gerber, C.; Weibel, E. *Phys. Rev. Lett.* **1982**, *49*, 57.

(69) Binnig, G.; Rohrer, H.; Gerber, C.; Weibel, E. *Phys. Rev. Lett.* **1983**, *50*, 120.

(70) Chen, C. *Introduction to Scanning Tunneling Microscopy*; Oxford University Press: Oxford, 2008.

(71) Wiesendanger, R. *Scanning Probe Microscopy and Spectroscopy*; Cambridge University Press: Cambridge, 1994.

(72) Mayne, A. J. *Atomic and Molecular Manipulation*; Elsevier Science: Oxford, 2011; Vol. 2.

(73) Morgenstern, K.; Lorente, N.; Rieder, K.-H. *physica status solidi (b)* **2013**, *250*, 1671.

(74) Horcas, I.; Fernàndez, R.; Gòmez-Rodrìgez, J. M.; Colchero, J.; Gòmez-Herrero, J.; Baro, A. M. *Rev. Sci. Instr.* **2007**, *78*, 013705.

(75) Böhringer, M.; Schneider, W.-D.; Berndt, R. *Angewandte Chemie* **2000**, *39*, 792.

(76) Vidal, F.; Delvigne, E.; Stepanow, S.; Lin, N.; Barth, J. V.; Kern, K. *J. Am. Chem. Soc.* **2005**, *127*, 10101.

(77) Gopakumar, T. G.; Matino, F.; Schwager, B.; Bannwarth, A.; Tuczek, F.; Kröger, J.; Berndt, R. *J. Phys. Chem. C* **2010**, *114*, 18247.

(78) Barth, J.; Brune, H.; Ertl, G.; Behm, R. *Physical Review B* **1990**, *42*, 9307.

(79) Ernst, K.-H.; Baumann, S.; Lutz, C. P.; Seibel, J.; Zoppi, L.; Heinrich, A. J. *manuscript in preparation*.

(80) Kuzmenko, I.; Weissbuch, I.; Gurovich, E.; Leiserowitz, L.; Lahav, M. *Chirality* **1998**, *10*, 415.

(81) Green, M. M.; Reidy, M. P.; Johnson, R. J.; Darling, G.; O'Leary, D. J.; Wilson, G. *J. Am. Chem. Soc.* **1989**, *111*, 6452.

(82) Green, M. M.; Garetz, B. A.; Munoz, B.; Chang, H.; Hoke, S.; Cooks, R. G. *J. Am. Chem. Soc.* **1995**, *117*, 4181.

(83) Humblot, V.; Ortega Lorenzo, M.; Baddeley, C. J.; Haq, S.; Raval, R. *J. Am. Chem. Soc.* **2004**, *126*, 6460.

(84) Parschau, M.; Behzadi, B.; Romer, S.; Ernst, K.-H. *Surf. Interface Anal.* **2006**, *38*, 1607.

(85) Barbosa, L. A. M. M.; Sautet, P. *J. Am. Chem. Soc.* **2001**, *123*, 6639.

(86) Parschau, M.; Behzadi, B.; Romer, S.; Ernst, K.-H. *J. Am. Chem. Soc.* **2004**, *126*, 15398.

(87) Parschau, M.; Kampen, T.; Ernst, K.-H. *Chem. Phys. Lett.* **2005**, *407*, 433.

(88) Fasel, R.; Wider, J.; Quitmann, C.; Ernst, K. H.; Greber, T. *Angewandte Chemie* **2004**, *43*, 2853.

(89) Roth, C.; Passerone, D.; Ernst, K. H. *Chem. Commun.* **2010**, *46*, 8645.

(90) Haq, S.; Liu, N.; Humblot, V.; Jansen, A. P. J.; Raval, R. *Nat. Chem.* **2009**, *1*, 409.

(91) Chen, Q.; Richardson, N. V. *Nat. Mater.* **2003**, *2*, 324.

(92) Blankenburg, S.; Schmidt, W. *Phys. Rev. Lett.* **2007**, *99*.

(93) Roth, C.; Parschau, M.; Ernst, K. H. *Chemphyschem : a European journal of chemical physics and physical chemistry* **2011**, *12*, 1572.

(94) Roth, C.; Passerone, D.; Merz, L.; Parschau, M.; Ernst, K.-H. *J. Phys. Chem. C* **2011**, *115*, 1240.

(95) Mhatre, B. S.; Pushkarev, V.; Holsclaw, B.; Lawton, T. J.; Sykes, E. C. H.; Gellman, A. J. *J. Phys. Chem. C* **2013**, *117*, 7577.

(96) Amemiya, R.; Yamaguchi, M. *Organic & biomolecular chemistry* **2008**, *6*, 26.

(97) Laarhoven, W. H.; Prinsen, W. J. C. *Top. Curr. Chem.* **1984**, *125*, 63.

(98) Stipe, B. C.; Rezaei, M. A.; Ho, W. *Phys. Rev. Lett.* **1998**, *81*, 1263.

(99) Stipe, B. C. *Science* **1998**, *280*, 1732.

(100) Parschau, M.; Passerone, D.; Rieder, K. H.; Hug, H. J.; Ernst, K. H. *Angew. Chem. Int. Ed. Engl.* **2009**, *48*, 4065.

(101) Alemani, M.; Peters, M. V.; Hecht, S.; Rieder, K.-H.; Moresco, F.; Grill, L. *J. Am. Chem. Soc.* **2006**, *128*, 14446.

(102) Janke, R. H.; Haufe, G.; Würthwein, E.-U.; Borkent, J. H. *J. Am. Chem. Soc.* **1996**, *118*, 6031.

(103) Grimme, S.; Peyerimhoff *Chem. Phys.* **1996**, *204*, 411.

(104) Satta, M.; Iacobucci, S.; Larciprete, R. *Phys. Rev. B* **2007**, *75*.

(105) Sudhakar, A.; Katz, T. J. *Tetrahedron Lett.* **1986**, *27*, 2231.

(106) Wittig, G.; Geissler, G. *Liebigs Ann. Chem.* **1953**, *580*, 44.

(107) Mallory, F. B.; Mallory, C. W. *Org. React.* **1984**, *30*, 1.

(108) Miyaura, N.; Suzuki, A. *J.C S. Chem. Commun.* **1979**, 866.

(109) Allemann, O.; Duttwyler, S.; Romanato, P.; Baldridge, K. K.; Siegel, J. S. *Science* **2011**, *332*, 574.

13 Appendix

Heptahelicene

Racemic 9-bromo-[7]H was prepared photochemically according to route developed by Katz and coworkers[105] shown in **Scheme 13.1**. and used for the synthesis of bisheptahelicene.

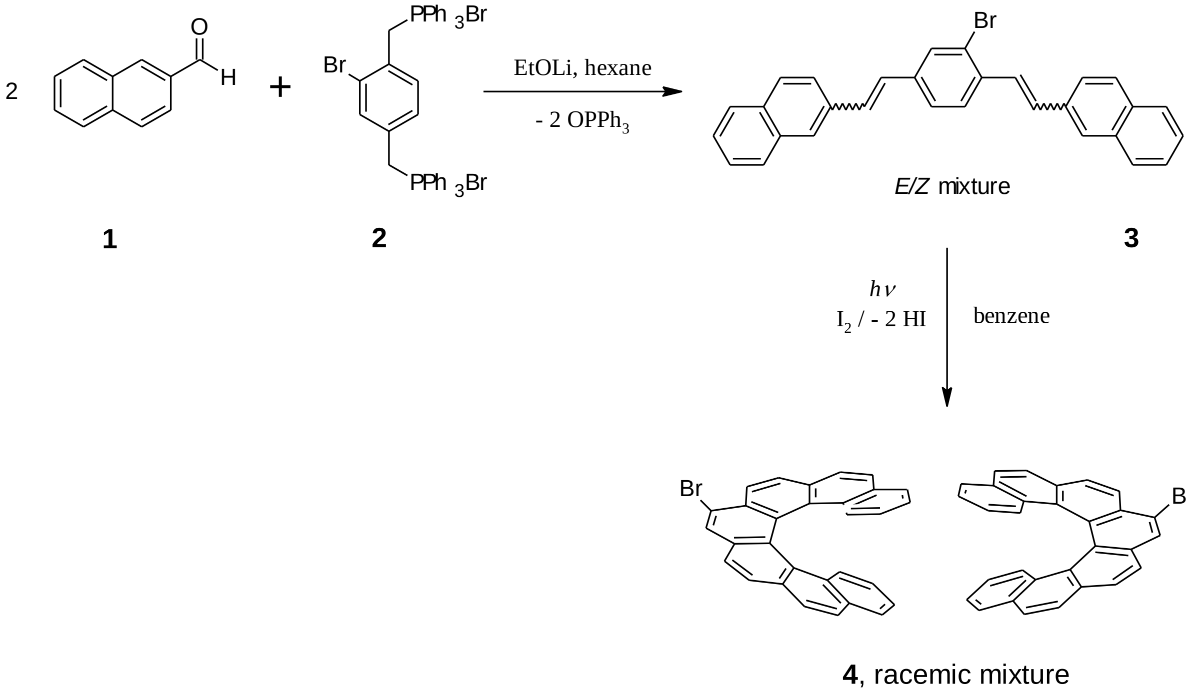

Scheme 13.1: Photochemical synthesis *rac*-heptahelicene.

The synthesis of *rac*-[7]H started with 2-naphtaldehyde (**1**) and [2-bromo-4-[(triphenyl)methyl]benzyl](triphenyl)phosphonium dibromide (**2**). A possible synthesis for these precursors is presented in the appendix Scheme 13.4. The bisphisphonium salt **2** was subjected to a Wittig reaction[106] with **1** to give an *E/Z* mixture of **3**. The helix was then formed by two photocyclizations[107] with iodine as oxidant giving a racemic mixture of bromide-substituted [7]H (**4**). In this step the bromine has a directive effect, thus increasing the yield and preventing possible side reactions[105].

Bisheptahelicene

The Bisheptahelicenes were synthesized in the group of Prof. Dr. Terfort at the University of Frankfurt. The synthetic route is shown in **Scheme 13.2**.

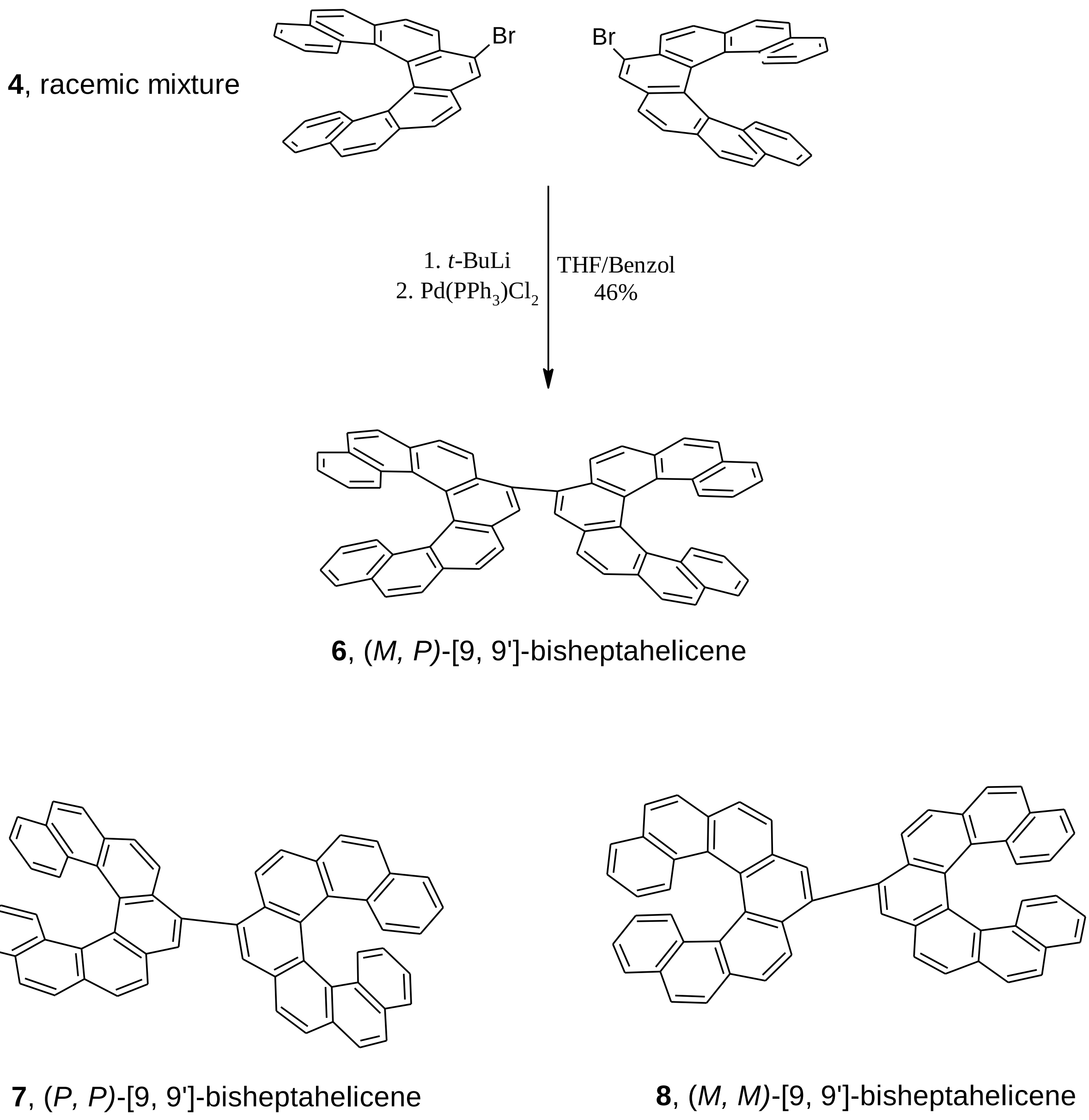

4, racemic mixture

6, (*M, P)*-[9, 9']-bisheptahelicene

7, (*P, P)*-[9, 9']-bisheptahelicene

8, (*M, M)*-[9, 9']-bisheptahelicene

Scheme 13.2: Synthesis of [9, 9′]-bisheptahelicene.

A racemic mixture of 9-bromoheptahelicene (**4**) was prepared as described in the previous chapter. Instead of removing the bromide substituent, two random helicenes were coupled by a Suzuki coupling[108], which resulted in a mixture of the *meso* compound (*M, P*)-[9, 9']-bisheptahelicene (**6**) and the chiral (*P, P*)-[9, 9']-bisheptahelicene (**7**) and (*M, M*)-[9, 9']-bisheptahelicene (**8**).

[5,6,9,10]-Dibenzopentahelicene

Racemic db[5]H was synthesized by Oliver Allemann in the group of Prof. Dr. Jay S. Siegel at the University of Zürich. The synthesis is shown in the following **Scheme 13.3**.

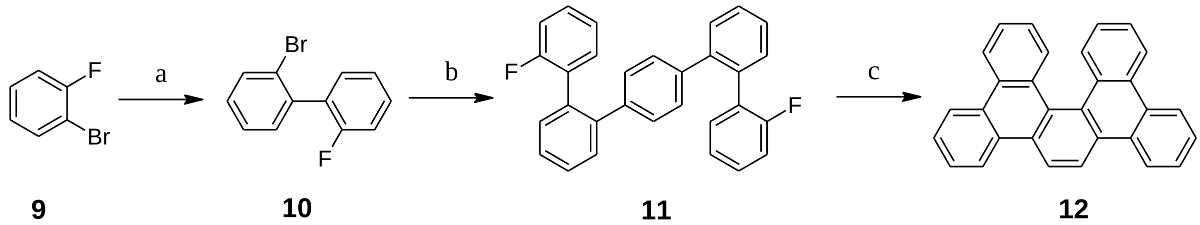

a) 1. *n*BuLi, THF, -78 °C, 2. $ZnCl_2$, 3. $Pd(PPh_3)_4$, 1-bromo-2-iodobenzene, 50 °C, 12 h, 90%

b) 1. *n*BuLi, THF, -78 °C, 2. $ZnCl_2$, 3. PEPPSI-*i*Pr, 1,4-diiodobenzene, 70 °C, 13 h, 61%

c) [*i*PrSi][$CHB_{11}H_5Cl_6$], Me_2SiMes_2, PhCl, 110 °C, 8 h, 67%

Scheme 13.3: Synthesis of [5,6,9,10]-dibenzopentahelicene.

2-bromo-2'-fluorobiphenyl (**10**) was prepared via a Negishi cross coupling between 1-bromo-2-fluorobenzene (**9**) and 1-bromo-2-iodobenzene. Consecutive Negishi cross couplings of **10** with 1,4-diiodobenzene gave difluoroquinquephenyl (**11**). The last step was an intramolecular Friedel-Crafts type arylation of **11** using silylium ion promoted C-F bond activation[109], which gave [5,6,9,10]-dibenzopentahelicene (**4**).

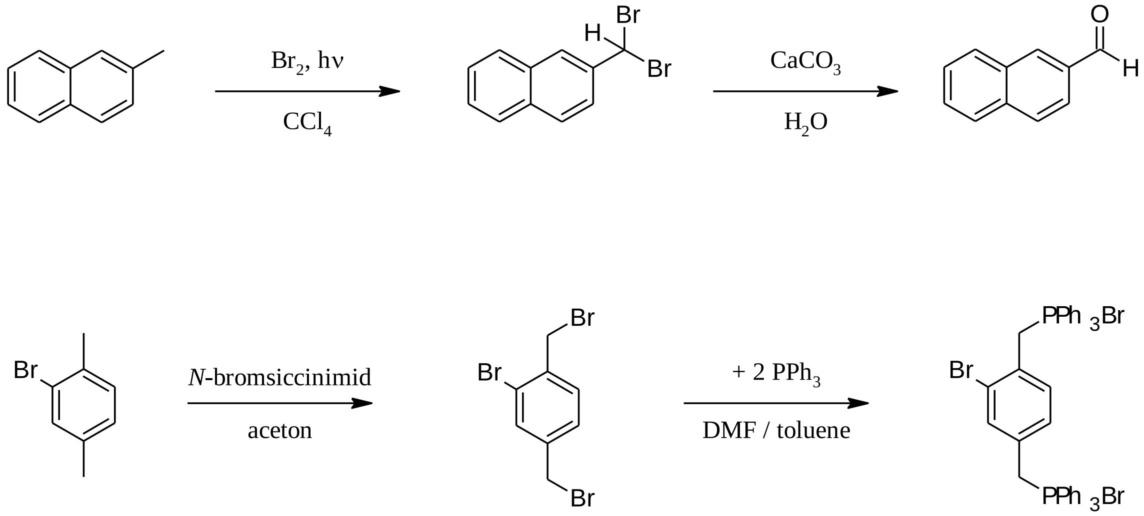

Scheme 13.4: Synthesis of the precursors required for the helicene synthesis described above.

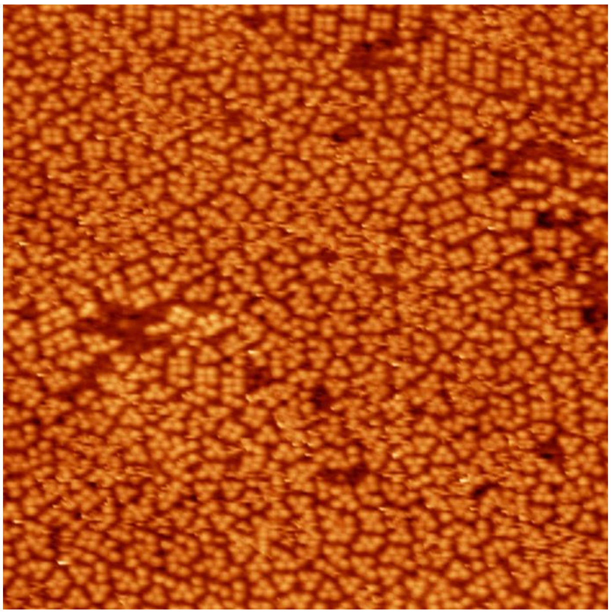

Fig. 13.1: STM image of *M*-[7H] with features of the γ and δ phase on Au(111) at a coverage of θ = 0.98. (Measurement parameters: 46 nm x 46 nm, -2.725 V, 35 pA)

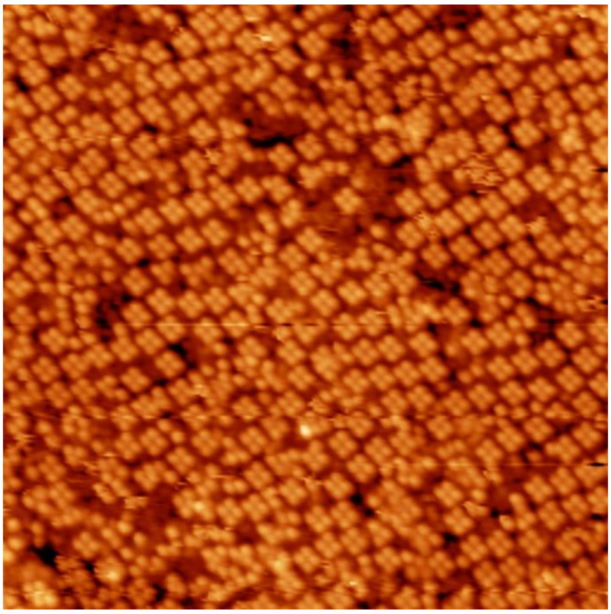

Fig. 13.2: STM image of *M*-[7H] on Cu(100) at θ = 0.8. Quadruplets are already formed, but not ordered. (Measurement parameters: 50 nm x 50 nm, -2.73 V, 37 pA)

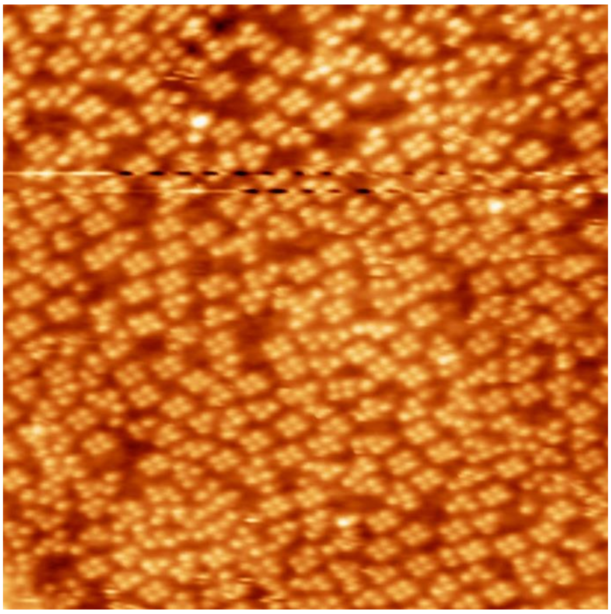

Fig. 13.3: STM image of *M*-[7H] on Cu(100) at θ = 0.8. Cluster of four molecules are formed, but not ordered yet. (Measurement parameters: 40 nm x 40 nm, -2.73 V, 31 pA)

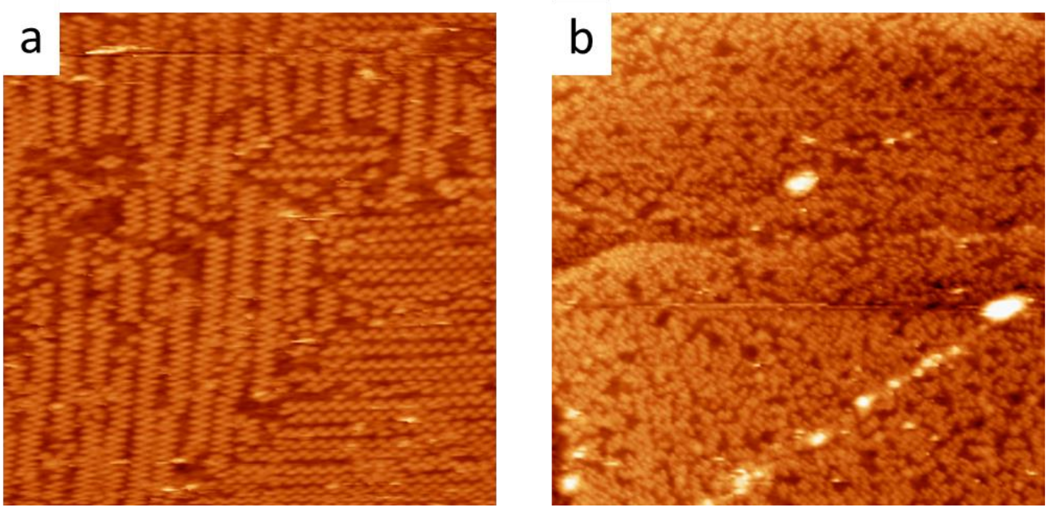

Fig. 13.4: STM images or *rac*-[7]H on Ag(100) after fast cooling from RT (**a**) and after heating the once cooled sample to 200 K, keeping it at that temperature for a few minutes and slowly cooling down again (**b**). In the image after slow cooldown the ordering in the monolayer is significantly reduced. (Measurement parameters: **a**) 40 nm x 40 nm, -2.73 V, 10 pA, **b**) 80 nm x 80 nm, 2.84 V, 21 pA)

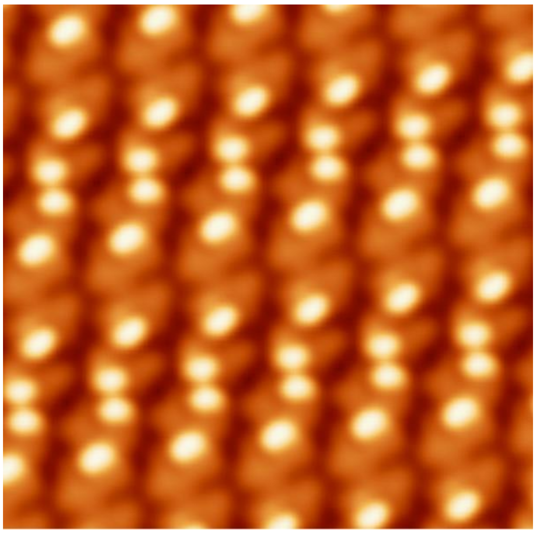

Fig. 13.5: High resolution image obtained by averaging over several unit cells. (Measurement parameters: 9 nm x 9 nm, 2.05 V, 28 pA)

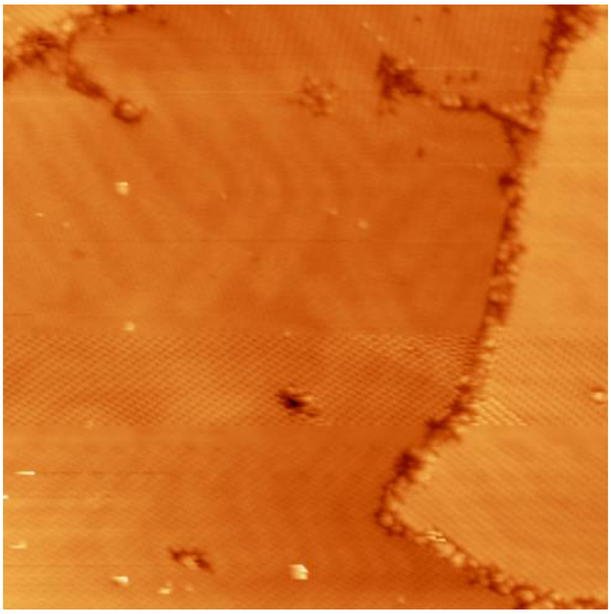

Fig. 13.6: STM image showing the saturated second layer of *rac*-db[5]H on Au(111) with the herringbone reconstruction still visible underneath. (Measurement parameters: 100 nm x 100 nm, -2.78 V, 24 pA)

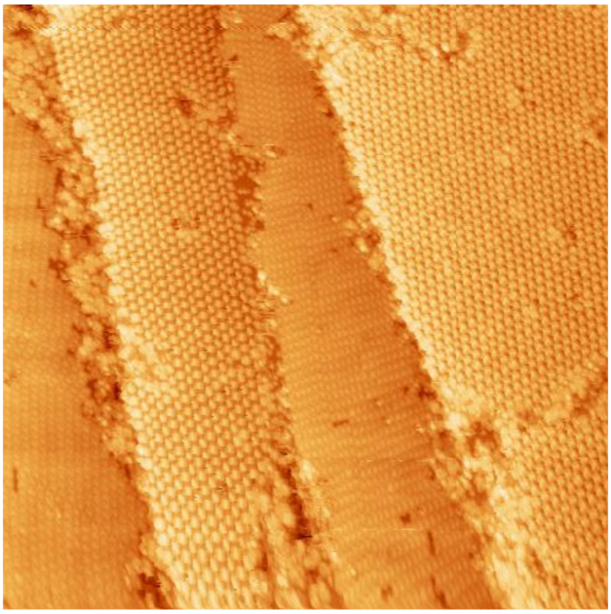

Fig. 13.7: STM image showing racemic and enantiopure structures in the second layer of *rac*-db[5]H on Au(111) co-existing on adjacent terraces. (Measurement parameters: 100 nm x 100 nm, -2.13 V, 88 pA)

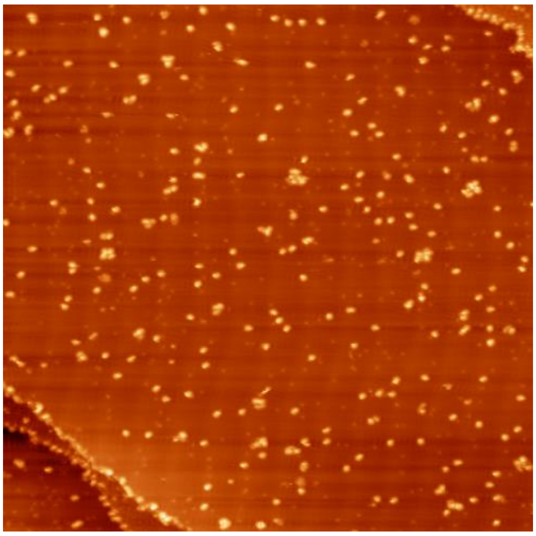

Fig. 13.8: Large area STM image of [5]H on Cu(111) at low coverage. Single molecules are located at the step edges, mostly isolated on the flat terrace and in some cases aggregated in small clusters. (Measurement parameters: 100 nm x 100 nm, 1.914 V, 69 pA)

14 List of Publications

(1) Johannes Seibel, Tobias Weidner and Ulrich Siemeling, Di(thienyl)ethene – substituted subphthalocyanine derivatives for switchable, self-assembled monolayers on gold surfaces, Poster, SAOG Meeting, 28.01.2011, Fribourg

(2) Tobias Weidner, Joe E. Baio, Johannes Seibel and Ulrich Siemeling, Dithienylcyclopentene-functionalised subphthalocyaninatoboron complexes: Photochromism, luminescence modulation and formation of self-assembled monolayers on gold, *Dalton Trans.* **2012**, 41, 1553-1561

(3) Johannes Seibel and Karl-Heinz Ernst, Differences in Chiral Expression: Racemic and Enantiopure Heptahelicenes on Various Metal Surfaces, Poster, Annual Meeting of the Swiss Physical Society, 21.-22. 6. 2012, ETH Zürich

(4) Johannes Seibel and Karl-Heinz Ernst, Differences in Chiral Expression: Racemic and Enantiopure Heptahelicenes on Various Metal Surfaces, Poster, SAOG Meeting, 25.01.2013, Fribourg

(5) Johannes Seibel, Laura Zoppi, Manfred Parschau and Karl-Heinz Ernst, Differences in Chiral Expression: Racemic and Enantiopure Heptahelicenes on Various Metal Surfaces, Talk, DPG-Frühjahrstagung der Sektion Kondensierte Materie, 10.-15. 03. 2013, University of Regensburg

(6) Johannes Seibel, Oliver Allemann, Jay S. Siegel and Karl-Heinz Ernst, Chiral conflict among different helicenes suppresses formation of one enantiomorph in 2D crystallization, Poster, Empa PhD Students Symposium, 23.11.2013, Empa Dübendorf

(7) Johannes Seibel, Oliver Allemann, Jay S. Siegel and Karl-Heinz Ernst, Chiral conflict among different helicenes suppresses formation of one enantiomorph in 2D crystallization, *J. Am. Chem. Soc.* **2013**, *135*, 7434–7437; DOI: 10.1021/ja402012j

(8) Johannes Seibel, Laura Zoppi, Manfred Parschau and Karl-Heinz Ernst, Surface symmetry rules over 2D racemate or conglomerate crystallization, *manuscript in preparation*

(9) Karl-Heinz Ernst, Susanne Baumann, Christopher P. Lutz, Johannes Seibel, Laura Zoppi and Andreas J. Heinrich*,* Single molecule manipulation reveals chiral recognition in van der Waals dimers, *manuscript in preparation*

15 Curriculum Vitae

First and Last Name: Johannes Seibel
Address: Am Stadtrand 31
8600 Dübendorf, Switzerland
Nationality: German
Date and Place of Birth: 01.10.1984, Bad Wildungen, Germany

School: Gustav Stresemann Gymnasium, Bad Wildungen
[2001-2004] Degree: Abitur

Civil Service Asklepios Kliniken Bad Wildungen
[2004-2005]

Academic Studies: University of Kassel
[2005-2010] Nanostructure and Molecular Sciences
Diploma Thesis: "Di(thienyl)ethen-substituierte Subphthalocyaninderivate für schaltbare, selbstassemblierende Monolagen auf Goldoberflächen" in the group of Prof. Dr. Ulrich Siemeling
Degree: Diplom Nanostrukturwissenschaftler

Doctoral Studies: Empa, Swiss Federal Institute for Materials Science and Technology,
[From 2011] 8600 Dübendorf, Switzerland
Molecular Surface Science Group, Supervisor: Prof. Dr. Karl-Heinz Ernst

16 Acknowledgements

Many people contributed considerably to the success of this thesis, be it professionally or personally. I would like to thank all of them.

First and foremost I would like to thank my family for their support and always being there for me.

I thank my supervisor Karl-Heinz Ernst for making this thesis possible and providing the equipment and environment for professional science. I want to thank Manfred Parschau for always having an open ear and helping with various problems anytime it was needed. Chrysanthi Karageorgaki, Quirin Stöckl, Andreas Bliersbach and Johannes Schwenk have my thanks for accompanying me on our mutual journey and making it a fun one. I thank Frank Pilger for joining me on my adventure in Switzerland and proofreading.

My thanks go to our collaborators, the groups of Jay S. Siegel at the University of Zürich and Andreas Terfort at the University of Frankfurt for the synthesis of the various helicene derivatives as well as Laura Zoppi for the calculations of the STM appearances.

Last but not least I thank all members of the Lab 203 and former Lab 125 for their support and providing a productive and professional environment.

Financial support by the Swiss National Science Foundation (SNF) is gratefully acknowledged.

Thank you all

Acknowledgements

Acknowledgements